Spring 5-31-2012

Instabilities in newtonian films and nematic liquid crystal droplets

Te-Sheng Lin
New Jersey Institute of Technology

ABSTRACT

INSTABILITIES IN NEWTONIAN FILMS AND NEMATIC LIQUID CRYSTAL DROPLETS

by
Te-Sheng Lin

The instabilities of Newtonian films and nematic liquid crystal droplets within the framework of the long wave (lubrication) approximation are studied. For Newtonian films, it is found that, under destabilizing gravitational force, a contact line, modeled by a commonly used precursor film model, leads to free surface instabilities without any additional natural or imposed perturbations. In addition, there is a coupling between the surface instabilities and the transverse (fingering) instabilities which leads to complex behavior. All the observed phenomena are characterized by a single parameter $D = (3Ca)^{1/3} \cot \alpha$ where Ca is the capillary number and α is the inclination angle. Variation of D leads to changes in the wavelike properties of the instabilities, allowing us to observe traveling wave behavior, mixed waves, and waves resembling solitary ones. The study is also extended to explore partially wetting fluids by introducing the disjoining pressure in the thin film equation. It is found that there exists an additional regime where the film breaks up into a series of droplets.

For nematic liquid crystal droplets, a model is derived based on the long wave approach available in the literatures. In particular, the surface anchoring energy is chosen such that very thin films admit the isotropic phase while thick ones remain nematic. The model permits fully nonlinear time-dependent simulations. These simulations, for the appropriate choice of parameter values, exhibit most of the phenomena appearing in the series of experiments. Finally, the influence of elastic distortion energy and the effect of anchoring variations at the substrate are explored through simple linear stability analysis, serving as a good indicator of the behavior of more complicated spreading drops.

INSTABILITIES IN NEWTONIAN FILMS AND NEMATIC LIQUID CRYSTAL DROPLETS

by
Te-Sheng Lin

A Dissertation
Submitted to the Faculty of
New Jersey Institute of Technology and
Rutgers, The State University of New Jersey – Newark
in Partial Fulfillment of the Requirements for the Degree of
Doctor of Philosophy in Mathematical Sciences

Department of Mathematical Sciences, NJIT
Department of Mathematics and Computer Science, Rutgers-Newark

May 2012

APPROVAL PAGE

INSTABILITIES IN NEWTONIAN FILMS AND NEMATIC LIQUID CRYSTAL DROPLETS

Te-Sheng Lin

Lou Kondic, Ph.D, Dissertation Advisor — Date
Professor, Department of Mathematical Sciences, NJIT

Linda J. Cummings, Ph.D, Dissertation Co-Advisor — Date
Associate Professor, Department of Mathematical Sciences, NJIT

Robert M. Miura, Ph.D, Committee Member — Date
Distinguished Professor, Department of Mathematical Sciences, NJIT

Richard O. Moore, Ph.D, Committee Member — Date
Associate Professor, Department of Mathematical Sciences, NJIT

Peter Palffy-Muhoray, Ph.D, Committee Member — Date
Professor of Chemical Physics and Associate Director of Liquid Crystal Institute,
Kent State university

BIOGRAPHICAL SKETCH

Author: Te-Sheng Lin

Degree: Doctor of Philosophy

Date: May 2012

Undergraduate and Graduate Education:

- Doctor of Philosophy in Mathematical Sciences,
  New Jersey Institute of Technology, Newark, NJ, 2012
- Master of Science in Applied Mathematics,
  National Chung-Cheng University, Chia-Yi, Taiwan, 2004
- Bachelor of Science in Mathematics,
  National Chung-Cheng University, Chia-Yi, Taiwan, 2002

Major: Applied Mathematics

Publications:

T.-S. Lin, L. Kondic and A. Filippov, Thin film flowing down inverted substrates: three dimensional flow, *Phys. Fluids*, **24**, 022105 (2012).

T.-S. Lin, L. Kondic and L. J. Cummings, Defect modeling in spreading nematic droplets, *Phys. Rev. E*, **85**, 012702 (2012).

L. J. Cummings, T.-S. Lin and L. Kondic, Modeling and simulations of the spreading and destabilization of nematic droplets, *Phys. Fluids*, **23**, 043102 (2011).

T.-S. Lin and L. Kondic, Thin films flowing down inverted substrates: Two dimensional flow, *Phys. Fluids*, **22**, 052105 (2010).

To my wife, Chiung-Jiuan Chen, my parents, Jau-Yang Lin and Mei-Yu Z. Lin, and my family.

ACKNOWLEDGMENT

I would like to thank my advisors, Professor Lou Kondic and Professor Linda J. Cummings for the countless discussions in which they have given me invaluable insights, advice and encouragement. My dissertation, publications, presentations and even this degree would not be possible without their support. I am deeply grateful for their guidance and patience through these years.

Thank you to my committee members, Professor Robert M. Miura, Professor Richard O. Moore and Professor Peter Palffy-Muhoray for their stimulating questions helpful suggestions.

I would like express my gratitude to all the professors whom I took classes from at NJIT, and special thanks to Professor John K. Bechtold, Professor Amitabha K. Bose, Professor Wooyoung Choi, Professor Shidong Jiang, Professor Jonathan H. Luke, Professor Richard O. Moore, Professor Robert M. Miura and Professor Michael S. Siegel for their excellence in teaching.

I would like to thank all the graduate students in the Department of Mathematical Sciences at NJIT whom I have got to know in the past five years. Especially, thank you to Qiming Wang, Jacek Wrobel, Matthew Causley, Xiaoni Fang, Qiyi Zhou, Iveta Jancigova, Daniel Cargill, Daniel Fong, Peixin Zhang, Xing Zhong, Zhi Liang, Jeffrey Pohlmeyer, Oleksiy Varfolomiyev for helpful discussion regarding life, research and research life.

I would like to thank Kuan Xu and Yu-Hau Tseng for their patience and willingness to explore with me never-ending mathematical problems.

I would like to thank my family for their support and encouragement. Special thanks to my parents for organizing my marriage while I was physically in the United States. Also thanks to my wife for taking care of my life. It is especially valuable that we can support each other in a place away from our home country, Taiwan.

TABLE OF CONTENTS

TABLE OF CONTENTS
(Continued)

Chapter **Page**

LIST OF TABLES

LIST OF FIGURES

Figure **Page**

LIST OF FIGURES
(Continued)

Figure **Page**

CHAPTER 1

INTRODUCTION

The field of thin liquid films has surprisingly wide application in our daily life. From industrial coating and painting processes to printing, many technologies nowadays require the study of fluid flow in which one spatial dimension (the film thickness) is significantly smaller than the others (typically, the scales on which film thickness changes). Under such circumstances one can use systematic asymptotic methods based on a small parameter (usually the film aspect ratio) to simplify the full Navier-Stokes governing equations. Expanding the dependent variables of interest (fluid velocity, pressure, etc.) in terms of this small parameter, once can obtain a much simpler system of reduced equations for the leading-order quantities. Despite its simplicity, this approach has been used and experimentally tested many times, and has been found to be very successful in describing the real physics in a wide range of flows.

In particular, this asymptotic approach, so-called lubrication theory, has been widely used in exploring the dynamics of films under gravity or other body and surface forces in a variety of settings. For then Newtonian fluid films, research activities have evolved in a few rather disjoint directions. One of these is flow down an incline of films characterized by the presence of fronts (contact lines). These flows are known to be unstable with respect to transverse instability, leading to formation of finger-like or saw-tooth patterns [8, 12, 23, 33, 65]. One may also consider flow of a continuous stream of fluid down an incline. Experimentally, this configuration was analyzed first by Kapitsa and Kapitsa [35] and more recently in much more detail in a number of works, in particular by Gollub and collaborators [43, 44, 45]. We also refer the reader to [4, 16] for relatively recent reviews. There has also been some works on

the related problem of fluid flow down an inverted substrates. These works involve either the mathematical/computational analysis of the situation leading to finite time singularity, i.e., detachment of the fluid from the surface under gravity [64], or experimental works involving the so-called "tea-pot effect" [36, 55], that includes the development of streams and drops that occur as a liquid film (or parts of it) detach from an inverted surface [34]. These considerations typically do not include contact line treatment; the fluid film is assumed to completely cover the considered domain.

On the other hand, while plenty of work has been done with Newtonian fluids, this kind of systematic asymptotic treatment of flowing thin non-Newtonian fluids, in particular liquid crystals, is still in its infancy. Liquid crystals are anisotropic liquids consisting of rod-like molecules. In a nematic phase, the rod-like molecules have no positional order, but they self-align to reach long range directional order. Therefore, to have a complete description of a nematic liquid crystal (NLC) flow, one needs to consider not only the velocity field, but also the orientational director field. In the direction of asymptotic modeling of such flows, based on the long wave approach, Ben Amar & Cummings [6] and Cummings [20] derived a model to describe the surface evolution of NLCs, while Carou et al. [11] studied two-dimensional flow of NLC in a slowly varying channel. In the experimental direction, Poulard & Cazabat [54] found that a spreading NLC droplet exhibits surprisingly rich instabilities (on the contrary, a Newtonian droplet will only spread stably). The results of [6, 20] go some way towards explaining the occurrence of such instabilities, but the full details of the driving mechanism, as well as a mathematical model that correctly describes the contact line motion of the NLC flow are still to be explored.

In this Dissertation, we take advantage of the long wave (lubrication) theory to model Newtonian film flow as well as the flow of nematic liquid crystals, with special emphasis on understanding the role of the contact line on the formation of surface

waves and fingering patterns. For the first part, Newtonian film flow, we investigate the dynamics of films under destabilizing gravitational forces. We find that the presence of a contact line leads to surface instabilities without any other perturbation. The coupling between such surface instabilities and transverse (fingering) instabilities gives rise to complex behavior. We have found that the instabilities can be categorized into three regimes, with different wavelike properties. For the second part, nematic liquid crystal flow, we derive the evolution equation of a spreading NLC droplet based on long wave theory. The present model shows satisfactory behavior in the vicinity of the contact line. We further study the influence of anchoring energy on a spreading NLC droplet and explain the mechanism of instabilities found in the experiments [54].

This Dissertation is organized as follows. In Chapter 2 we investigate the flow of thin films down an inclined or inverted inclined plane. We reviewed related existing literature in Section 2.1. We consider two-dimensional flow in Section 2.2 to investigate the influence of a contact line on surface instabilities. Three-dimensional flow is studied in Section 2.3 with emphasis on the coupling between the surface instabilities and transverse (fingering) instabilities. In Section 2.3.4, we also study the case that is perhaps most relevant to applications, the flow of thin films with variable viscosity. Finally, the flow of a partially wetting fluid is studied in Section 2.4. The influence of contact angle on the instabilities described above is explored.

In Chapter 3 we study the flow of nematic liquid crystal. We derive a model that is capable of describing the motion of a contact line. The derivations are shown in Section 3.2. We investigate the influence of surface anchoring in Section 3.3 and the influence of the prescribed director orientation at the substrate in Section 3.4. In Section 3.5, we compare the instabilities found in our model with those found in the experiments by Poulard & Cazabat [54]. We find qualitative agreement.

Finally, in Chapter 4 we make some concluding remarks with comments on possible directions of further investigations. Also, certain technical details were left

out of the main chapters to preserve the flow of ideas; these details are included in the appendices. In Appendix A, we present the analysis on the evolution of small perturbations of the thin film equation. In Appendix B, we present the numerical method used to simulate the evolution equations considered in this Dissertation.

The research results presented in this Dissertation has so far led to four refereed journal publications. Two-dimensional flow down an incline (material in Section 2.2) was published in Physics of Fluids, 2010 [40], and the three-dimensional problem in Physics of Fluids, 2012 [42]. The flow of nematic liquid crystals without presence of defects was considered in the paper published in Physics of Fluids, 2011 [21], while two-dimensional flow with defects was discussed in Physical Review E, 2012 article [41]. Furthermore, the research presented here inspired an undergraduate student project in the Capstone laboratory in the Department of Mathematical Sciences, where downslope flow of nematic liquid crystals was considered using analytical, computational, and experimental techniques. This project has led to undergraduate publication in SIAM Undergraduate Research Online [48].

CHAPTER 2

THIN HANGING FILM WITH A FRONT

2.1 Introduction

The problem of spreading of thin films on a solid surface is of interest in a variety of applications, many of which were discussed and elaborated upon in excellent review articles [16, 19, 50, 58, 66]. Perhaps the largest amount of work has been done in the direction of analyzing properties of the flow of a uniform film spreading down an incline. Starting from a pioneering work by Kapitsa and Kapitsa [35] and progressing to more contemporary contributions [4, 16, 43], a rich mathematical structure of the solutions of governing evolution equations, usually obtained within the framework of long wave (lubrication) approach has been uncovered. The models developed have led to evolution equations nowadays known as Kuramoto-Sivashinksy [14, 59], Benney [50] and Kapitsa-Shkadov [18, 69]. A variety of nonlinear waves have been found; such waves, together with the conditions leading to their formation, are briefly discussed in the Introduction to our work [40]. For the purpose of the present work, it is worth emphasizing that the linear and nonlinear waves discussed in the cited literature resulted from either natural or forced perturbations of the film surface, in the setup where inertial effects were relevant: flow of uniform film (no contact line) down an inclined plane (with inclination angle $\alpha \leq \pi/2$, shown in Figure 2.1) is stable in the limit of zero Reynolds number.

In another direction, there has also been a significant amount of work analyzing a different type of instabilities due to the presence of fluid fronts, bounded by contact lines where the three phases (gas, liquid, solid) meet. The fluid fronts are unstable, leading to the formation of finger-like structures [70] whose properties depend on the relative balance of the in-plane and out-of-plane components of gravity [25, 38], as

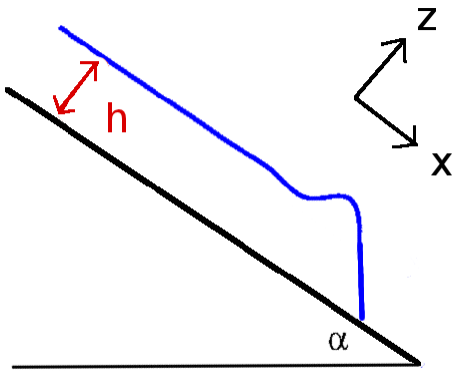

Figure 2.1 Definition sketch of the inclination angle α, film thickness h and coordinates x and z. The coordinate y (not shown in the figure) is the direction pointing out of the plane.

well as on wetting properties of the fluid [23, 33, 65]. The analysis of the contact-line induced instabilities has so far concentrated on films flowing down an incline, so with $\alpha \leq \pi/2$. In this configuration, as opposed to the case of a fluid front, the fluid surface itself is stable - typically, the only structure visible on the main body of the film is the capillary ridge which forms just behind the contact line.

It is also of interest to consider situations where body forces (such as gravity) are destabilizing, as is the case during spreading down an inverted surface, with $\alpha > \pi/2$. Such a flow is expected to be unstable, even if inertial effects are neglected. Examples of related instabilities are wave and drop structures seen in experimental studies of a pendant rivulet [2, 34]. Furthermore, if contact lines are present, one may expect coupling of different types of instabilities discussed above. In this context of front/contact line induced instabilities, two incompressible viscous fluids in an inclined channel were considered [63], while more recently the configuration where the top layer is denser than the bottom one was studied [46]. Such configurations were found to be unstable, and give rise to large amplitude interfacial waves.

In addition to mathematical complexity, this setting is of significant technological relevance, in particular in problems where there is also a temperature

gradient present, which may lead to a significant variation of viscosity of the film. Despite significant progress in the study of isoviscous thin film flows, surprisingly few studies have been devoted to analyses of fluid dynamics of thin films with variable viscosity. Meanwhile, such flows are rather common in various industrial applications. Well-known examples include layers of liquid plastics and paints used for coatings, as well as other materials, whose viscosities are strong functions of temperature. Very often, the temperature variations are difficult to detect and prevent. Corresponding variations of viscosity affect the processes and, as we will discuss in this work, can be included in the model in a relatively straightforward manner.

The present chapter consists of three related parts with slightly different focus. In the first part, Section 2.2, we consider the 2D flow of a completely wetting film spreading on an inverted surface. The problem is formulated in Section 2.2.1, followed by results of numerical simulations and analysis. Particularly, in Section 2.2.5, we discuss the relation between the nondimensional parameter D in our model and physical quantities. We conclude this part by showing the experimental conditions for which the results we show can be observed in Section 2.2.6.

Section 2.3 considers in general terms the 3D flow of a film spreading on an inverted surface. In Section 2.3.1, we consider instabilities occurring in the flow of a single rivulet, as the simplest example of a 3D flow. Fully 3D flow is considered in Section 2.3.2, where we discuss in particular the interaction between the surface instabilities considered previously in the 2D setting, and the transverse fingering instabilities at the front. We also briefly comment on the connection of the instability considered here and the Rayleigh-Taylor instability mechanism in Section 2.3.3. Section 2.3.4 discusses a setting which is perhaps more closely related to applications: dynamics of a finite width fluid film characterized by a nonuniform viscosity which varies in the transverse direction. Such a setting may be relevant, for example, to fluid exposed to a temperature gradient, leading to nonuniform viscosity.

Section 2.4 considers the influence of partially wetting on a spreading film. In particular, we are interested in the regime where the van der Waals forces and gravitational force are both relevant. We choose an appropriate scaling and formulate the problem in Section 2.4.1. In Section 2.4.2, we perform linear stability analysis of a flat film to gain some insight into the problem. We then show the results of numerical simulations for a film on a horizontal surface as well as on an inclined plane.

2.2 Two-Dimensional Flow

2.2.1 Problem Formulation

We consider completely wetting fluid flowing down a planar surface enclosing an angle α with the horizontal. The flow is considered within the framework of the lubrication approximation and inertial effects are neglected, see e.g., [50]. In particular, the spatial and velocity scalings, denoted by x_c and U, respectively, are chosen as

$$x_c = \left(\frac{a^2\, h_c}{\sin\alpha}\right)^{1/3}, \quad U = \frac{\rho g\, h_c^2}{3\mu}\, \sin\alpha, \tag{2.1}$$

where $a = \sqrt{\gamma/\rho g}$ is the capillary length, γ is the surface tension, ρ is the fluid density, g is the gravitational acceleration, μ is the viscosity and $h_c \ll x_c$ is the scaling of the film thickness. Assuming that nondimensional slopes are $O(1)$, strict validity of the lubrication approximation requires that $[(h_c/a)\sqrt{\sin\alpha}]^{2/3} \ll 1$. Within this approach, one obtains the dimensionless depth averaged velocity $\boldsymbol{v}$

$$\boldsymbol{v} = h^2\nabla\nabla^2 h - Dh^2\nabla h + h^2\mathbf{i}, \tag{2.2}$$

where $h = h(x, y, t)$ is the fluid thickness (illustrated in Figure 2.1), $\nabla = (\partial x, \partial y)$, x, y are spatial variables, t is time and $\mathbf{i} = (\mathbf{1}, \mathbf{0})$ is the unit vector pointing in the x direction. The parameter $D = (3Ca)^{1/3}\cot\alpha$ measures the size of the gravitational component perpendicular to the fluid film, where $Ca = \mu U/\gamma$ is the capillary number. Using this expression and mass conservation $h_t + \nabla\cdot(h\boldsymbol{v}) = 0$, we obtain the following

PDE discussed extensively in the literature, see e.g., [37, 51, 61]:

$$\frac{\partial h}{\partial t} + \nabla \cdot \left[h^3 \left(\nabla \nabla^2 h - D \nabla h + \mathbf{i} \right) \right] = 0. \tag{2.3}$$

To avoid the well-known issue of the singularity at a moving contact line, we implement a precursor film approach, assuming that the surface is pre-wetted by a thin film of thickness b. This approach has been used extensively in the literature; see e.g., [40] for a recent review of this and other methods used in modeling thin film flows.

2.2.2 Initial and Boundary Conditions

We consider two-dimensional flow first, in which h is y-independent. Equation (2.3) can be rewritten as

$$\frac{\partial h}{\partial t} + \left[h^3 \left(h_{xxx} - D h_x + 1 \right) \right]_x = 0 \ . \tag{2.4}$$

The boundary conditions are such that constant flux at the inlet is maintained. The choice implemented here is

$$h(0,t) = 1, \quad h_{xxx}(0,t) - D h_x(0,t) = 0. \tag{2.5}$$

At $x = L$, we assume that the film thickness is equal to the precursor, so that

$$h(L,t) = b, \quad h_x(L,t) = 0, \tag{2.6}$$

where L is the domain size and $b \ll 1$ is the precursor film thickness. Typically, we set $b = 0.01$. It is also possible to set b even smaller. However, we have found that this change has only minor influence on the results. The initial condition is chosen as a hyperbolic tangent to connect smoothly $h = 1$ and $h = b$ at $x = x_f$. It has been verified that the long term results are independent of the details of these procedures.

2.2.3 Computational Results

It is known that for flow down a vertical plane, $\alpha = \pi/2$, a capillary ridge forms immediately behind the fluid front [37]. This capillary ridge can be thought of as a strongly damped wave in the streamwise direction. As we will see below, this wave is crucial for understanding the instability that develops for a flow down an inverted surface. Here, we first outline the results obtained numerically for various values of the coefficient D, and then discuss the main features in more detail in the following section. We use $x_f = 5$ for all the simulations presented in this section.

Type 1: $-1.1 \leq D < 0$. For these values of D, we still observe existence of a dominant capillary ridge; this ridge becomes more pronounced as the magnitude of D is increased. In addition, we also observe secondary, strongly damped oscillations behind the main ridge. Figure 2.2 shows an example of an evolution profile. For longer times, a traveling wave solution is reached, and the wave speed reaches a constant value equal to $U = 1 + b + b^2$, as discussed, e.g., in [8]. Appendix A.1 gives more details regarding this traveling wave solution.

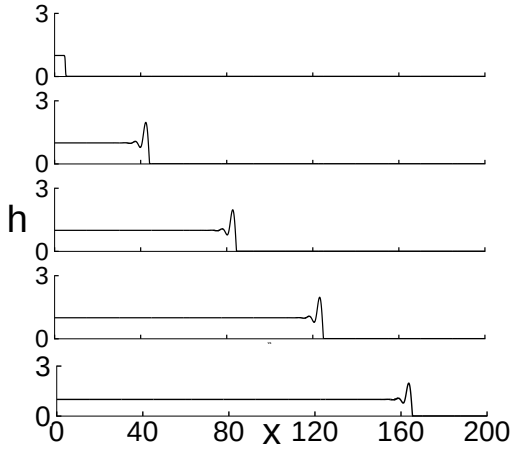

Figure 2.2 The flow down an inverted substrate ($D = -1.0$). From top to bottom, $t = 0$, 40, 80, 120, 160.

Type 2: $-1.9 \leq D < -1.1$. The capillary ridge is still observed; however, here it is followed by a wave train. Figure 2.3 shows an example of the evolution for

$D = -1.5$. Waves keep forming behind the front, and, furthermore, they move *faster* than the front itself. Therefore, the first wave behind the front catches up with the ridge, interacts and merges with it. The other important feature of the results is that there are three different states observed behind the capillary ridge: two types of waves and a constant state. These states can be clearly seen in the last frame of Figure 2.3. Immediately behind the front, there is a range characterized by waves resembling solitary ones [16] discussed in some more detail below. This range is followed by another one with sinusoidal shape waves. Finally, there is a constant state behind. Such mixed-wave features remain present even for very long times. To illustrate this, Figure 2.4 shows the result at much later time, $t = 340$, using an increased domain size.

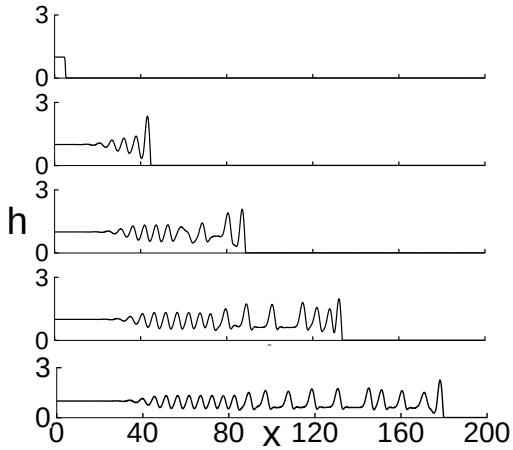

Figure 2.3 The flow down an inverted substrate ($D = -1.5$). From top to bottom, $t = 0$, 40, 80, 120, 160.

Also, Figure 2.5, which includes typical results from the *Type 3* regime discussed below, implies that *Type 2* corresponds to a transitional regime between the *Types 1* and *3*. Additional simulations (not shown here) suggest that the regions where the waves are present within the *Type 2* regime become more and more extended as the magnitude of D is increased. Future insight regarding the nature of wave formation in the *Type 2* regime is discussed in the following Section. Here we note that the

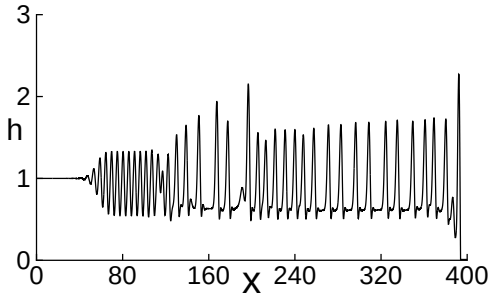

Figure 2.4 The flow down an inverted substrate ($D = -1.5$) at $t = 340$.

available animations of wave evolution are very helpful to illustrate the complexity of the wave interactions in *Type 2* and *Type 3* regimes discussed next.

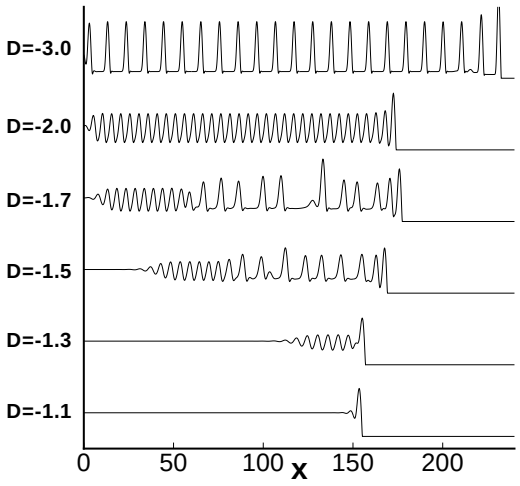

Figure 2.5 Comparison of the results for different Ds at $t = 150$.

Type 3: $-3.0 \leq D < -1.9$. This is a nonlinear steady traveling wave regime. There is no damping of surface oscillations that we observed e.g., in Figure 2.3. Figure 2.6 shows an example obtained using $D = -2.0$. Here, a wave train forms behind the first (still dominant) capillary ridge. Similarly as before, since this wave train travels faster than the fluid front, there is an interaction between the first of these waves and the capillary ridge. On the other end of the domain, these waves also interact with the inlet at $x = 0$; the role of this interaction is discussed in more detail later in Section 2.2.4.3.

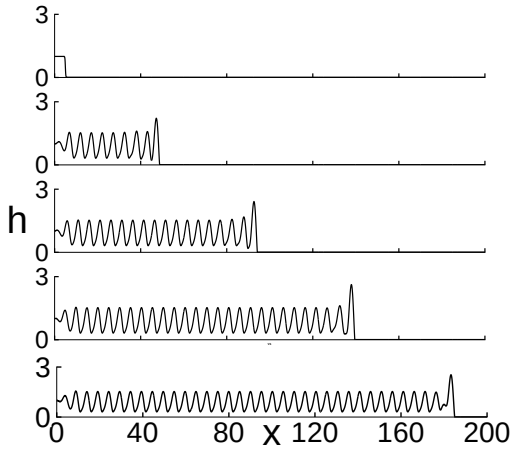

Figure 2.6 The flow down an inverted substrate ($D = -2.0$). From top to bottom, $t = 0$, 40, 80, 120, 160. Note that there is a continuous interaction of the surface waves and the front, since the surface waves travel faster than the front itself.

We find that the *Type 3* includes two sub-types. For smaller absolute values of D, such as $D = -2.0$, one finds sinusoidal waves as shown in Figure 2.6. For larger magnitudes of D, we find solitary type waves, the structures sometimes referred to as 'solitary humps', such that the characteristic dimension of a hump is much smaller than the distance between humps [16]. Both types of waves are illustrated in Figure 2.5, which shows the results for $D = -2.0$ and $D = -3.0$, and in Figure 2.7, showing the typical wave profiles for $D = -2.0$, $D = -2.5$ and $D = -3.0$. The wave profiles that we find are very similar to those observed for continuous films exposed to periodic forcing [17, 44, 49]. For the flow considered here, the governing parameter is D, in contrast to the forcing frequency in the works referenced above.

In the next section, we will discuss in more detail some features of the results presented here. Here, we only note that it may be surprising that we have found waves in the numerical simulations, remembering that we do not impose forcing on the inlet region, and furthermore, we do not include inertial effects in our formulation. Instead, we have a hanging film with a contact line in the front. Therefore, it appears that the presence of fronts and corresponding contact lines plays an important role in instability development.

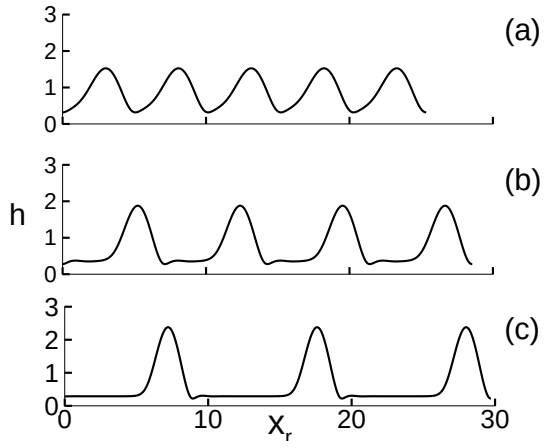

Figure 2.7 Wave profile for different Ds. (a): $D = -2.0$; (b): $D = -2.5$; (c): $D = -3.0$. The wave profiles have been shifted to illustrate the difference in wave number, i.e., $x_r = x - x_0$ where x_0 is an arbitrary shift.

We note that it is possible in principle to carry out the computations also for larger negative values of D. We find that, as the absolute value of D is increased, the amplitude of the waves, including the capillary ridge, increases, and furthermore, the periodicity of the wave train following the capillary ridge is lost. However, since the observed structures are characterized by relatively large spatial gradients which at least locally are not consistent with the lubrication approximation, we do not show them here. It would be of interest to consider this flow configuration beyond the lubrication approximation and analyze in more detail the waves in this regime. In addition, this regime should also include the transition from flow to detachment, the configuration related to the so call 'tea-pot' effect [34, 36, 55].

2.2.4 Discussion of the Results

In this Section, we discuss in some more detail the main features of the numerical results and compare them to those found in the literature. We consider in particular the difference between the various regimes discussed above. In Section 2.2.4.1, we give the main results for the velocities of the film front and the propagating waves. In Section 2.2.4.2, we discuss the main features of the instability that forms and show

that the presence of the contact line is important in determining the properties of the waves, including their typical wavelength. Then, we finally discuss one question that was not considered explicitly so far: What is the source of the instability? As we already suggested, the contact line appears to play a role here. However, it is appropriate to also discuss the influence of numerical noise on instability development, shown in Section 2.2.4.3. As we will see, both aspects are important to gain better understanding of the problem.

2.2.4.1 Front Speed and Wave Speed. Figure 2.8 compares the velocity of the leading capillary ridge, V, for different Ds. The speed of the traveling wave solution, U, is $1 + b + b^2$, and is exactly the front speed for $D = -1.0$, as discussed in Appendix A.1. For all other cases shown, the velocity of the leading capillary ridge oscillates around U, due to the interaction between the leading capillary ridge and the waves coming from behind.

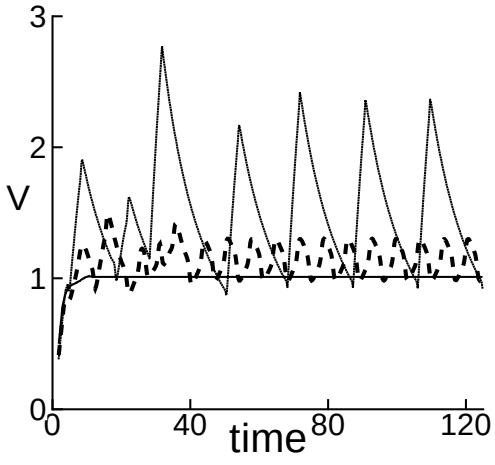

Figure 2.8 Velocity profile of the leading capillary ridge for different Ds. $D = -1.0$ (solid), $D = -2.0$ (dashed), $D = -3.0$ (dotted).

Table 2.1 shows the speed of waves in *Type 3* regime. As we can see, the wave speed in all cases is greater than U (≈ 1). A simple explanation of why the waves move faster than the fluid front itself is that the motion of the front is resisted by the

precursor film (recall that in the limit $b \to 0$, there is infinite resistance to the fluid motion within the formalism implemented here). The surface waves, however, travel with a different, larger speed. Therefore, the upcoming waves eventually catch up with the front, interact, and merge into a new capillary ridge. Figure 2.9 illustrates this process. As the leading capillary ridge moves forward, its height decreases until the next wave arrives. That is the reason why we see such pulse-like velocity profiles in Figure 2.8; each pulse is a sign of a wave reaching the front. In the *Type 2* regime, the velocity of the front shows similar oscillatory behavior, although the approximate periodicity of the oscillations is lost due to more irregular structure of the surface waves. Going back to *Type 3* waves and Table 2.1, we see that wave amplitude and speed are both increasing with D, consistent with the behavior of continuous vertically falling films [3, 17].

Table 2.1 Wave Amplitude and Wave Speed for Different D in *Type 3* Regime

D	wave amplitude	wave speed
-2.0	1.53	1.88
-2.5	1.88	2.20
-3.0	2.38	2.65

2.2.4.2 Absolute Versus Convective Instability. Here we analyze some features of the results from the *Type 1* and *Type 2* regimes using linear stability analysis. Let us ignore, for a moment, the contact line and analyze stability of a flat film. The basic framework is given in the Appendix A.2. We realize that Equation (A.4) can be reduced to a linear Kuramoto-Sivashinsky equation in the reference frame moving with the nondimensional speed equal to 3. Consider then the evolution of a localized disturbance imposed on the flat film at $t = 0$. This disturbance will transform into an expanding wave packet with two boundaries moving with the

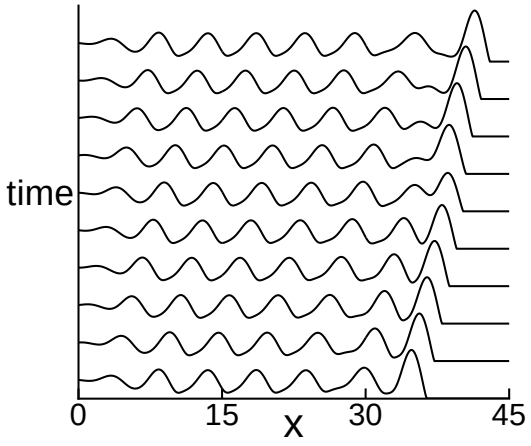

Figure 2.9 Wave interaction with the capillary ridge. Time evolution is from the bottom to the top, $D = -2.0$.

velocities $(x/t)_-$ and $(x/t)_+$ [32]. In the laboratory frame, as shown in Appendix A.3, these velocities are given by [15]

$$\left(\frac{x}{t}\right)_{\pm} \approx 3 \pm 1.62\,(-D)^{3/2}. \tag{2.7}$$

The right-going boundary, $(x/t)_+$, moves faster than the capillary ridge and can be ignored. Considering now the left boundary, $(x/t)_-$, we see that there is a range $D_{c1} > D > D_{c2}$ such that the speed of this boundary is positive and smaller than U. Alternatively, one can use the approach from [30], which is based on studying the behavior of the curve $\omega_i = 0$ in the complex k plane, with the same result. Using either approach, one finds $D_{c1} \approx -1.15$ and $D_{c2} \approx -1.51$. This result explains the boundary between the *Type 1* and *Type 2* regimes since for *Type 1*, $D > D_{c1}$ and the left boundary moves faster than the front itself. For $D > D_{c2}$, the speed of the left boundary is positive, and therefore the instability is of convective type. This can be seen from Figure 2.5 and is illustrated in detail in Table 2.2. In this table, we show the value of D_{lin}, predicted by Equation (2.7), using the position of the left boundary x_- taken from Figure 2.5 ($t = 150$). While the agreement between D_{num} and D_{lin}

is generally very good, we notice some discrepancy for $D_{num} = -1.7$; this can be explained by the fact that for this D_{num} there is already some interaction with the boundary at $x = 0$.

Table 2.2 Numerical Results on Speed of Left Boundaries, $(x/t)_-$

D_{num}	x_-	$(x/t)_-$	D_{lin}
-1.1	150	1.00	-1.15
-1.3	100	0.66	-1.28
-1.5	30	0.20	-1.44
-1.7	0	0.00	-1.51

These results suggest that we should split our *Type 2* regime into two parts: *Type 2a*, for which the speed of the left boundary is positive ($D > D_{c2}$), and *Type 2b*, for which the speed of the boundary is negative and the instability is of absolute type. In *Type 2a* regime, a flat film always exists and expands to the right with time. In *Type 2b* regime, the flat film disappears after sufficiently long time. As an illustration, we note that $D = -1.5$ shown in Figure 2.3, lies approximately at the boundary of these two regimes, since here the length of the flat film is almost time-independent. We also note that in *Type 2b* regime, we always observe two types of waves, in contrast to *Type 3*; that is, the structure shown, e.g., in Figure 2.5 for $D = -1.7$, persists for a long time.

To allow for better understanding of the properties of the waves that form, in the results that follow we have modified our initial condition (put $x_f = 50$) to allow for longer wave evolution without interaction of the wave structure with the domain boundary ($x = 0$). Figure 2.10 shows that for $D = -2.0$, the waves form immediately behind the leading capillary ridge; see also the animation attached to this figure. For longer time ($t > 40$ in Figure 2.10), the disturbed region covers the whole domain as expected based on the material discussed in Section 2.2.4.2. Note that even for

$t = 100$, we still see transient behavior: the long time solution for this D consists of a uniform stream of waves and is shown in Figure 2.7(a). This long time solution is independent of the initial condition. However, the time period needed for this uniform stream of waves to be reached depends on the initial film length and is much longer for the larger x_f used here.

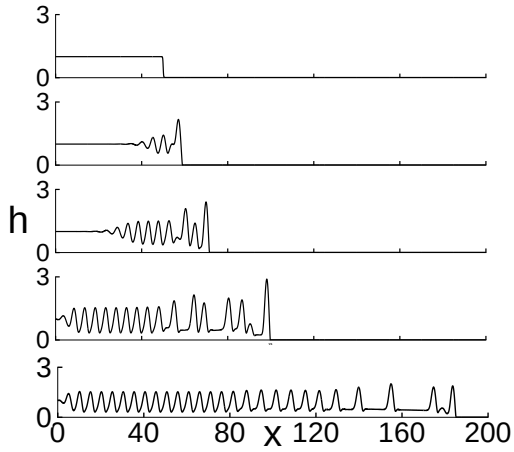

Figure 2.10 $D = -2.0$. From top to bottom, $t = 0$, 10, 20, 40, 100. For early times, the contact line induced instability propagates to the left. For longer times, sine-like and solitary-like waves are observed, covering the whole domain by $t = 40$.

Figure 2.10 suggests that the contact line plays a role in wave formation (the other candidate, numerical noise, is discussed below). One may think of the contact line as a local disturbance. It generates an expanding wave packet as we have just shown, and the velocities of the two boundaries are given by Equation (2.7). In particular, for $D < D_{c1}$, the left boundary moves slower than the capillary ridge. The wave number, k_l, along this boundary is defined by

$$\left(\frac{\partial \omega}{\partial k}\right)\Big|_{k=k_l} = \left(\frac{x}{t}\right)_- , \tag{2.8}$$

and it should be compared to the sine-like waves that form due to the presence of the contact line. Table 2.3 gives this comparison: the values of k_l for a given D are shown in the second column, followed by the numerical results for the wave number, q_n. We find close agreement, suggesting that k_l captures very well the basic features

of the waves that form due to the contact line's presence. Furthermore, both q_n and k_l are *much larger* than k_m, the most unstable wave number expected from the linear stability analysis (LSA) described below (vis. the last column in Table 2.3). This difference allows one to clearly distinguish between the contact line induced waves and the noise induced ones, discussed in what follows.

Table 2.3 Comparison between Simulations and Linear Analysis for Wavenumbers of Induced Waves

D	k_l	q_n	k_m
-1.3	1.10	1.10	0.81
-1.5	1.18	1.14	0.87
-1.7	1.25	1.23	0.92
-2.0	1.36	1.35	1.00
-2.5	1.52	1.48	1.12

2.2.4.3 Noise Induced Waves. The results of the LSA of a flat film (see Section A.2) for the most unstable wave number shown in Table 2.3, confirm that a flat film is unstable to long wave perturbations for negative Ds. Although our base state is not a flat film, there is clearly a possibility that numerical noise, which includes long wave components, could grow in time and influence the results. As an example, we consider again $D = -2.0$. Similar results and conclusions can be reached for other values of D.

Let us first discuss the expected influence of numerical noise. For $D = -2.0$, the LSA shows that it takes 30 time units for the noise with an initial amplitude of 10^{-16} (typical for double precision computer arithmetic) to grow to 10^{-2}. LSA also shows that waves with small amplitude should move with the speed 3. That is, natural (numerical) noise, which is initially at $x = 0$, should arrive to $x = 90$

after 30 time units. Figure 2.11 (a) illustrates this phenomenon. As t approaches 30, we see that the noise appears at about $x = 90$. Noise manifests itself through the formation of waves *behind* the contact line induced waves; which were already present for earlier times. To further confirm that this new type of waves is indeed due to numerical noise, we have also performed simulations using quadruple precision computer arithmetic. Figure 2.11 (b) shows the outcome: with higher precision, the noise induced waves are absent, as expected. We note that in order to be able to clearly identify various regimes, we take $x_f = 150$ in Figure 2.11 (a) and (b), so that no influence of the boundary condition at $x = 0$ is expected.

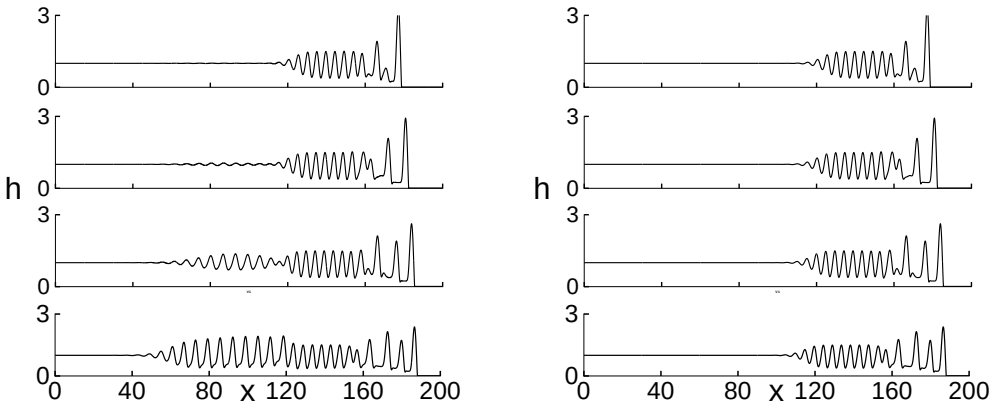

(a) Double precision (b) Quadruple precision

Figure 2.11 $D = -2.0$. From top to bottom, $t = 25, 27, 29, 31$. The initial condition for this simulation is chosen to be a hyperbolic tangent with contact line located at $x = 150$. The error-induced waves appear at (a) $(50 < x < 120)$.

In Figure 2.11 (a) $(t = 31)$, we can clearly distinguish between the waves induced by the contact line $(120 < x < 190)$, and the 'natural waves' induced by numerical noise $(50 < x < 120)$. The main difference is the wavelength. The contact line induced waves have a specific wavelength, $2\pi/k_l$, while the noise induced ones are characterized by a wavelength, λ, corresponding very closely to the mode of maximum growth, $\lambda \approx 2\pi/k_m$, obtained using LSA. This can be clearly seen by comparing the

numerical results shown in Figure 2.11 (a) ($t = 31$) with the LSA results given in Table 2.3.

To summarize, the evolution of the wave structure in the *Type 2* and *Type 3* regimes proceeds as follows. First, one sees formation of contact line induced waves, characterized by relatively short wavelengths (compared to what would be expected based on the LSA of a flat film). Depending on the value of D, one may also see formation of solitary-looking waves immediately following the capillary ridge. At some later time, these waves are followed by noise-induced ones. These three types of waves are all presented in Figure 2.11 (a). Then, at even later times, when the waves cover the whole domain and interact with the $x = 0$ boundary, the final wave pattern forms, as illustrated for $D = -2.0$ by Figure 2.5. In the conclusions, Section 2.2.6, we discuss briefly under which conditions these waves may be expected to be seen in physical experiments.

Remark I. One may wonder why the traveling wave solution for $D = -1.0$ shown in Figure 2.2 remains stable for such a long time. Recall that the LSA predicts that natural noise with amplitude 10^{-16} should grow to 10^{-2} in 130 time units, while our numerical result shows that the flat film is preserved even for $t = 160$. The reason is the domain size. It takes approximately 66 time units for noise to travel across the domain (moving with the speed equal to 3), and the noise can only grow from 10^{-16} to 10^{-9} during this time period for $D = -1$. This is why we do not see the effect of noise for small Ds.

Remark II. We have used LSA of a flat film (therefore, ignoring contact line presence) to predict the evolution of the *size* of the region covered by waves in Section 2.2.4.2. However, in order to understand the *properties* of the waves that form in this region, one has to account for the presence of a front. In our simulations, we are able to tune the influence of noise on the results (visualize Figure 2.11 (a)

versus (b)). In physical experiments, these two effects will quite possibly appear together.

2.2.5 Physical Interpretation of Nondimensional Parameter D

It is useful to discuss the relationship between the nondimensional parameter D in our model, Equation (2.4), and physical quantities. In particular, we recall that there are two quantities, h_0 (film thickness) and α (inclination angle) which can be adjusted in an experiment, and here we discuss how variation of each of these modifies our governing parameter and the results. We also relate D to the fluid flux and the Reynolds number.

The velocity scaling in Equation (2.4) can be expressed as

$$U = \frac{\rho g}{3\mu} h_0^2 \sin\alpha.$$

Therefore, the parameter D can be written as

$$D = \left(\frac{\rho g}{\gamma}\right)^{1/3} h_0^{2/3} \frac{\cos\alpha}{(\sin\alpha)^{2/3}}. \tag{2.9}$$

In our simulations, the flux Q in the x-direction is kept constant and equal to 1. The dimensional flux is

$$Q = 1 \cdot h_0 \cdot U = \frac{\rho g}{3\mu} h_0^3 \sin\alpha. \tag{2.10}$$

The Reynolds number can be expressed as

$$Re = \frac{\rho U \ell}{\mu} = \frac{(\rho^5 g^2 \gamma^2)^{1/3}}{3\mu^2} h_0^{7/3} (\sin\alpha)^{2/3}. \tag{2.11}$$

We note that there is no contradiction in considering Re, although inertial effects were neglected in deriving the formulation that we use. The present formulation is valid for $Re = O(1/\epsilon)$ or smaller, where $\epsilon \ll 1$ is the ratio of the length scales in

the out-of-plane and in-plane directions [1]. Considering the influence of Re for this range is permissible.

Table 2.4 Physical Interpretation of Nondimensional Parameter D

α fixed			h_0 fixed		
	$D > 0$	$D < 0$		$D > 0$	$D < 0$
$\|D\|$	$\uparrow$	$\uparrow$	$\|D\|$	$\uparrow$	$\uparrow$
h_0	$\uparrow$	$\uparrow$	α	$\downarrow$	$\uparrow$
Q	$\uparrow$	$\uparrow$	Q	$\downarrow$	$\downarrow$
Re	$\uparrow$	$\uparrow$	Re	$\downarrow$	$\downarrow$
U	$\uparrow$	$\uparrow$	U	$\downarrow$	$\downarrow$

The relation between D and relevant physical quantities is shown in Table 2.4. For fixed inclination angle, an increase of the magnitude of D is equivalent to an increase of the film thickness, flux and Reynolds number. On the other hand, for fixed film thickness, i.e., h_0 =constant, raising the magnitude of D leads to lower flux and Reynolds number, and the inclination angle approaches horizontal. We can use this connection to relate to the experimental results of Alekseenko et al. (see Figure 11 in [2]). They performed experiments with fixed inclination angle and increasing flux, which corresponds to an increase of the magnitude of D in our case. Figure 2.5 shows that the trend of our results is the same as in the above experiments. In addition, the results in [34] suggest that further increasing of the flux leads to pinch-off, consistent with our results, since for $D < -3.0$, numerics suggest that the lubrication assumption is not valid.

Finally, one should recall that the lubrication approximation is derived under the condition of small slopes (of the free surface), which translates to

$$\left(\frac{h_0\sqrt{\sin\alpha}}{a}\right)^{2/3} \ll 1, \tag{2.12}$$

if nondimensional slopes (of the free surface) are O(1), see e.g., [37]; here $a = \sqrt{\gamma/\rho g}$ is the capillary length. In addition, by combining the above lubrication limit with Equation (2.9), one gets the following condition (see also [31]):

$$|D| < |\cot\alpha|. \tag{2.13}$$

Therefore, for a given D, there exists a range of inclination angle for which the thin film model, Equation (2.4), is strictly valid. Table 2.5 shows this range for some values of D.

Table 2.5 Inclination Angle, α_c, at which Long Wave Theory Ceases to be Formally Valid

D	α_c (deg)
-1.0	135^o
-1.5	147^o
-2.0	154^o
-3.0	162^o

2.2.6 Conclusions

In this section, we report numerical simulation of the thin film equation, Equation (2.4), governing the height of fluid flowing down an inverted substrate. It is found that by changing a single parameter D, one can find three different regimes of instability. Each regime is characterized by a different type of waves. Some of these

waves show similar properties to those observed in thin liquid films with periodic forcing. In contrast to those waves produced by perturbations at the inlet region, our instability comes from the front. We find that the presence of a contact line leads to free surface instability without any additional perturbation. According to linear stability analysis, we know that for negative D, the model problem, Equation (2.4), is unstable in the sense that any numerical disturbance grows exponentially in time. However, we can also take advantage of the stability analysis to separate the instability caused by noise and any other sources.

Finally, we may ask about experimental conditions for which the waves discussed here can be observed. As an example, consider polydimethylsiloxane (PDMS), also known as silicon oil (surface tension: $21\,dyn/cm$; density: $0.96\,g/cm^3$), and discuss the experimental parameters for which the condition $|D| < 3.0$ is satisfied. For $\alpha = 170^o$ (the value used in [2]), the thickness should be less than $1.4\,mm$. Table 2.6 gives the values for this, as well as for some other Ds. However, one should recall that Equation (2.13) shows that our model is formally valid only up to a certain D for a given inclination angle α. In addition, one should be aware that the use of lubrication approximation is easier to justify for inclination angles further away from the vertical.

Table 2.6 The Values of α, D, and h_0 for Experimental Parameters as in [2]

α (deg)	D	h_0 (mm)
150^o	-1.0	0.93
	-1.5	1.7
170^o	-1.0	0.27
	-2.0	0.75
	-3.0	1.40

2.3 Three-Dimensional Flow

In Section 2.2, we found that for a film flowing down an inverted plane in 2D, the fluid front bounded by the contact line (contact point in 2D) played the role of a local disturbance that induces instabilities. As the inclination angle approaches 180° (that is, the parameter $D = (3Ca)^{1/3} \cot \alpha$ becomes smaller), the fluid front influences strongly the flow behind it and induces waves. In particular, the governing equation, obtained under the lubrication approximation, is found to allow for three types of solutions. We note that solutions could not be found for flows characterized by even smaller (more negative) values of D. We presume that this is due to the fact that, in this case, the gravitational force is so strongly destabilizing that detachment is to be expected. Mathematically, this may be related to the singular behavior of Benney-type equations [57]. It should be pointed out, however, that in the present context, singular behavior is physical, although not well described due to limitations inherent in the long-wave approach.

In the following, we consider, in general terms, the 3D flow of a film spreading on an inverted surface. In Section 2.3.1, we consider instabilities occurring in the flow of a single rivulet, as the simplest example of a 3D flow. Fully 3D flow is considered in Section 2.3.2, where we discuss in particular the interaction between the surface instabilities considered previously in the 2D setting (Section 2.2), and the transverse fingering instabilities at the front. We also briefly comment on the connection of the instability considered here and the Rayleigh-Taylor instability mechanism.

2.3.1 Inverted Rivulet

In this section, we consider a single rivulet with a front, following on the underside of a solid surface. The related problem of an infinite rivulet was studied in a number of works. For example, the exact solution of the Navier-Stokes equation for a steady infinite rivulet has been obtained [68], and under the lubrication assumption the

stability of such settings were studied for completely and partially wetting fluids [7, 67]. However, the influence of fluid front on the stability has not been studied. In the following, we will first extend the steady infinite rivulet solution [28] to include the presence of a precursor film. Then we will examine the effect of a fluid front on the stability of an inverted rivulet.

2.3.1.1 Inverted Infinite Rivulet. Consider a rivulet with infinite length flowing down an inverted planar surface. A steady state shape of the rivulet, independent of the downstream coordinate x can be found by solving Equation (2.3), which in this special case reduces to

$$\left(h^3 h_{yyy}\right)_y - D\left(h^3 h_y\right)_y = 0. \tag{2.14}$$

Integrating this equation and applying the boundary conditions $h_y = h_{yyy} = 0$ and integrating again yields

$$h_{yy} - Dh = c_1, \tag{2.15}$$

where c_1 is a constant. Concentrating on the inverted case, $D < 0$, the general solution can be written as

$$h_r(y) = c_2 \cos(\sqrt{-D}\, y) + c_3 \sin(\sqrt{-D}\, y) - \frac{c_1}{D}, \tag{2.16}$$

where c_2 and c_3 are constants. Without loss of generality, we impose the symmetry condition at $y = 0$ to find $c_3 = 0$, and the complete wetting assumption further determines the rivulet's width as $\left[-\pi/\sqrt{-D}, \pi/\sqrt{-D}\right]$. At the boundaries $h\left(\pm\pi/\sqrt{-D}\right) = b$, so we obtain

$$h_r(y) = \frac{A_r - b}{2} \cos\left(\sqrt{-D}\, y\right) + \frac{A_r + b}{2}, \tag{2.17}$$

where $A_r = h_r(0)$ is a constant.

According to the above analysis, we find a family of exact rivulet solutions for a given D. The unique solution can be obtained by specifying flux or average thickness at the inlet.

2.3.1.2 Inverted Rivulet with A Front.

2.3.1.2.1 Initial and Boundary Conditions. To analyze the effect of the front bounded by a contact line (regularized by the precursor) on the rivulet flow, we perform numerical simulations of the 3D thin film equation via the ADI method. The details of the implementation of the ADI method are discussed in Appendix B. The boundary conditions are such that constant flux at the inlet is maintained with the additional assumption that the shape at the inlet corresponds to a steady rivulet. The choice implemented here is

$$h(0,y,t) = h_r(y), \quad h_{xxx}(0,y,t) - Dh_x(0,y,t) = 0. \tag{2.18}$$

In addition, we choose $A_r = 2$ in the steady rivulet solution so that the average thickness at the inlet is 1. At the outlet, $x = L$, as well as at the y boundaries, $\pm M$, we assume zero-slope and a precursor film

$$h(L,y,t) = h(x,\pm M,t) = b, \quad h_x(L,y,t) = h_y(x,\pm M,t) = 0, \tag{2.19}$$

where $[0,L]$ is the domain size in the x direction, $[-M,M]$ is the domain in the y direction. The initial shape of the rivulet is chosen as a hyperbolic tangent to connect smoothly the steady solution and the precursor film at $x = x_f$ as follows:

$$h(x,y,0) = \frac{h_r(y) - b}{2} \tanh\left(-5(x - x_f)\right) + \frac{h_r(y) + b}{2}, \tag{2.20}$$

here we choose $x_f = 5$.

Due to heavy computational costs involved in resolving behavior on the precursor scale in 3D simulations (Δx should be $O(b)$), the precursor thickness is

typically set to 0.1 instead of the smaller value $b = 0.01$ used in Section 2.2. This change has only a minor influence on the boundaries of the instability regimes (the change of critical values of D is less than 10^{-2}). We have also carried out additional 3D simulations for selected cases with smaller values of b to verify that there is only a very weak influence of the exact value of b on the presented results.

2.3.1.2.2 Results. The presence of the contact line modifies the steady solution discussed in Section 2.3.1.1. Without going into the details of this modification, for the present purposes it is sufficient to realize that the speed of the traveling rivulet, V_r, can be easily computed by comparing the net flux with the average film thickness as

$$V_r = \frac{\int (h_r^3 - b^3)\, dy}{\int (h_r - b)\, dy} = \frac{5}{8} A_r^2 + A_r\, b + O(b^2). \tag{2.21}$$

V_r is useful to facilitate understanding of the computational results in the context of 2D instabilities discussed previously. For this purpose, we use V_r instead of U as a velocity scale and to avoid confusion, we denote such a D by Dn.

Figure 2.12 shows the computational results at $t = 25$. For $Dn = -1.0$, we still observe traveling-wave type solutions. We have examined the speed of the capillary ridge and found that it equals V_r, as predicted. For Dn larger in absolute value, the traveling wave solution becomes unstable and waves keep forming right behind the capillary ridge. For $Dn > -1.5$, simulations suggest that the instability is convective, since it is carried by the flow and moves downstream from the initial contact line position, x_f. For $Dn < -1.5$, the instability is absolute. At the time shown, the whole rivulet is covered by waves which in cross section resemble solitary ones.

The rivulet simulations show a qualitative similarity to our 2D simulations (vis. the right hand side of Figure 2.12 and Figure 2.5). Therefore, on one hand this result validates the accuracy of our 3D simulations. On the other hand, it also suggests that the instability regimes, (*types 1, 2,* and *3*) can be extended to 3D rivulet geometry.

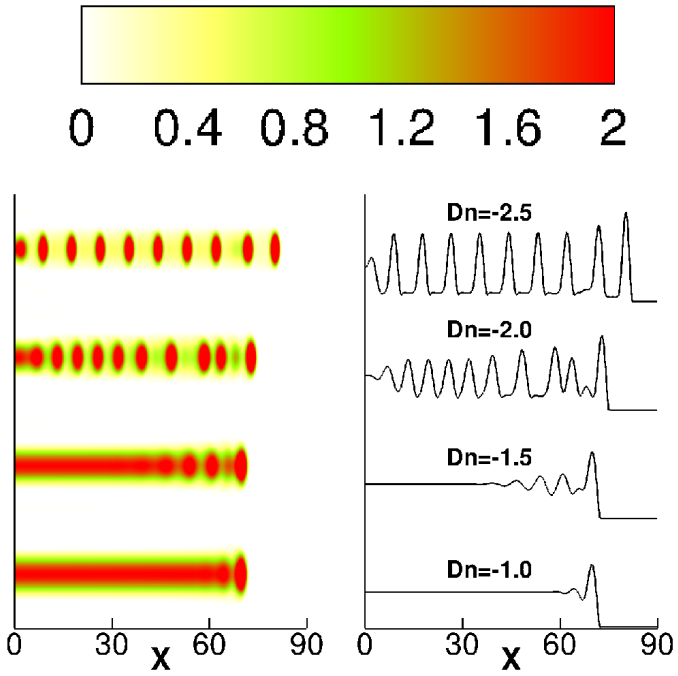

Figure 2.12 Rivulet flow for different Dn's at $t = 25$. The domain size is specified by $L = 90$ and $M = 5$. Left-hand side shows the contour plot and the right-hand side shows the cross section ($y = \text{const.}$) at the middle of a rivulet. We will use a similar way of presenting results, and the same color map in the other figures given in Section 2.3.

Clearly, it was necessary to use a renormalized value of D, Dn, to be able to carry out this comparison.

It is also of interest to relate the present results to stability properties of an inverted infinite length rivulet without a front. In this case, it is known that there exists a critical angle between $\pi/2$ and π such that the inverted infinite rivulet is unstable if the inclination angle is larger than the critical one [7]. In order to be able to directly compare the two problems (with and without a front), we have carried out simulations of an inverted infinite rivulet. The steady state is fixed by choosing the height in the middle of a rivulet $A_r = 2$. We perturb the rivulet at $t = 0$ by a single perturbation defined by $h(x, y, 0) = h_r(y)(1 + A_p\text{sech}(x - x_p))$ with $A_p = 0.2$ and $x_p = 5.0$. In this work, we consider only this type of perturbation and do not discuss in more detail the influence of its properties on the results. For this

case, we find that an inverted infinite rivulet is unstable for $Dn \leq -0.74$, which is consistent with the fact that there exists a critical angle for stability [7]. An obvious question to ask is: Which instability is dominant for sufficiently small Dn's, such that both front-induced and surface-perturbation induced instabilities are present? This question will also appear later in the context of thin film flow - to avoid repetition we consider it for that problem, in Section 2.3.3.

2.3.2 Inverted Film with a Front

We proceed with analyzing stability of an inverted film with a front flowing down a plane. In Section 2.3.2.1 we extend the results of the linear stability analysis in the transverse direction to the inverted case. Then, we proceed with fully nonlinear time dependent simulations in Section 2.3.2.2. We start with addressing a simple case where we perturb the fluid front by a single wavelength only – this case allows us to correlate the results with the 2D surface instabilities discussed previously, with the instabilities of a single inverted rivulet discussed in Section 2.3.1, and also with the well-known results for transverse instability of a film front flowing down an inclined plane, see e.g. [25]. We proceed with more realistic simulations of a front perturbed by a number of modes with random amplitudes, where all discussed instability mechanisms come into play. We conclude the section by discussing in Section 2.3.3 the connection between the instabilities considered here and the Rayleigh-Taylor type of instability of an infinite film flowing down an inverted plane.

2.3.2.1 Linear Stability Analysis in the Transverse Direction. In order to analyze the stability of the flow in the transverse, y, direction, we perform a linear stability analysis (LSA). The results of similar analysis were reported in previous works, see, e.g., [37], but they typically concentrated on downhill flows, with $D \geq 0$. Here we extend the analysis to also consider films on an inverted surface, with $D < 0$.

Consider a moving frame defined by $s = x - Vt$, and assume a solution of the form

$$h(s, y, t) = H(s) + \epsilon h_1(s, y, t), \tag{2.22}$$

where $\epsilon \ll 1$, and $H(s)$ is the traveling wave solution with speed V. Then, plug this ansatz into Equation (2.3). The leading order term ($O(\epsilon^0)$) gives the 2D equation

$$-VH' + [H^3(H''' - DH' + 1)]' = 0 \tag{2.23}$$

while the first order term ($O(\epsilon^1)$) yields

$$\begin{aligned} \frac{\partial h_1}{\partial t} &= -\nabla \cdot \left[H^3 \nabla \nabla^2 h_1 + 3H^2 h_1 \nabla \nabla^2 H\right] \\ &\quad + D\nabla \cdot \left[H^3 \nabla h_1 + 3H^2 h_1 \nabla H\right] - \left(3H^2 h_1\right)_s + V h_{1s}, \end{aligned} \tag{2.24}$$

where $\nabla = (\partial_s, \partial_y)$. The next step is to express the solution, h_1, as a continuous superposition of Fourier modes,

$$h_1(s, y, t) = \int_{-\infty}^{0} \phi(s, q) e^{\sigma t} e^{iqy} dq, \tag{2.25}$$

where q is the wavenumber and σ is the growth rate that determines the temporal evolution of h_1. For a given q, there is an associated eigenvalue problem, see e.g., [37]. The largest eigenvalue corresponds to the growth rate, which is the quantity of interest.

Figure 2.13 shows the LSA results. Each curve represents the corresponding largest eigenvalue for a given wavenumber and for fixed D. One can see that sufficiently long wavelengths are unstable. Consequently, there is a critical wavenumber, $q_c(D)$, which determines the range of unstable wavenumbers to be $[0, q_c]$. Concentrating now on negative Ds, we find that q_c increases with $|D|$, suggesting shorter unstable wavelengths for larger $|D|$s, which are furthermore expected to grow faster. Therefore, for $D < 0$, as $|D|$ is increased (for example by increasing the angle

α, or by making the film thicker), LSA predicts formation of more unstable fingers spaced more densely.

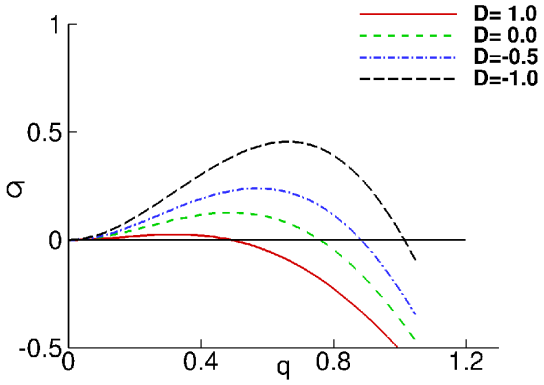

Figure 2.13 Wavenumber, q, and corresponding growth rate σ for different Ds.

One may note that Figure 2.13 only shows the results for D down to -1.0. The reason is that a base state could be found only for $D \geq -1.1$, and therefore LSA could not be carried out for smaller Ds. This issue was discussed in Section 2.2, where we were able to find traveling wave solutions only for Ds in the *type 1* regime, and could not find such solutions in the *type 2* and *3* regimes.

2.3.2.2 Fully 3D Simulations. Here we discuss the results of fully 3D simulations of the thin film equation, Equation (2.3). We choose the initial condition as for the 2D simulations - that is, two flat regions of thickness $h = 1$ and $h = b$ connected at $x = x_f$ by a smooth transition zone described by a hyperbolic tangent, perturbed as follows

$$h(x, y, 0) = \frac{1-b}{2} \tanh\left(-5(x - x_f(y))\right) + \frac{1+b}{2}, \quad x_f(y) = x_{f0} - A_0 \cos(2\pi y/\lambda), \tag{2.26}$$

where $\lambda = 2\pi/q$ is the wavelength of the perturbation and x_{f0} is the unperturbed position. Here we choose $x_{f0} = 5$. The boundary conditions in the flow direction are such that constant flux at the inlet is maintained, while at $x = L$, we assume that

the film thickness is equal to the precursor. The boundary conditions implemented here are

$$h(0,y,t) = 1, \quad h_{xxx}(0,y,t) - D\,h_x(0,y,t) = 0,$$
$$h(L,y,t) = b, \quad h_x(L,y,t) = 0.$$

For the y boundaries, we use symmetry boundary conditions,

$$h_y(x,0,t) = h_y(x,M,t) = 0, \quad h_{yyy}(x,0,t) = h_{yyy}(x,M,t) = 0, \tag{2.27}$$

where M is the width of the domain in the y direction.

Figure 2.14 shows the results of simulations for $D = -1.0$ perturbed by specified single mode perturbations. For $\lambda = 8$ and $\lambda = 10$, the perturbation evolves into a single finger, whereas for $\lambda = 20$, which corresponds to the wavelength larger than the most unstable one (visualizing Figure 2.13), we observe a secondary instability: in addition to the finger that corresponds to the initial perturbation, there is another one (which appears as half fingers at $y = 0, M$), developing at later time (in this case after $t = 10$). This is due to the fact that the mode $\lambda = 20$ is very weakly unstable. It grows slowly and leaves enough space in the domain for other unstable modes to develop.

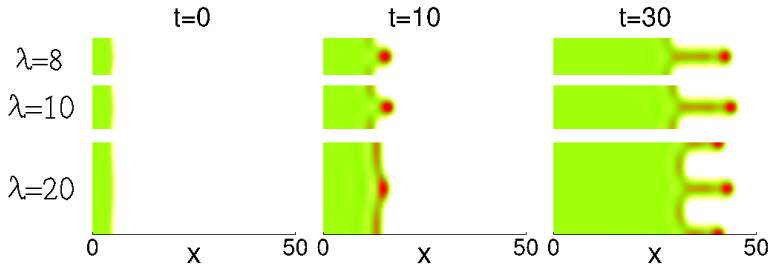

Figure 2.14 Time evolution for perturbations of different wavelengths (λ) and $D = -1.0$. Here the domain is specified by $L = 50$ and $M = \lambda$.

Next, we compare the growth rate of a finger from our 3D simulations with the LSA results. This comparison is shown in Figure 2.15 for $D = -0.5$ and $D = -1.0$.

The initial condition for these simulations is chosen as a single mode perturbation, $\lambda = M = 10$. The growth rate is extracted by considering the finger's length, A, defined as the distance between tip and root. As shown in Figure 2.15, for early times, the finger grows exponentially with the same growth rate as predicted by the LSA. For later times, the finger length exhibits a linear growth. This late time behavior can be simply explained by the fact that the finger evolves into the rivulet solution discussed in Section 2.3.1.

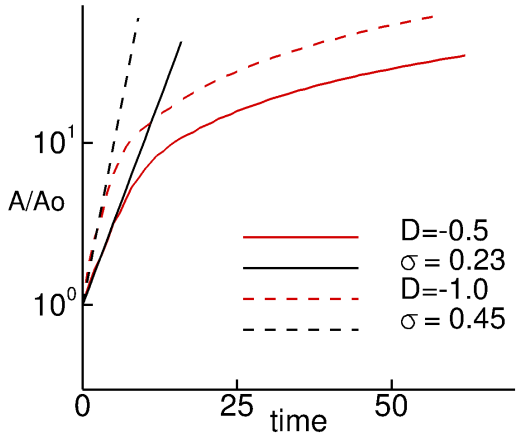

Figure 2.15 Length of a finger, A, divided by the initial length, A_0. Here $\lambda = M = 10$. Red (curved) lines show the computational results while the black (straight) lines show the LSA prediction for two different D's.

Figure 2.16 shows the numerical results for $D = -1.5$ with three single mode perturbations in a fixed domain, $[0, 90] \times [0, 20]$. Both contour plots and the cross sections at the center of the computational domain ($y = 10$) are presented. In this case, in addition to the secondary instability already observed for the perturbation $\lambda = 20$, we also see a secondary instability developing for $\lambda = 10$, suggesting that as the absolute value of (negative) D grows, shorter and shorter wavelengths become unstable. For this D, even $\lambda = 5$ is unstable. This result is consistent with the trend of the LSA results shown in Figure 2.13; note however that LSA cannot be carried out for such small Ds due to the fact that a traveling wave solution could not be

found. Instead of traveling waves, we find surface instabilities on the film. As shown in the contour plot at $t = 50$, several red(dark) dots, which represent waves, appear on the fingers, as it can be seen in the cross section plots as well. The red(dark) dots keep forming, moving forward and interact with the capillary ridge in the fronts.

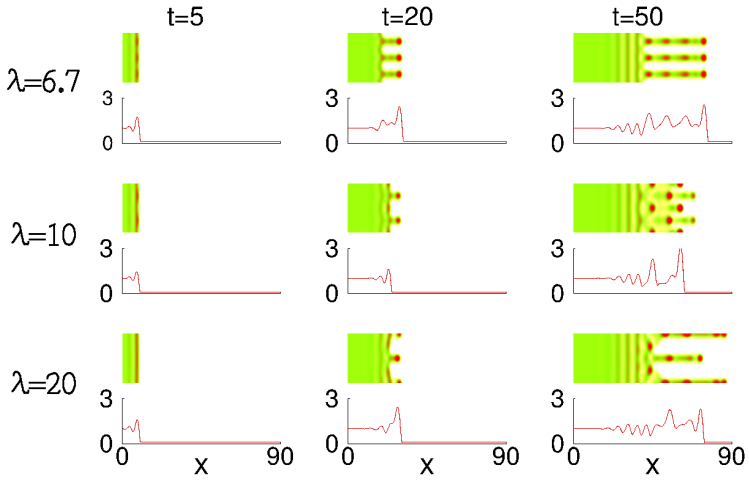

Figure 2.16 Time evolution for perturbations of different wavelengths (λ) at $D = -1.5$. The domain is chosen as $L = 90$ and $M = 20$. In each sub-block, the upper figure shows the contour plot, and the lower figure shows the cross section at $y = 10$.

The cross-sectional plots in Figure 2.16 show formation of solitary-like waves. Behind these solitary-like waves, there exists a second region where waves appear as 'stripes' (vis. the straight stripes in the middle part of the contour plot at $t = 50$). These stripe-waves move forward for a short distance and then break into several waves localized on the surface of the finger-like rivulets. In the cross-section plots, these strip-like waves appear as sinusoidal waves. Finally, a flat film is observed in the region far behind the contact line. The appearance of such a flat film indicates that the flow instability is of convective type. Therefore, for such D, the contact line induced waves are carried by the fluid and they eventually move away from any fixed position.

Figure 2.17 shows the numerical results for $D = -2.0$ with the same set of initial perturbations as in Figure 2.16. Both contour plots and the cross sections at

the middle of the y domain are presented. As mentioned in Section 2.2, $D = -2.0$ corresponds to the *Type 2* regime and is of absolute instability type. This is exactly what we see in the contour plot. Localized waves shown as red (dark) dots appear all over the surface and see neither strip waves nor flat film appearing. In the cross section plots, we only see solitary-like waves.

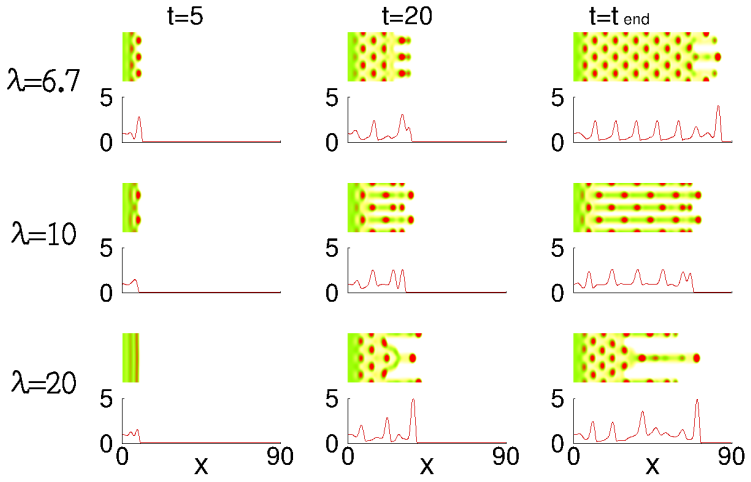

Figure 2.17 Time evolution for perturbations of different wavelengths (λ) at $D = -2.0$. $t_{end} = 50$ for $\lambda = 6.67$, $t_{end} = 40$ for $\lambda = 10$, $t_{end} = 30$ for $\lambda = 20$. The domain is chosen as $L = 90$ and $M = 20$. In each sub-block, the upper figure shows the contour plot, and the lower figure shows the cross section at $y = 10$.

Next, we proceed to analyze the behavior in the case where initially multiple perturbations are present. The imposed perturbation consists of 50 sinusoidal modes with amplitudes randomly selected from $[-0.2, 0.2]$

$$x_f(y) = x_{f0} - \sum_{i=1}^{50} A_i \cos((i-1)\,\pi\, y), \quad -0.2 \le A_i \le 0.2\,.$$

Figure 2.18 shows the simulations for different Ds with the same random initial perturbations, so that the nondimensional parameter D is the only difference between the four panels. The initial profile is also shown in Figure 2.18 ($t = 0$).

The first obvious observation is that the number of fingers increases as the absolute value of (negative) D becomes larger. This is due to the fact that the most unstable wavelength decreases as $|D|$ becomes larger. Therefore, more fingers

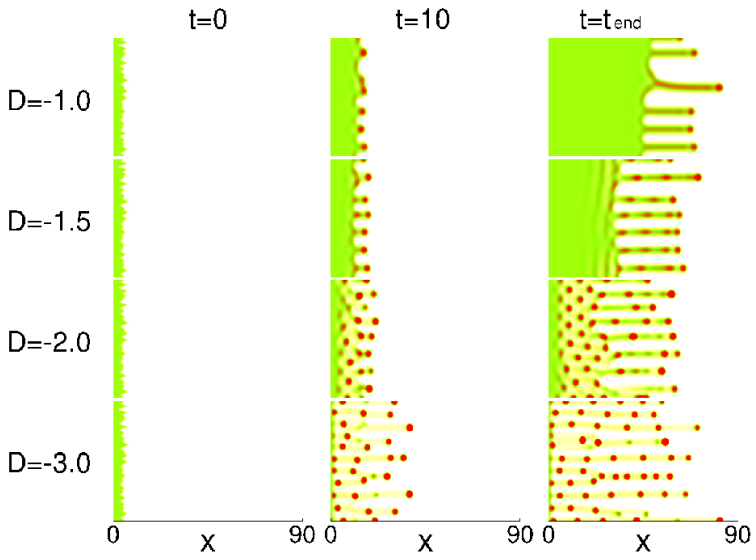

Figure 2.18 Time evolution of perturbations for different Ds with the same random initial perturbations. Here $t_{end} = 50$ for $D = -1.0$, $t_{end} = 40$ for $D = -1.5$, $t_{end} = 30$ for $D = -2.0$, $t_{end} = 20$ for $D = -3.0$. The domain is chosen as $L = 90$ and $M = 50$.

can fit into the flow domain. Secondly, the fingers become more narrow for these Ds, consistent with the predictions for rivulet flow. Thirdly, the absolute/convective instability argument is a good explanation for these contact line induced instabilities: there is no surface instability seen for $D = -1.0$; we see convective instability, shown as localized waves/stripes/flat film for $D = -1.5$; and absolute instability for $D = -2.0$ and $D = -3.0$.

Remark.

Here we comment on two additional sets of simulations - corresponding figures are omitted for brevity. One set involves the case when the initial condition is chosen as y-independent. Mathematically such an initial condition reduces the problem to 2D, and the solution should remain y-independent for all times. However, this is not the case in numerical simulations. Numerical errors are present and grow with time. To estimate this effect, one can calculate the largest growth rate in the x and y direction based on the LSA results, and estimate the time for which the numerical noise becomes significant. For example, for $D = -1.0$, the largest growth rate for

instability of a flat film in the x direction is 0.25 and the largest growth rate in the y direction is 0.46. That is, it takes 70 time units for noise of initial amplitude 10^{-16} (typical for double precision computer arithmetic) to grow to 10^{-2}. So as long as the final time is less than 70, the numerical noise is still not visible. By carrying out such an analysis, we are able to distinguish between the numerical noise induced instability and the contact line induced one, and further separate the effect of numerical noise.

The other set of simulations has to do with the case when the initial single mode perturbation is chosen as a stable one. In such a case, the amplitude of perturbation decays exponentially and the surface profile soon becomes y-independent. Again, after sufficiently long time, numerical noise will become relevant and break the y-independence.

2.3.2.3 The width of a finger. It is of interest to discuss how fingers' widths depend on D. As a reminder, the LSA shows that there exists a most unstable wavenumber, $q_m(D)$, and the distance between two neighboring fingers in physical experiments, in the presence of natural or other noise, is expected to center around the most unstable wavelength, $\lambda_m = 2\pi/q_m(D)$. On the other hand, the width of the rivulet part of a single finger is not known to the best of our knowledge. In the following we define this width and discuss how it relates to the LSA results.

We check whether there is a difference between the fingers for different single mode perturbations. Figure 2.19 shows the y-orientation cross section of the fingers' rivulet part for $D = -0.5$ and $D = -1.0$. As shown in this figure, for a given D, the fingers are very similar in the cross section, with their shape almost independent of the initial perturbation. Note that this result still holds even for the λ's that are very close to the critical value, $\lambda_c = 2\pi/q_c(D)$ - e.g., see $\lambda = 6.3$ in Figure 2.19(b) (here $\lambda_c \approx 6.25$). By direct comparison of the parts (a) and (b) of this figure, we immediately observe that the fingers are more narrow for more negative Ds.

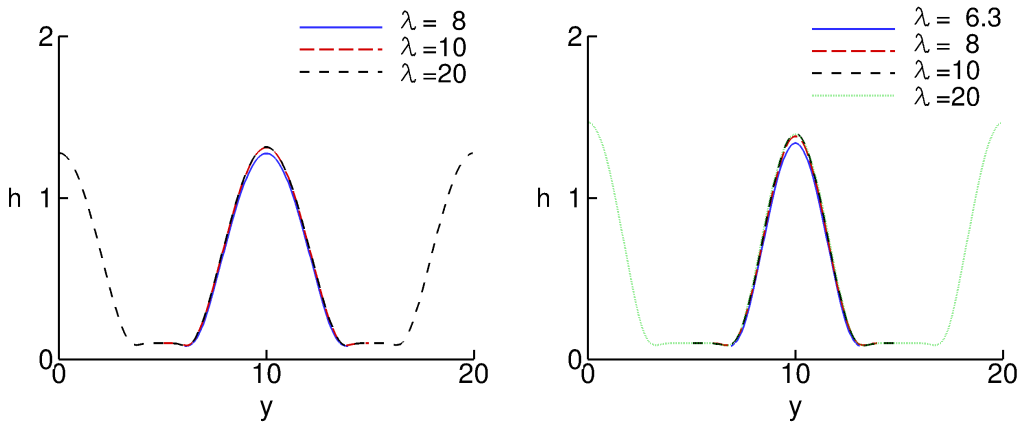

(a) $D = -0.5$. (b) $D = -1.0$.

Figure 2.19 Cross sections of film thickness as a function of the transverse coordinate, y, for different wavelengths of initial perturbation, λ. The cross sections are taken from the rivulet part of a finger, at $x = 35$, $t = 30$; some of results from which the cross sections are extracted can be seen in Figure 2.14. The centers of the cross sections are shifted to $y = 10$ for the purpose of comparison. For $D = -0.5$, $\lambda = 6.3$ is stable (not shown).

To make this discussion more precise, we define the width of a rivulet, w, as the distance between two dips on each side of a finger (the two dips are shown at $y \approx 7$ and $y \approx 13$ in Figure 2.19). *The main finding is that* $w \approx \lambda_c$. This finding applies for all Ds and all perturbation wavelengths that we considered. In particular note that Figure 2.19 shows that w becomes smaller as the absolute value of (negative) D increases, consistently with the decrease of λ_c, see Figure 2.13.

While it is clear that w cannot be larger than λ_c (since w is independent of the initial perturbation, and for $\lambda > \lambda_c$ it must be that $\lambda > w$), at this point we do not have a precise argument why w is so close to λ_c for all considered perturbations and the values of D. Of course, one could argue that $w \approx \lambda_c$ is also consistent with stability of any perturbation characterized by $\lambda < \lambda_c$, since such a perturbation cannot support a finger of width $w \approx \lambda_c$.

It should be pointed out that the fingers that we discuss in this Section differ from the analytical infinite rivulet solution derived in Section 2.3.1. For example,

as shown in Figure 2.19, the cross section of a finger with a front includes two dips on each side, that do not appear in the analytical solution of an infinite rivulet. Furthermore, the width of an infinite rivulet diverges as $D \to 0$, but we still observe fingers of finite width for $D = 0$. Such differences suggest that one should include nonlinear effects when considering properties of finger-like solutions.

2.3.3 Rayleigh-Taylor Instability of Inverted Film

The instabilities we have discussed so far arise in flow configurations where a contact line is present, and an obvious question is what happens if there is no contact line, that is, if we have an infinite film spreading down an (inverted) surface. This configuration is expected to be susceptible to Rayleigh-Taylor (R-T) type of instabilities, since we effectively have a heavier fluid (liquid) above a lighter one (air). The question is: What are the properties of this instability for a film flowing down an inverted surface, and how does this instability relate to the contact line induced one, discussed so far?

Figure 2.20 shows the results of 3D simulation of an infinite film (no contact line). The initial condition at $t = 0$ is chosen as a flat film with a localized hemispherical perturbation of amplitude 0.1 (marked by the black circle in Figure 2.20). As an example, we use $D = -1.0$. At time $t = 20$, the perturbation had been amplified, as expected. The properties of this instability are, however, very different from that observed in thin film flow where a contact line is present. For this D, if a contact line is present, we see only a capillary wave behind the front (vis. Figure 2.18), and we do not find upstream propagating waves as we do for the infinite film shown in Figure 2.20. Therefore, the instability discussed so far is not of R-T type - instead, it is induced by the presence of a contact line.

One obvious question is why we do not observe (additional) R-T instability in the flow with fronts. The answer is that the speed with which a perturbation on a main body of a film (such as the infinite film shown in Figure 2.20) propagates

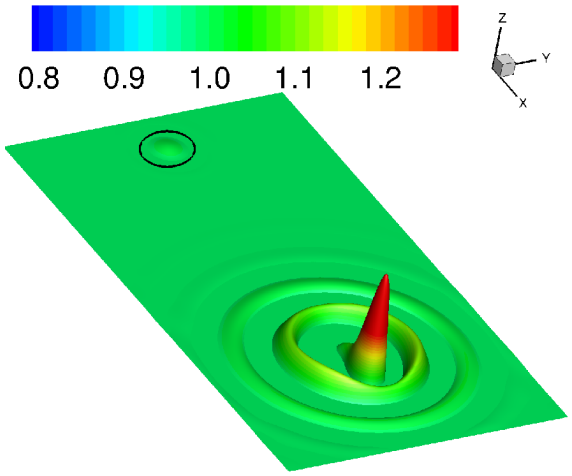

Figure 2.20 Simulation of Rayleigh-Taylor instability for hanging film on inclined plane at $D = -1.0$. The black circle indicates the initial profile. The surface shown in the downstream is the surface profile at $t = 20$. The computational domain is $[0, 90] \times [0, 50]$.

downstream is faster than the speed of the contact line itself. Therefore, in the simulations of films with fronts presented so far, flat film instabilities do not have time to develop since they reach the contact line before having a chance to grow. We note that in Figure 2.20 we used large scale perturbation to illustrate the point; in a physical problem, one would expect surface perturbations to be characterized by much smaller amplitudes and would therefore, require much longer time to grow to the scale comparable to the film thickness. As a consequence, R-T instability could be expected to become relevant only for films of spatially extend much larger than that considered here. A similar conclusion extends to stability of infinite rivulets, discussed briefly in Section 2.3.1.

2.3.4 Inverted Film of Variable Viscosity with a Front

Consider now a situation in which the film is of finite width and the fluid viscosity is variable in the transverse direction. We have the governing equation for the film

height

$$\frac{\partial h}{\partial t} + \nabla \cdot \left[\frac{h^3}{\bar{\mu}(y)} \left(\nabla \nabla^2 h - D \nabla h + \mathbf{i} \right) \right] = 0. \tag{2.28}$$

We have to substitute the symmetry boundary conditions, Equation (2.27), at the borders of the computational domain with the following ones

$$h(x, 0, t) = h(x, M, t) = b,$$

$$h_x(x, 0, t) = h_x(x, M, t) = 0.$$

The flow starts at the top of the domain according to the condition

$$h(0, y, t) = b + F_0 \left(\frac{y}{M} \right) \frac{(\beta t)^2}{1 + (\beta t)^2}, \tag{2.29}$$

where the value of parameter β is 0.775 and the bell shape of the entrance thickness profile determined by the function F_0 is shown in Figure 2.21. Equation (2.29) mimics the growth of the flow rate and the film thickness at the entrance boundary as the liquid starts being delivered to the substrate during the ramp-up in industrial processes or experiments. Characteristic patterns of flow depend on the value of the parameter D, the width of the film and the distribution of viscosity, and are establish when the product βt in Equation (2.29) reaches a value of several units.

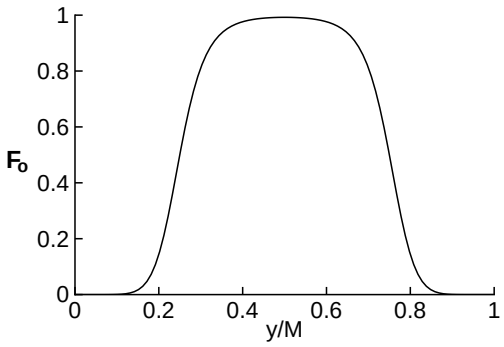

Figure 2.21 Entrance profile of film thickness in Equation (2.29).

In many practical situations, the variation of viscosity is a result of its dependence on temperature, which is usually nonlinear. For example, assume that the film temperature T decreases linearly with the lateral coordinate y and the viscosity is given by a generic equation

$$\log_{10}(\bar{\mu}) = -A_1 + \frac{A_2}{T - A_3}, \quad T = T_0 - A_4 y, \tag{2.30}$$

where $A_1 = -4.5$, $A_2 = 7000K$ and $A_3 = 520K$ are the material constants, and T is the liquid temperature. The viscosity function is normalized by its value at $y = 0$, and the constant value T_0 is taken as $1530K$. The lateral temperature drop across the computational domain, $A_4 M$, is $115K$ in all cases discussed hereafter, resulting in 7.5 fold viscosity growth from bottom to top of the domain.

Similar to the isoviscous cases discussed earlier, the film front is always unstable, producing finger-like rivulets. The morphology of the non-isoviscous film (as compared to an isoviscous case) stems from the fact that similar structures such as fingers at different parts of the film move with different speeds. As an example, Figures 2.22 (a) and (b) show distributions of film thickness at $t = 9.4$, 16.5, with parameter $D = -0.88$ and the dimensionless domain width M equal to 133. Morphology of individual fingers is similar to that of fingers in the isoviscous cases shown in Figure 2.18, but there is obvious mass redistribution along the front line because of its inclination, resulting in coalescence of some of the fingers and variation of the finger-to-finger distance. A finger produced by coalescence of two parent fingers, such as finger 5 in Figure 2.22(b) (circled), has a higher flow rate and moves faster than its neighbors.

These specific properties of non-isoviscous film are common for flows in the whole spectrum of parameter D, but morphology of individual fingers strongly depends on the type of the flow, similar to the isoviscous case considered already. Figure 2.23 shows the distribution of film thickness for parameter $D = -1.5$,

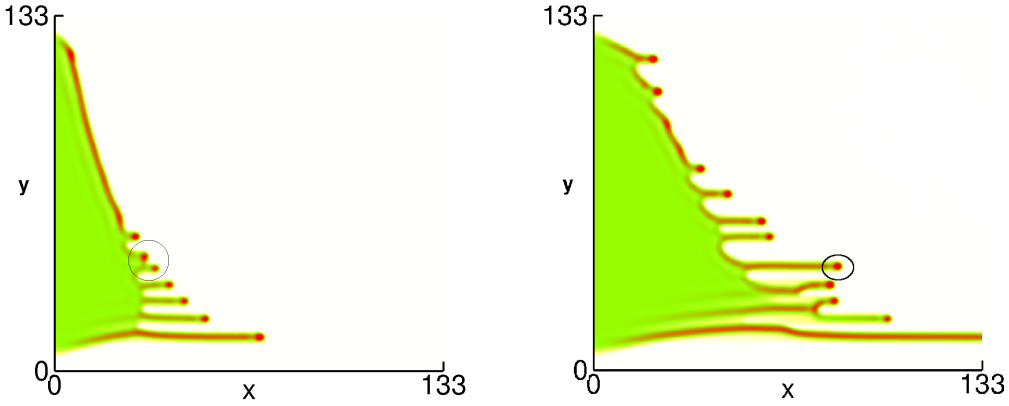

(a) $t = 9.4$. (b) $t = 16.5$.

Figure 2.22 Film thickness for $D = -0.88$. The circles in the part (a) and (b) indicates two coalescing fingers.

corresponding to *type 2*, with film width $M = 72.2$, at $t = 25.4$. The leading capillary ridges are followed by a rivulet with followup smaller waves moving faster than the leader. The pattern is common for all fingers, but the speed of propagation increases with temperature. Each of the fingers has a faster-moving neighbor on the higher temperature side, causing slight increase of the background film thickness on that side compared to the colder side. As a result, the fingers may have a tendency to divert and coalesce with warmer neighbors resulting in mass transport from colder areas to warmer areas of the flow, despite the fact that the film velocity does not explicitly depend on the temperature gradient.

In *type 3* film flow, the height of follow-up drops is already close to that of finger head drops, as shown in Figure 2.24, which shows the thickness distribution in the film at time $t = 44.4$, with parameter $D = -2.54$ and film width $M = 52.2$. In *type 3* flows, there is no propagation front and the flow itself consists of a series of propagating fingers. Another peculiarity of this type of flow is the existence of small drops, separating from the leading drops to be immediately consumed by the following drop in the train, as indicated by circles in Figure 2.24. These features are also observed in isoviscous flows for similar values of D; see, e.g., the cross-sectional

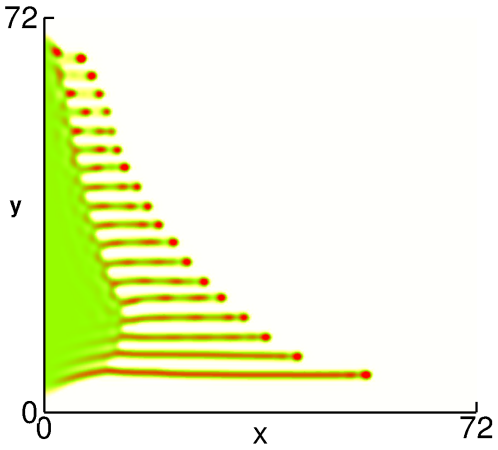

Figure 2.23 Film thickness for $D = -1.5$ at $t = 25.4$.

profile in Figure 2.17. The viscosity effect in the developed *type 3* flows shows mainly as the difference in speeds for droplets in low and high viscosity regions.

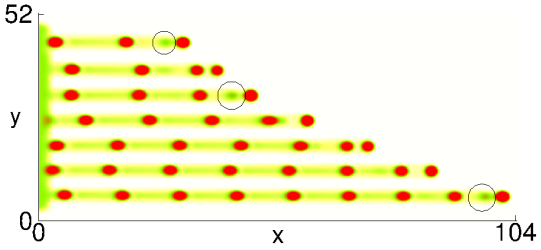

Figure 2.24 Film thickness for $D = -2.54$ at $t = 44.4$.

2.3.5 Conclusions

In Section 2.2, we carried out extensive computational and stability analysis of the two-dimensional flow of a completely wetting fluid down an inverted surface. Complex behavior was uncovered with different families of waves evolving in configurations characterized by different values of the governing parameter D. In the present work, we have considered the fully three-dimensional problem of spreading down an inverted surface. We find that there is an elaborate interaction of surface instabilities and contact line instabilities. For values of D that are not too small (approximately $D \geq$

-1.1) we find behavior similar to that already known for flow down an inclined surface, with the main difference that the finger-like patterns that form are spaced more closely and the fingers themselves are more narrow for negative Ds. As D decreased through negative values, we still find instabilities of the contact line leading to formation of fingers, but in addition we observe the formation of surface waves, which propagate down the fingers with speed larger than that of the fingers themselves: therefore, these propagation waves (which may appear as drops on top of the base film) travel down a finger, reach the front and merge with the leading capillary ridge. Behind the fingers, in this regime we find strip-like waves (whose fronts are independent of the transverse direction). These waves are convective in nature and leave behind a portion of a flat film whose length increases with time. For even smaller Ds (less than approximately -2.0), these transverse strip-like waves disappear, and the whole film is covered by localized waves. These localized waves travel faster than the film itself, and converge towards the fingers which form at the front.

It is worth emphasizing that the properties of the surface waves which form due to the presence of fronts are different from those that would be expected if the fronts were not present. To illustrate this effect, we consider an infinite film with a localized perturbation which is expected to be unstable by a Rayleigh-Taylor type of instability. We find that this instability leads to a different type of surface waves, which may or may not be observable in physical experiments, depending on the size of the fluid domain.

In the second part of the section, we consider flow where fluid viscosity is not constant, but varies in the transverse direction. The most important difference is the loss of flow periodicity in the lateral direction. The fingers in the warmer parts of the flow move faster than those in the colder areas, yielding a slight increase of the background film thickness on the warmer side of each finger compared to the colder side. This results in mass redistribution from colder areas to warmer areas of the

flow, more pronounced for lower values of $|D|$, despite explicit independence of the film velocity on the temperature gradient.

2.4 Partially Wetting Fluid

In this section, we study the spreading and dewetting process of films that partially wet a solid surface. In particular, we are interested in the regime where the van der Waals forces and gravitational forces are both relevant. We present the model and appropriate scalings in Section 2.4.1. We then perform analysis of a flat film in Section 2.4.2 to characterize linearly stable and unstable regimes. Numerical simulations of a film on a horizontal surface are shown in Section 2.4.3 as well as on an (inverted) inclined plane in what follows.

2.4.1 Thin Film Equation with Disjoining Pressure

We model partially wetting fluid by introducing the disjoining pressure in the thin film equation [27]. The model is written as (in dimensional form)

$$3\mu\frac{\partial\bar{h}}{\partial\bar{t}} + \bar{\nabla}\cdot\left(\gamma\bar{h}^3\bar{\nabla}\bar{\nabla}^2\bar{h} + \bar{h}^3\bar{\nabla}\Pi(\bar{h}) - \rho g\bar{h}^3\bar{\nabla}\bar{h}\cos\alpha + \rho g\bar{h}^3\sin\alpha\mathbf{i}\right) = 0, \qquad (2.31)$$

where μ is the viscosity, γ is the surface tension, ρ is the fluid density, g is the gravity and α is the inclination angle. The disjoining pressure model that we use,

$$\Pi(\bar{h}) = \kappa f(\bar{h}) = \kappa\left[\left(\frac{\bar{h}_*}{\bar{h}}\right)^n - \left(\frac{\bar{h}_*}{\bar{h}}\right)^m\right], \qquad (2.32)$$

introduces κ (proportional to the Hamaker constant) and the exponents $n > m > 1$. The first term represents liquid-solid repulsion, while the second term is attractive, leading to a stable film thickness $\bar{h} = \bar{h}_*$. Within this model, $\kappa = S/(M\bar{h}_*)$, where S is the spreading parameter and $M = (n-m)/[(m-1)(n-1)]$. The spreading parameter can be related to the apparent contact angle θ via the Laplace-Young condition $S = \gamma(1-\cos\theta)$.

2.4.1.1 Nondimensionalization. We define the scalings as

$$h = \frac{\bar{h}}{h_c}, \quad (x, y, t) = \left(\frac{\bar{x}}{x_c}, \frac{\bar{y}}{y_c}, \frac{\bar{t}}{t_c}\right), \quad t_c = \frac{3\mu}{\gamma}\frac{x_c^4}{h_c^3}, \tag{2.33}$$

where the choices of scalings will be discussed in Section 2.4.1.2. The nondimensional equation is then given by

$$\frac{\partial h}{\partial t} + \nabla \cdot [h^3 \nabla \nabla^2 h] + K \nabla \cdot [h^3 F(h) \nabla h] - D_c \nabla \cdot [h^3 \nabla h] + D_s \frac{\partial h^3}{\partial x} = 0, \tag{2.34}$$

where

$$F(h) = \frac{-n\, h_*^{n-m}}{h^{n+1}} + \frac{m}{h^{m+1}}, \quad h_* = \frac{\bar{h}_*}{h_c}, \tag{2.35}$$

and

$$K = \frac{\kappa \bar{h}_*^m x_c^2}{\gamma h_c^{m+1}}, \quad D_c = \frac{x_c^2}{a^2}\cos\alpha, \quad D_s = \frac{x_c^3}{a^2\, h_c}\sin\alpha, \tag{2.36}$$

with $a = \sqrt{\gamma/\rho g}$ being the capillary length.

2.4.1.2 Choice of Scalings. We want to consider the case where the contributions of van der Waals and gravitational forces are comparable. To have a balance between these two forces, we choose

$$h_c = a^{2/m}\, \bar{h}_*^{(m-1)/m}\, x_c^{-1/m}, \quad x_c = a^{(2m+2)/(3m+1)}\, \bar{h}_*^{(m-1)/(3m+1)}. \tag{2.37}$$

Under such scaling, the parameters that measure the relative importance of disjoining pressure, normal gravity and tangential gravity are:

$$K = \frac{1-\cos\theta}{M}, \quad D_c = \frac{x_c^2}{a^2}\cos\alpha, \quad D_s = \sin\alpha. \tag{2.38}$$

As an example, assuming $m = 2$, for fluids with capillary length $a \approx 10^{-3}m$ and precursor thickness $\bar{h}_* \approx 10^{-9}m$, we have $x_c \approx 10^{-4}m$, $h_c \approx 3 \times 10^{-6}m$, giving the characteristic scaling on film thickness as about $3\mu m$.

In the following, for convenience, we fix the parameters $n = 3$, $m = 2$, so that

$$F(h) = \frac{2h - 3h_*}{h^4}. \tag{2.39}$$

2.4.2 Linear Stability Analysis of a Flat Surface

Here we consider the two-dimensional planar case, and study the effect of small perturbations of the free surface. (Also, from this point onwards, only 2D films will be considered.) Equation (2.34) reduces to

$$\frac{\partial h}{\partial t} + \frac{\partial}{\partial x}\left[h^3\left(\frac{\partial^3 h}{\partial x^3} + K\,F(h)\,\frac{\partial h}{\partial x} - D_c\,\frac{\partial h}{\partial x} + D_s\right)\right] = 0. \tag{2.40}$$

Setting $h = h_0 + \xi$ where $\xi \ll 1$, we have

$$\xi_t = -h_0^3\xi_{xxxx} - Kh_0^3F(h_0)\xi_{xx} + D_ch_0^3\xi_{xx} - 3D_sh_0^2\xi_x. \tag{2.41}$$

Assuming further that $\xi = \exp(i(kx - \omega t))$ with $\omega = \omega_r + i\omega_i$, we find

$$\omega_r = 3D_sh_o^2k, \quad \omega_i = -h_0^3(k^4 + (D_c - KF(h_0))k^2). \tag{2.42}$$

These two expressions tell us that the regime of instability is determined by the sign of $(D_c - KF(h_0))$. As an example, for $h_0 \gg h_*$, we have $F(h_0) \approx 2/h_0^3$. Therefore, a flat film of thickness h_0 is unstable if $D_c < 2K/h_0^3$. On the other hand, the precursor film, $h_0 = h_*$, is unstable if $D_c < -K/h_*^3$.

2.4.2.1 Absolute and Convective Stability Analysis. For an unstable film, $D_c - KF(h_0) < 0$, we can perform the absolute and convective stability analysis. The change of variables

$$\eta = \sqrt{-D_c + KF(h_0)}\,\left(x - 3D_s\,h_0^2\,t\right), \quad \tau = h_0^3\,(-D_c + KF(h_0))^2\,t$$

in Equation (2.41) leads to

$$\xi_\tau + \xi_{\eta\eta\eta\eta} + \xi_{\eta\eta} = 0.$$

The front velocities (velocity of the boundary of local disturbance, as mentioned in Section 2.2.4.2) of this equation have been determined by Chang et al. [15] to be ± 1.62. Therefore, the front velocities of perturbed partially wetting films, governed by Equation (2.41), are

$$3\,D_s\,h_0^2 \pm 1.62\,h_0^3\,(-D_c + K\,F(h_0))^{3/2}. \tag{2.43}$$

Finally, if $3\,D_s\,h_0^2 - 1.62\,h_0^3\,(-D_c + K\,F(h_0))^{3/2} \leq 0$, the range of influence of any perturbation will eventually cover the whole film, and the film exhibits absolute instability.

2.4.3 Thin Films on a Horizontal Surface

2.4.3.1 Infinite Film. For films on a horizontal surface, $\alpha = 0$, we have $D_s = 0$ and $D_c = (x_c/a)^2$. The criterion for a flat film of thickness $h = h_0$ to be unstable is that

$$\left(\frac{x_c}{a}\right)^2 < K\,\frac{2h_0 - 3h_*}{h_0^4}. \tag{2.44}$$

So very thin and very thick films are stable. In particular, films with thickness $h_0 \leq 3h_*/2$ are always stable. On the other hand, there exists a range of thicknesses where instabilities are possible. Figure 2.25 shows the stability diagram for film thickness versus contact angle. For a completely wetting fluid, films of infinite widths are stable for any thickness. However, for a partially wetting film, there exists a range of unstable film thicknesses.

2.4.3.2 Finite Film. Figure 2.26 shows the evolution of a finite 2D film on a horizontal surface. As discussed in [27], there are two types of dewetting mechanisms in the linearly unstable regime: surface instability dominated [Figure 2.26 (a)] and nucleation instability dominated [Figure 2.26 (b)]. In general, thick

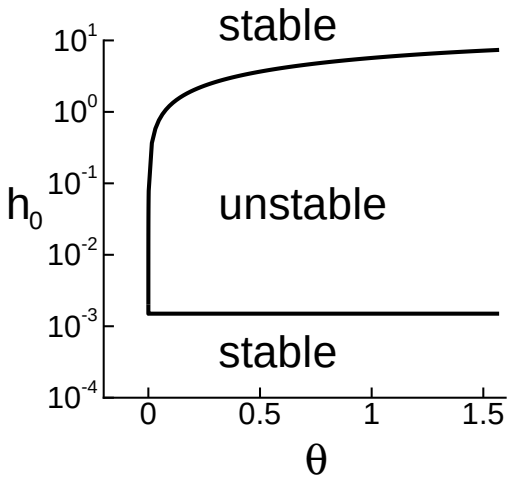

Figure 2.25 Stability diagram for an infinite film at horizontal surface, $\alpha = 0$. The parameters are chosen as $x_c/a = 0.1$ and $h_* = 0.001$. Note also that the precursor film is always stable.

films experience nucleation dewetting while thin films experience spinodal dewetting (surface instability dominated).

2.4.4 Falling Film with a Front

In this section, we consider a film of partially wetting fluid flowing down an inclined plane enclosing an angle α with the horizontal, as a natural extension to those discussed in Section 2.2. We first consider the constant volume films in Section 2.4.4.1. We further consider the films with constant flux configuration in Section 2.4.4.2.

2.4.4.1 Constant Volume. We consider the evolution of films of finite width on an inclined plane. Figure 2.27 shows the evolution of a finite film on a vertical surface, $\alpha = 90°$. The parameters are chosen to be the same as in Figure 2.26 (b) except for the inclination angle. We see that in this example the time scale for the film to break up is faster than the time scale for the film to move downward (positive x direction). Therefore, the number of droplets observed after the process of breaking up is the same as for the horizontal surface (vis. Figure 2.26 (b)). The

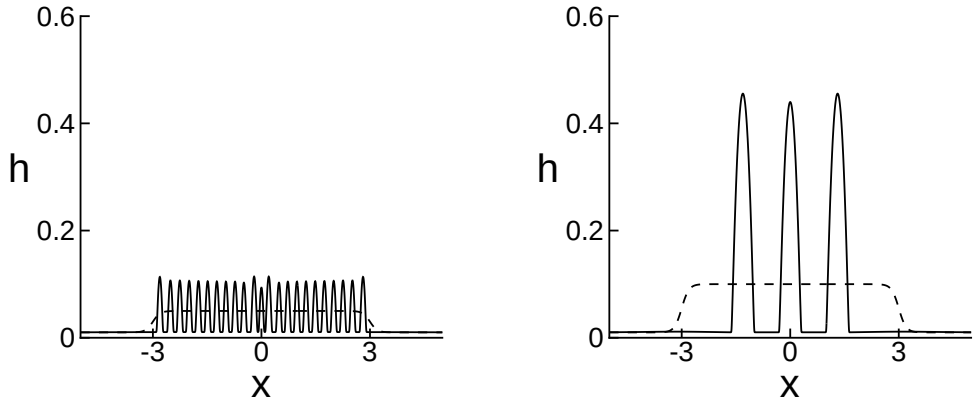

(a) $h_0 = 0.05$ (b) $h_0 = 0.1$

Figure 2.26 Numerical simulations of dewetting finite films on a horizontal surface. Dashed line shows the initial condition and the solid line shows the film thickness at $t = 10$. Parameters are chosen as: $K = 0.1$, $h_* = 0.01$, $D_c = 0.01$ and $D_s = 0$. The most unstable wavelength corresponding to the film $h_0 = 0.05$ is 0.27, while the most unstable wavelength is 0.68 for $h_0 = 0.1$.

other observation is that a drop with larger volume moves faster. Once a drop catches another one they merge, forming a bigger drop. Finally, by time $t = 30$ all drops have merged into one, which moves forward with a constant speed.

One should note that the instabilities considered here are different from the "pearling" instabilities observed in the tail of a sliding droplet [53], where the trailing edge of the droplet could be a rounded, smooth contact line, a corner, or a cusped tail that emits smaller drops. Such phenomena are apparently three-dimensional and will be explored in the future.

2.4.4.2 Constant Flux. Here we consider a film flowing down an inclined surface with constant flux at the inlet, $x = 0$. The boundary condition is imposed by specifying

$$h(0)^3 D_s = 1, \quad h_{xxx}(0) + KF(h(0))h_x(0) - D_c h_x(0) = 0. \tag{2.45}$$

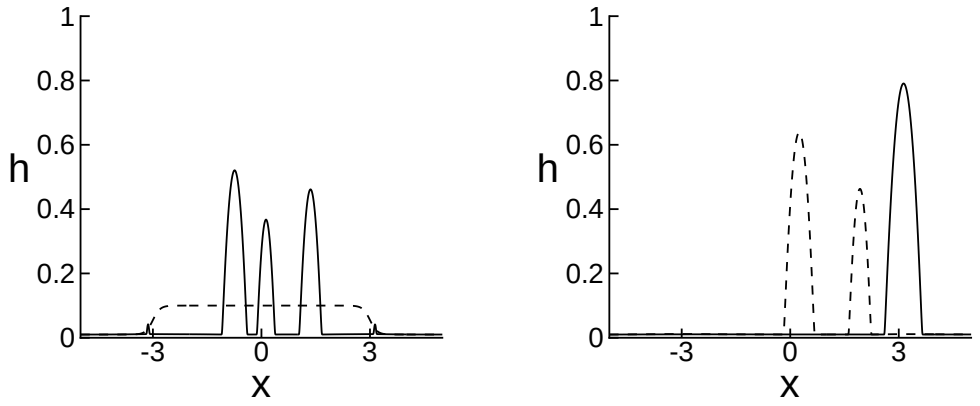

(a) $t = 0$ (dashed); $t = 2$ (solid) (b) $t = 10$ (dashed); $t = 30$ (solid)

Figure 2.27 Numerical simulations of falling finite films. Parameters are chosen as: $K = 0.1$, $h_* = 0.01$, $D_c = 0$ and $D_s = 1$.

Based on such settings, the film thickness at the inlet is not the same for simulations with different substrate inclination angle, α. It changes with respect to the inclination angle to ensure a constant flux. At the outlet, we assume that the film thickness is equal to the precursor, so that

$$h(L,t) = h_*, \quad h_x(L,t) = 0, \tag{2.46}$$

where L is the domain size.

2.4.4.2.1 Traveling Wave Solution. Setting $s = x - Ut$ in Equation (2.40), a traveling wave $H(s) = h(x,s)$ must satisfy

$$-UH + [H^3(H''' + KFH' - D_cH' + D_s)] = c.$$

Imposing the boundary conditions at infinity as $H(x = -\infty) = h_0$ and $H(x = \infty) = b$ we obtain $c = -D_s(h_0^2\, b + h_0\, b^2)$ and $U = D_s(h_0^2 + h_0\, b + b^2) \approx (D_s)^{1/3}$.

According to the above analysis and based on the discussion in Section 2.2.4.2, the contact line may influence the film behind it if $D_c - KF(h_0) < 0$ and if

$$2\,D_s\,h_0^2 < 1.62 h_0^3(-D_c + KF(h_0))^{3/2}.$$

2.4.4.2.2 Stability Diagram. Figure 2.28 shows the stability diagram for a film of partially wetting fluid flowing down an inclined plane, based on the results in Section 2.4.2 and in Section 2.4.4.2.1. Note that the line $K = 0$ corresponds to the completely wetting fluid. The region between the curve $K = 0$ and the red solid curve is the linearly stable regime ($D_c - KF(h_0) > 0$). The region between the red solid curve and the green dashed curve (for $0 \leq \alpha \leq 90°$) and the region between the curve $K = 0$ and the green dashed curve (for $90° < \alpha \leq 180°$) are the nonlinearly stable regime. In this regime, the contact line is not able to influence the film behind it. The profile of the film will either be a traveling wave solution or take the form of a train of periodic droplets. For the region between the green dashed curve and dotted blue curve is the convective instability regime. The traveling wave will not exist in this regime. Finally, the region outside the dotted blue curve is the absolute instability regime. Any kind of local disturbance will grow and expand to cover the whole film.

As we can see in Figure 2.28, the curves change dramatically when the inclination angle approaches horizontal (0° or 180°). In Figure 2.29, we have shown the zoom in of these two regions ($0° < \theta < 1°$ and $179° < \theta < 180°$). For a partially wetting fluid (fixed contact angle θ), a flat film becomes more stable as the inclination angle α approaches 0°; while as $\alpha \to 180°$, the film becomes more unstable.

Figure 2.30 shows the evolution of vertically falling films with different contact angles. Note that both cases lie in the nonlinearly stable regime, we do not expect any surface waves to appear. For small contact angle, $K = 0.3$, we observe a stable traveling wave solution. In addition, a dewetting process takes place during the early

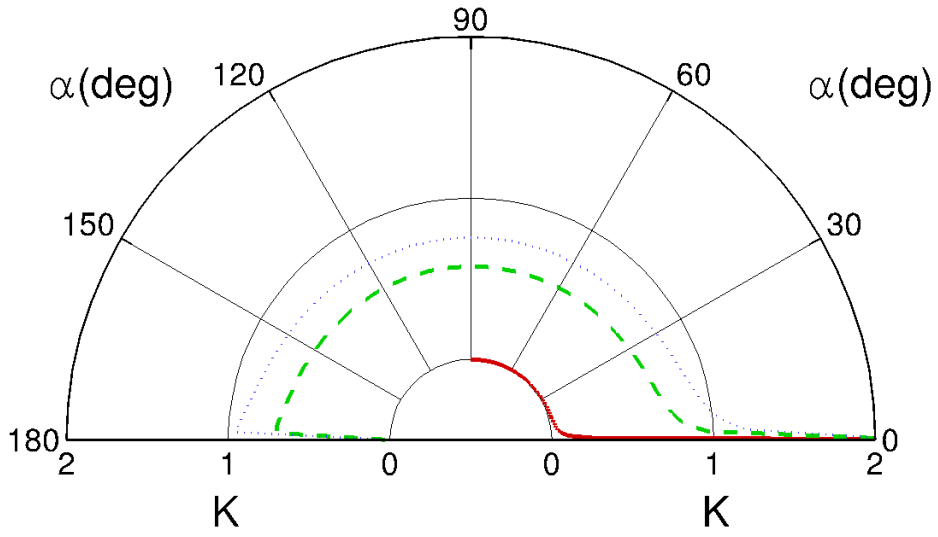

Figure 2.28 Stability diagram for a partially wetting fluid flowing down a possibly inverted incline. Here, $h_* = 0.001$. Parameter K, defined by Equation 2.38, reflects the influence of the contact angle; α is the inclination angle.

stage of evolution. The contact line is initially placed at $x = 50$ and at first moves backward (dewetting) until $t = 3$. Only then does it advance, and a traveling wave solution is formed.

For larger contact angle ($K = 0.5$), in addition to dewetting, we observe film breakup, illustrated in Figure 2.30 (b). At $t = 11$ the film breaks up into two parts

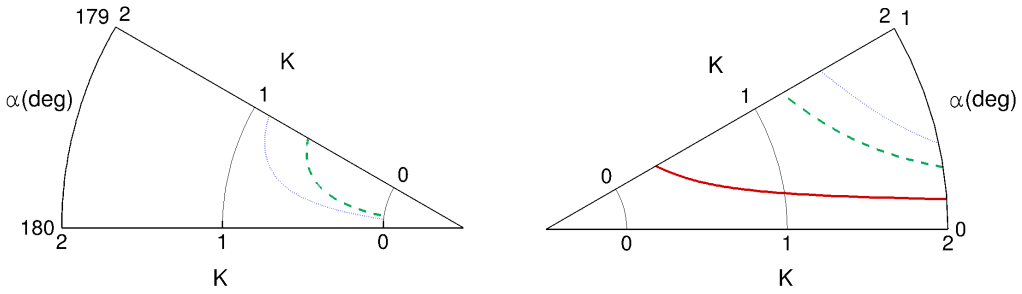

Figure 2.29 Zoom-in version of Figure 2.28.

behind the capillary ridge. The detached portion at the front moves forward as a single droplet, while the portion connected to the main film dewets again.

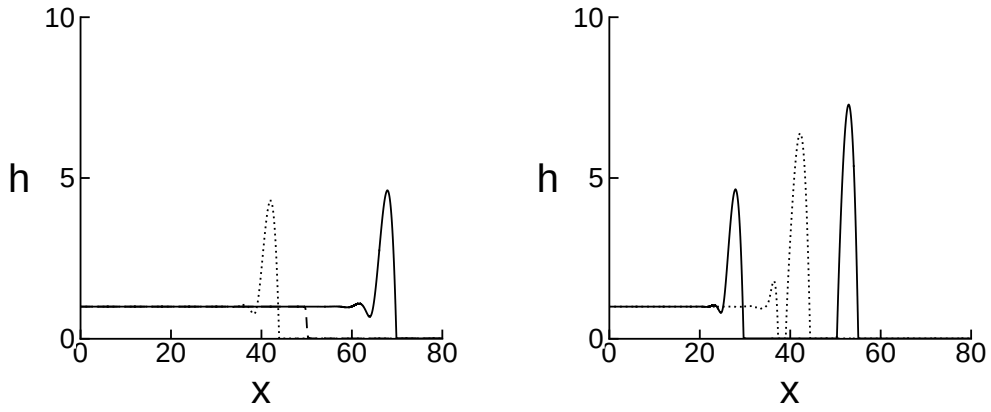

(a) $K = 0.3$ (b) $K = 0.5$

Figure 2.30 Evolution of a partially wetting fluid with constant flux boundary condition. The initial condition are the same for both cases, shown as a dashed line in (a). For $K = 0.3$, the dotted line corresponds to $t = 3$ and solid line is $t = 30$. For $K = 0.5$, the dotted line corresponds to $t = 11$ and solid line is $t = 12$. Parameters are chosen as: $h_* = 0.01$, $D_c = 0$, $D_s = 1$.

We have found in simulations that, for $\sin\alpha = O(1)$, the breakup of a film occurs in the nonlinearly stable regime (between the red solid curve and the green dashed curve in Figure 2.28). As a result, we do not observe surface instabilities since there is no flat film after the film breaks up. On the other hand, this mechanism of breakup is of interest and will require further investigation.

CHAPTER 3

SPREADING NEMATIC LIQUID CRYSTAL DROPLETS

3.1 Introduction

The coating of a thin film of nematic liquid crystal (NLC) onto a substrate is one stage in the manufacture of liquid crystal display devices. For example, a recent experimental study [10] on coating/falling flows in the nematic phase was motivated by the search for improved manufacturing techniques for NLC microdisplay components. We refer readers to [52], which discusses many intriguing features of liquid crystals, and to [13, 24] for more in-depth reviews of liquid crystal phenomenology.

Coating may be unstable: In a series of beautiful and surprising experiments in [54], Poulard & Cazabat observed remarkable spontaneous instabilities in droplets of nematic liquid crystal (5CB, pentyl-cyanobiphenyl) spreading on hydrophilic silicon substrates under conditions of high relative humidity. The authors found that the drops could either remain stable without spreading [Figure 3.1 (a)], spread stably [Figure 3.1 (b)], or spread while destabilizing [Figure 3.1 (c)-(e)]. The major factors influencing the behavior appear to be the relative humidity (RH) at which the experiment is carried out, and the droplet size: qualitatively speaking, at low RH ($< 40\%$) no spreading is observed [Figure 3.1 (a)]; at intermediate RH ($40\% < \text{RH} < 60\%$) stable spreading is seen [Figure 3.1 (b)]; for $60\% < \text{RH} < 80\%$ instabilities develop at the moving contact line, (and in the free upper surface of the droplet) [Figure 3.1 (c)]; and for $\text{RH} > 80\%$ a second (longer wavelength) instability is manifested [Figure 3.1 (d)]. In general, small droplets are reported to be stable however, even at high RH; while larger droplets can be unstable as observed above. Curiously, all contact line instabilities are observed to fade away at very large times,

as spreading ceases. In addition, defects (discontinuities of the *director field*, the unit vector describing the local average direction of the molecules of the NLC) appear always to accompany instabilities, but at this stage their role in the instability development is unclear: whether defects induce the instabilities, are induced by them, or some other explanation altogether, is still an open question.

As is apparent, despite the simplicity of the experimental setup, the observed behavior is remarkably complex, and our challenge is to find a minimal plausible model capable of exhibiting such behavior in different parameter regimes.

We follow [6, 20] to derive a simple model describing the free surface evolution of a thin film of NLC on a rigid substrate. The derivation is based on standard long wave theory. The improvements in the model here permit fully nonlinear time-dependent simulations. In particular, our model enables us to simulate instabilities that occur at the contact line. These simulations are compared with experimental results of Poulard & Cazabat [54]. We have found qualitative agreement and believe that this model is a good starting point for a description of spreading NLC droplets.

3.2 Model Derivation

The main dependent variables governing the dynamics of a liquid crystal in the nematic phase are the velocity field $\bar{\boldsymbol{v}} = (\bar{u}, \bar{v}, \bar{w})$, and director field $\boldsymbol{n} = (n_1, n_2, n_3)$, the unit vector describing the orientation of the anisotropic axis in the liquid crystal (an idealized representation of the local preferred average direction of the rodlike liquid crystal molecules). The director is a function of space and time, which is determined by minimizing a suitably-defined free energy $\bar{W}$ within the NLC, with coupling to the local flow-field. Molecules like to align locally, and this preference is modeled by an elastic energy, which is minimized subject to boundary conditions. In general, a bounding surface is associated with a given preferred direction for $\boldsymbol{n}$; this preference is known as surface anchoring, and is modeled by an appropriate choice of

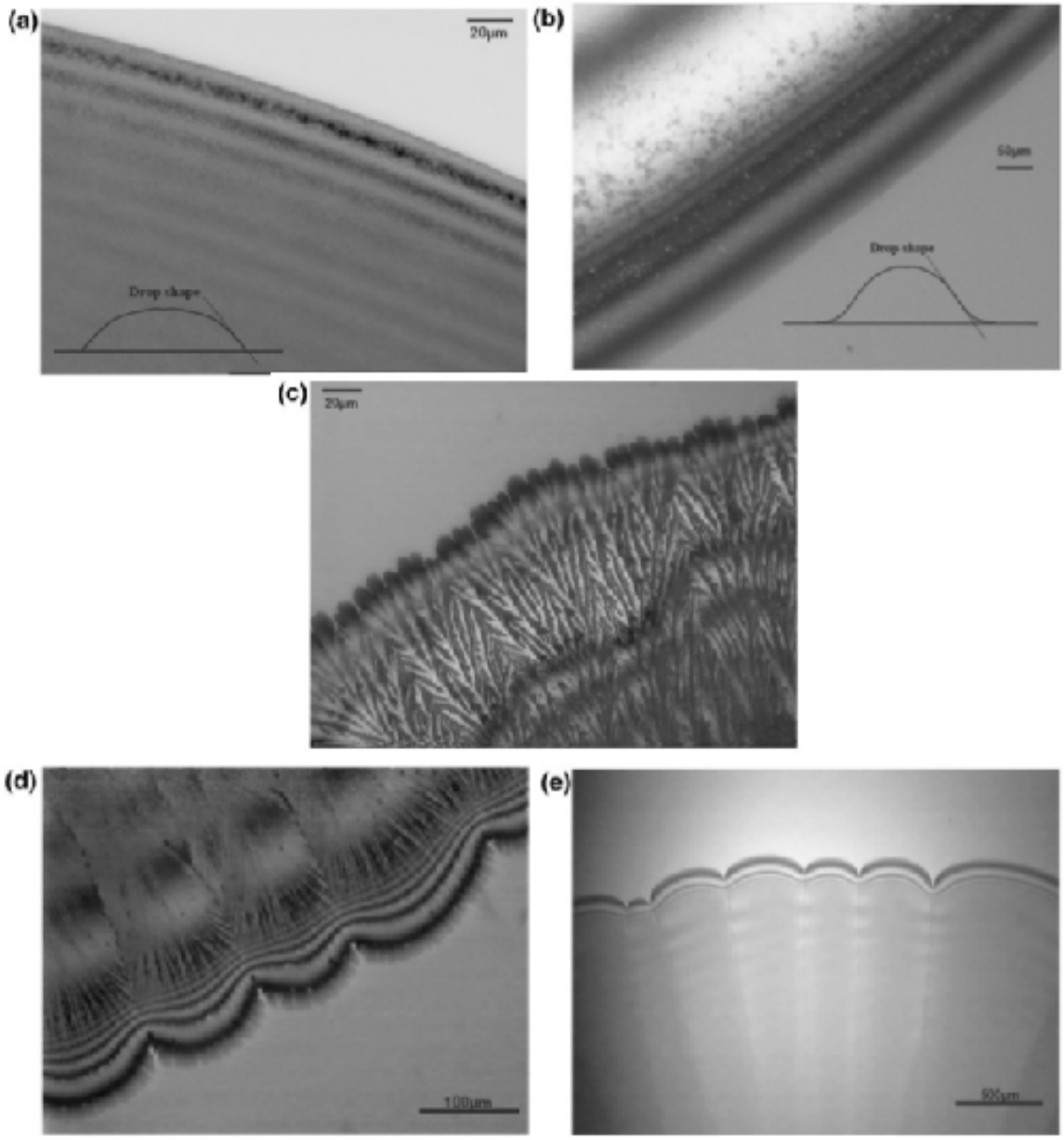

Figure 3.1 Experimental photos reproduced from Poulard & Cazabat [54]. Full details are given in [54], but in summary, (a) shows a stable, non-spreading droplet of 5CB at 20% relative humidity (RH); (b) shows a stable spreading droplet at 50% RH; (c) shows a spreading unstable droplet at 80% RH, with corrugated free surface and fingering at the apparent contact line; and (d) shows another unstable spreading droplet at yet higher RH 90%. In (d) a second, longer-wavelength instability appears alongside the first, and in (e) only this second instability is present.

surface energy. Anchoring can be tuned by appropriate treatment of a surface and may be either weak or strong.

3.2.1 Leslie-Ericksen Equations

The flow of nematic liquid crystal is described by the Leslie-Ericksen equations [39]. Neglecting inertia effects, the flow is governed by

$$\lambda n_i - \frac{\partial \bar{W}}{\partial n_i} + \left(\frac{\partial \bar{W}}{\partial n_{i,j}}\right)_{,j} + \tilde{G}_i = 0, \tag{3.1}$$

$$-\Pi_{,i} + \tilde{G}_k n_{k,i} + \tilde{t}_{ij,j} = 0, \tag{3.2}$$

$$\frac{\partial \bar{v}_i}{\partial \bar{x}_i} = 0. \tag{3.3}$$

representing energy, momentum and mass conservation, respectively. Here, λ is a Lagrange multiplier ensuring that the director $\boldsymbol{n}$ is a unit vector; $\bar{W}$ is the bulk elastic (Frank) energy and an overdot denotes differentiation with respect to time t. The quantities $\bar{W}$, $\tilde{G}$ and Π are defined by

$$2\bar{W} = K\left((\bar{\nabla}\cdot\boldsymbol{n})^2 + |\bar{\nabla}\wedge\boldsymbol{n}|^2\right); \tag{3.4}$$

$$\tilde{G}_i = -\gamma_1 N_i - \gamma_2 \bar{e}_{ik} n_k, \quad \bar{e}_{ij} = \frac{1}{2}\left(\frac{\partial \bar{v}_i}{\partial \bar{x}_j} + \frac{\partial \bar{v}_j}{\partial \bar{x}_i}\right); \tag{3.5}$$

$$N_i = -\dot{n}_i - \bar{\omega}_{ik}\, n_k, \quad \bar{\omega}_{ij} = \frac{1}{2}\left(\frac{\partial \bar{v}_i}{\partial \bar{x}_j} - \frac{\partial \bar{v}_j}{\partial \bar{x}_i}\right); \tag{3.6}$$

$$\Pi = \bar{p} + \bar{W} + \psi_g, \tag{3.7}$$

where K is an elastic constant, γ_1 and γ_2 are constant viscosities; $\bar{p}$ is the pressure and ψ_g is the gravitational potential. Finally, $\tilde{t}_{ij}$ is the extrastress tensor, given by

$$\tilde{t}_{ij} = \alpha_1 n_k n_p \bar{e}_{kp} n_i n_j + \alpha_2 N_i n_j + \alpha_3 N_j n_i + \alpha_4 \bar{e}_{ij} + \alpha_5 \bar{e}_{ik} n_k n_j + \alpha_6 \bar{e}_{jk} n_k n_i, \tag{3.8}$$

where α_i are constant viscosities (related to γ_i in Equation (3.5) by $\gamma_1 = \alpha_3 - \alpha_2$, $\gamma_2 = \alpha_6 - \alpha_5$, and to each other by the Onsager relation, $\alpha_2 + \alpha_3 = \alpha_6 - \alpha_5$), and $\mu := \alpha_4/2$ corresponds to the usual viscosity in the standard Newtonian case, when all other α_i are zero.

3.2.2 Nondimensionalisation

We make the usual lubrication scalings to nondimensionalize the governing equations:

$$(\bar{x}, \bar{y}, \bar{z}) = (Lx, Ly, \delta Lz), \quad (\bar{u}, \bar{v}, \bar{w}) = (Uu, Uv, \delta Uw), \tag{3.9}$$

$$\bar{t} = \frac{L}{U}t, \quad \bar{p} = \frac{\mu U}{\delta^2 L}p, \quad \bar{W} = \frac{K}{\delta^2 L^2}, \tag{3.10}$$

where L is the lengthscale of typical variations in the x and y directions, U is the typical flow speed; $\delta = h_0/L \ll 1$ is the aspect ratio of the film based on a typical film height h_0, and $\mu = \alpha_4/2$ was chosen as the representative viscosity scaling in the pressure, since this corresponds to the usual viscosity in the isotropic case.

3.2.3 Energy Equation

It is found in [6, 20] that by choosing the time scale appropriately, the coupling effect, $\tilde{G}$ in Equation (3.1)-(3.2), between the director field and velocity field can be neglected. The energy equation simply reduces to the appropriate static Euler-Lagrange equations for minimizing the free energy of the film subject to the constraint $\boldsymbol{n}\cdot\boldsymbol{n} = 1$. Imposing the constraint directly, we have a director field that is an arbitrary vector on the unit sphere,

$$\boldsymbol{n} = (\sin\theta\cos\phi, \sin\theta\sin\phi, \cos\theta) \tag{3.11}$$

for some functions $\theta(x, y, z, t)$ and $\phi(x, y, z, t)$, where ϕ is the azimuthal angle of the direction $\boldsymbol{n}$ about the axis $\theta = 0$.

The leading order elastic energy in the bulk, under lubrication scalings, is given by

$$2W = \theta_z^2 + \phi_z^2 \sin^2\theta + O(\delta). \tag{3.12}$$

The surface energy at the free surface $z = h(x, y, t)$ is denoted by $\mathcal{G} = \mathcal{G}(\hat{\theta})$ where $\hat{\theta}$ is the director orientation at the free surface. It is related to the director orientation θ by the relation

$$\hat{\theta} = \theta(z = h(x, y, t)). \tag{3.13}$$

The energy is a minimum when the director aligns in the preferred orientation $\hat{\theta} = 0$ (homeotropic surface anchoring). On the other hand, at the substrate we assume the anchoring is strong and the director always stay planar. That is, $\theta(z = 0) = \pi/2$.

We carry out the free energy minimization directly using a variational principle. The free energy J is made up of contributions from the bulk, and from surface effects. We write

$$J = \int_0^h \int_{\Omega(t)} W \, dV dz + \int_{\Omega(t)} \mathcal{G} \, dV, \tag{3.14}$$

where $\Omega(t)$ is the domain occupied by the liquid crystal sample in the x-y plane.

We then consider the variation induced in the energy J by small variations in the fields θ and ϕ. The first variation must vanish at a minimum and the second variation tells us whether or not we have an energy minimum. The Euler-Lagrange problem of minimizing J (subject to appropriate boundary conditions) is then given by

$$\theta_{zz} = \frac{\phi_z^2}{2} \sin 2\theta \qquad \text{in } \Omega, \tag{3.15}$$

$$(\phi_z \sin^2\theta)_z = 0 \qquad \text{in } \Omega, \tag{3.16}$$

with boundary conditions coming from the first variation: $\phi_z \sin^2\theta = 0$ on $z = h$. Therefore, we have $\phi_z \equiv 0$, ie., $\phi = \phi(x, y, t)$. We will assume strong anchoring on ϕ at the substrate $z = 0$ to close the problem. For θ, we then have $\theta_{zz} = 0$, which leads to

$$\theta = a(x, y, t)\, z + \frac{\pi}{2}. \tag{3.17}$$

The function a has to be determined by the boundary condition of first variation,

$$\mathcal{G}_{\hat{\theta}} + \theta_z(z = h) = 0. \tag{3.18}$$

It is worth noting that the most commonly-used weak anchoring model, given by the Rapini-Papoular surface energy [1] cannot be applicable in the vicinity of a contact line [21]. (Such an approach introduces an extra "nematic" term into the standard thin film equation for $h = O(1)$ and is not well-defined for $h \ll 1$.) Instead, we propose that the change in the director angle across the fluid layer, ah, approaches 0 as the film thickness $h \to 0$. We introduce an ad hoc anchoring condition based on specifying this change in director angle by the formula,

$$ah = \Theta\, m(h), \tag{3.19}$$

where $m(h)$ is a monotone increasing function of h with $m(0) = 0$ and $m(\infty) = 1$, Θ is the difference in the preferred angle between the free surface and solid substrate. With our assumption of homeotropic alignment at the free surface, $\Theta = -\pi/2$.

The physical rationale behind the ad hoc anchoring is that, when the film is relatively thick, ($h \gg 1$, so that $m(h) \approx 1$) it is easy for the director to adjust to the preferred angles at each interface by bending across the film. However, as the film gets thin, and in particular near contact lines, there is a very large energy penalty

[1] $\mathcal{G} = A \sin^2(\theta - \theta_0)$ where A is the anchoring strength and θ_0 is the preferred angle.

to pay for bending between two fixed angles across a very short distance h. Thus, it should be such that $ah \approx 0$ for very thin films and $ah \approx \Theta$ for thick films.

There are many possible forms we could choose for $m(h)$ that satisfy our basic requirement; we take

$$m(h) = \frac{h^{3/2}}{h^{3/2} + \beta^{3/2}}, \tag{3.20}$$

where β is a constant. It is easy to verify that $m(0) = 0$ and $m(\infty) = 1$. However, Equation (3.20) is chosen particularly such that $m \approx h^{3/2}$ for $h \ll 1$. Under such conditions we find that that a very thin film remains isotropic while thick films are nematic [29]. This relation can be clearly seen later in the full evolution equation.

One should note that even though we do not specify the surface energy $\mathcal{G}$ in the derivation of director orientation θ, it is implicitly imposed in our anchoring condition, Equation (3.20). In fact, one can recover the appropriate surface energy easily. Based on Equation (3.18) (recall that $\hat{\theta}$ is simply the director angle θ evaluated on the free surface, given by Equation 3.13), we have

$$-\left(-\frac{\pi}{2}\frac{m(h)}{h}\right) = -a = \frac{d\mathcal{G}}{d\hat{\theta}} = \frac{d\mathcal{G}}{dh}\frac{dh}{d\hat{\theta}} = \frac{\frac{d\mathcal{G}}{dh}}{-\frac{\pi}{2}m'(h)}, \tag{3.21}$$

so that

$$\frac{\partial \mathcal{G}}{\partial h} = -\frac{\pi^2}{4}\frac{m(h)m'(h)}{h}. \tag{3.22}$$

Integration of this equation tells us how the surface energy $\mathcal{G}$ varies, on the free surface, as the free surface height changes.

Similarly, we have

$$\frac{\partial \mathcal{G}}{\partial \hat{\theta}} = \frac{1}{\beta}\left(\left(\frac{\pi}{2} - \hat{\theta}\right)\hat{\theta}^2\right)^{\frac{1}{3}}. \tag{3.23}$$

We can easily see that there is only one minimum of the surface energy, occurring at $\hat{\theta} = 0$. The energy increases as the director angle goes from 0 to $\pi/2$ and reaches its maximum at $\hat{\theta} = \pi/2$. One can think of the quantity $1/\beta$ as the surface anchoring

strength. For weak anchoring, $\beta \gg 1$ and $\mathcal{G}$ is approximately a constant. That is, there is no preferred angle at the surface. For strong anchoring, $\beta \ll 1$, it is more energetically favorable to stay at the minimal energy, $\hat{\theta} = 0$.

3.2.4 Momentum Equation

For the momentum equation, Equation (3.2), the balance of dominant terms are

$$\frac{\partial \pi}{\partial x} \sim \frac{\partial \tilde{t}_{13}}{\partial z}, \quad \frac{\partial \pi}{\partial y} \sim \frac{\partial \tilde{t}_{23}}{\partial z}.$$

On the other hand, based on lubrication scalings and to leading order, we have

$$\tilde{t}_{13} = (A\cos^2\phi + B)\, u_z + C\, v_z, \quad \tilde{t}_{23} = C\, u_z + (A\sin^2\phi + B)\, v_z, \tag{3.24}$$

where $A = 2\alpha_1 \sin^2\theta\cos^2\theta + (\alpha_3+\alpha_6)\sin^2\theta$, $B = 1 + (\alpha_5 - \alpha_2)\,\cos^2\theta$, $C = A\sin\phi\cos\phi$, and the α_i have been normalized by $\alpha_4/2$. As a result, the leading order equations are

$$\frac{\partial p}{\partial x} + \mathcal{N}\frac{\partial W}{\partial x} = \frac{\partial}{\partial z}\left\{(A\cos^2\phi + B)\, u_z + C\, v_z\right\}, \tag{3.25}$$

$$\frac{\partial p}{\partial y} + \mathcal{N}\frac{\partial W}{\partial y} = \frac{\partial}{\partial z}\left\{C\, u_z + (A\sin^2\phi + B)\, v_z\right\}, \tag{3.26}$$

$$\frac{\partial p}{\partial z} = -\mathcal{B}, \tag{3.27}$$

where $\mathcal{B} = \delta^3 \rho g L^2/\mu U$ is the Bond number and $\mathcal{N} = K/\mu U L$ is the inverse Ericksen number.

As in Newtonian flows, we assume that the normal component of the stress vector at the free surface balances surface tension times curvature, and that the in-plane component of the stress vector is balanced by surface tension (surface energy) gradients in the plane of the surface. With the stress tensor $t_{ij} = -p\,\delta_{ij} + \tilde{t}_{ij}$ this

yields the leading order boundary conditions:

$$p = -\mathcal{C}\nabla^2 h, \qquad \text{on } z = h(x,y,t), \tag{3.28}$$

$$(A\cos^2\phi + B)\,u_z + C\,v_z = \mathcal{N}\mathcal{G}_x, \qquad \text{on } z = h(x,y,t), \tag{3.29}$$

$$C\,u_z + (A\sin^2\phi + B)\,v_z = \mathcal{N}\mathcal{G}_y, \qquad \text{on } z = h(x,y,t). \tag{3.30}$$

We can then solve Equations (3.27)-(3.28) for p to obtain

$$p = \mathcal{B}(h - z) - \mathcal{C}\nabla^2 h.$$

Substituting p in Equations (3.25)-(3.26), we can solve for u_z and v_z using the boundary conditions, Equations (3.29)-(3.30), derived above:

$$\begin{aligned} D\,u_z &= (A\sin^2\phi + B)\left((p_x + \mathcal{N}W_x)(z-h) + \mathcal{N}\mathcal{G}_x\right) \\ &\quad -C\left((p_y + \mathcal{N}W_y)(z-h) + \mathcal{N}\mathcal{G}_y\right), \\ D\,v_z &= (A\cos^2\phi + B)\left((p_y + \mathcal{N}W_y)(z-h) + \mathcal{N}\mathcal{G}_y\right) \\ &\quad -C\left((p_x + \mathcal{N}W_x)(z-h) + \mathcal{N}\mathcal{G}_x\right), \end{aligned}$$

where $D = AB + B^2$. Finally, using conservation of flux together with the relations

$$\int_0^h u\,dz = \int_0^h u_z(h-z)\,dz, \quad \int_0^h v\,dz = \int_0^h v_z(h-z)\,dz,$$

we obtain a partial differential equation governing the evolution of the film height:

$$\begin{aligned} h_t \;+\; & \frac{\partial}{\partial x}\left[\left(\mathcal{C}(\nabla^2 h)_x - \mathcal{B}h_x - \mathcal{N}W_x\right)(\sin^2\phi\,\mathfrak{f}_1 + \mathfrak{f}_3) + \mathcal{N}\mathcal{G}_x(\sin^2\phi\,\mathfrak{f}_2 + \mathfrak{f}_4)\right. \\ & \left. -\left(\mathcal{C}(\nabla^2 h)_y - \mathcal{B}h_y - \mathcal{N}W_y\right)\mathfrak{f}_5 - \mathcal{N}\mathcal{G}_y\mathfrak{f}_6\right] \\ +\; & \frac{\partial}{\partial y}\left[\left(\mathcal{C}(\nabla^2 h)_y - \mathcal{B}h_y - \mathcal{N}W_y\right)(\cos^2\phi\,\mathfrak{f}_1 + \mathfrak{f}_3) + \mathcal{N}\mathcal{G}_y(\cos^2\phi\,\mathfrak{f}_2 + \mathfrak{f}_4)\right. \\ & \left. -\left(\mathcal{C}(\nabla^2 h)_x - \mathcal{B}h_x - \mathcal{N}W_x\right)\mathfrak{f}_5 - \mathcal{N}\mathcal{G}_x\mathfrak{f}_6\right] = 0, \end{aligned} \tag{3.31}$$

where

$$\mathfrak{f}_1 = \int_0^h \frac{A(h-z)^2}{B(A+B)}\,dz, \quad \mathfrak{f}_2 = \int_0^h \frac{A(h-z)}{B(A+B)}\,dz, \quad \mathfrak{f}_3 = \int_0^h \frac{(h-z)^2}{A+B}\,dz,$$

$$\mathfrak{f}_4 = \int_0^h \frac{h-z}{A+B}\,dz, \quad \mathfrak{f}_5 = \sin\phi\cos\phi\mathfrak{f}_1, \quad \mathfrak{f}_6 = \sin\phi\cos\phi\mathfrak{f}_2.$$

To further simplify the model, we linearize the the nonlinear terms ($A \approx \alpha_3+\alpha_6$ and $B \approx 1$) to have

$$\mathfrak{f}_1 = -2\nu\,h^3, \quad \mathfrak{f}_2 = -3\nu\,h^2, \quad \mathfrak{f}_3 = (\lambda+\nu)\,h^3, \quad \mathfrak{f}_4 = \frac{3(\lambda+\nu)}{2}\,h^2, \quad \mathfrak{f}_5 = -\nu\sin 2\phi\,h^3,$$

$$\mathfrak{f}_6 = -\frac{3\nu\sin 2\phi}{2}\,h^2, \quad \nu = -\frac{\alpha_3+\alpha_6}{6(1+\alpha_3+\alpha_6)}, \quad \lambda = \frac{2+\alpha_3+\alpha_6}{6(1+\alpha_3+\alpha_6)}.$$

With these approximated quantities, the equation can be further rewritten in a compact form as

$$h_t + \nabla\cdot\left[h^3\tilde{\nabla}\left(\mathcal{C}\nabla^2 h - \mathcal{B}h - \mathcal{N}W\right) + \frac{3}{2}h^2\tilde{\nabla}\left(\mathcal{N}\mathcal{G}\right)\right] = 0, \tag{3.32}$$

where the operator $\tilde{\nabla}$ is defined as

$$\tilde{\nabla} = \left(\lambda I + \nu\begin{bmatrix}\cos 2\phi & \sin 2\phi\\ \sin 2\phi & -\cos 2\phi\end{bmatrix}\right)\cdot\nabla. \tag{3.33}$$

In Section 3.2.3, we derived the bulk elastic energy, W, and surface energy, $\mathcal{G}$, as a function of film thickness h based on our chosen anchoring condition. This leads to

$$h_t + \nabla\cdot\left[h^3\tilde{\nabla}\left(\mathcal{C}\nabla^2 h - \mathcal{B}h\right) + \mathcal{N}\left(m^2 - \frac{5}{2}hmm'\right)\tilde{\nabla}h\right] = 0. \tag{3.34}$$

Note that we have rescaled $\mathcal{N}$ again for simplification. ($\mathcal{N}$ in Equation 3.34 equals $\mathcal{N}\Theta^2$ in Equation 3.32.)

As mentioned before, for very thin films, $h \ll 1$, the function $m(h)$ in our anchoring condition may be written as $m(h) = (h/\beta)^{3/2}$. Therefore, for small h we have the evolution equation as

$$h_t + \nabla \cdot \left[h^3 \tilde{\nabla} \left(\mathcal{C} \nabla^2 h - \left(\mathcal{B} + \frac{11}{4\beta^3} \mathcal{N} \right) h \right) \right] = 0. \tag{3.35}$$

That is, the extra "nematic" terms reduce to the same form as the gravity term. So the model admits solutions that are regular at a contact line; such drops would simply be expected to spread faster than the Newtonian equivalents. On the other hand, the anchoring condition at the substrate, ϕ, is still effective. The film experiences different forces of director orientation at the substrate. We will discuss this influence in the following sections.

3.2.5 NLC Evolution Equation

Our final model consists of the PDE, Equation (3.34), with $m(h)$ given by Equation (3.20) and $\tilde{\nabla}$ given by Equation (3.33). We have seven dimensionless parameters: λ, ν, $\mathcal{C}$, $\mathcal{B}$, $\mathcal{N}$, β and h_0. The solution space is potentially very large. In the following analysis and simulations, we assume a balance between surface tension and gravity, setting $\mathcal{C} = \mathcal{B} = 1$. We also assume that $\lambda = 1$ and $\nu = 2/3$, which correspond to $\alpha_3 + \alpha_6 = -4/5$.

3.3 Influence of Surface Anchoring

In this section, we analyze the influence of surface anchoring on the flow. We assume $\nu = 0$ and only consider the two-dimensional case ($y = 0$). The evolution equation can then be written as

$$h_t + \left[h^3 \left(h_{xxx} - h_x \right) + \mathcal{N} \left(m^2 - \frac{5}{2} h m m' \right) h_x \right]_x = 0. \tag{3.36}$$

3.3.1 Linear Stability Analysis

We begin by considering linear stability analysis of a uniform film, $h(x,t) = h_0$. Assuming $h = h_0 + \xi$, where $|\xi| \ll 1$, we find

$$\xi_t + h_0^3 \left[\xi_{xxxx} - \xi_{xx} + \mathcal{N}M(h_0)\xi_{xx}\right] = 0, \quad M(h_0) = \frac{h^{3/2} - \frac{11}{4}\beta^{3/2}}{\left(h^{3/2} + \beta^{3/2}\right)^3}. \tag{3.37}$$

By putting $\xi \sim \exp(ikx + \omega t)$, we obtain the dispersion relation

$$\omega = -h_0^3 \left[k^4 + (1 - \mathcal{N}M(h_0))k^2\right]. \tag{3.38}$$

As a result, we have instability of the flat film to sufficiently long-wavelength perturbations if $\mathcal{N}M(h_0) > 1$. When this is the case, perturbations with wavenumbers $k \in (0, k_c)$ are unstable, where $k_c = \sqrt{\mathcal{N}M(h_0) - 1}$ is the critical wavenumber, and the fastest-growing wavenumber is $k_m = \sqrt{(\mathcal{N}M(h_0) - 1)/2}$, with wavelength

$$\lambda_m = \frac{2\pi}{k_m} = \frac{2\pi}{\sqrt{(\mathcal{N}M(h_0) - 1)/2}}, \tag{3.39}$$

and growth rate $\omega_m = h_0^3(\mathcal{N}M(h_0) - 1)^2/4$.

3.3.2 Simulation of Spreading Droplets

Although our stability analysis is valid only for a flat film, and thus is not strictly applicable to a spreading drop of the kind in the experiments, we expect to be able to extract qualitative predictions for spreading drop simulations. Our numerical experiments bear out this expectation: for all simulations we have carried out (including many more than are shown here) we find that flat film linear stability analysis is an excellent indicator of stability properties of the droplets considered. For a spreading droplet there is of course no precise definition of h_0, the film height in the linear stability analysis, but in all our simulations we consider a 2D droplet whose initial shape is close to a rectangle (though with smoothed corners), of variable height h_0.

To illustrate the drop evolution for different values of the parameters we refer to our stability diagrams for $\mathcal{N} = 10$, Figure 3.2. Flat films are unstable for small β, which corresponds to stronger anchoring at the free surface. There exists a critical value, $\beta_c = 0.22\mathcal{N}^{1/3}$. For β larger than this critical value, there is no instability for any film thickness. On the other hand, for β smaller than the critical value, there exists a range of unstable films. In general, very thin films and thick films are stable.

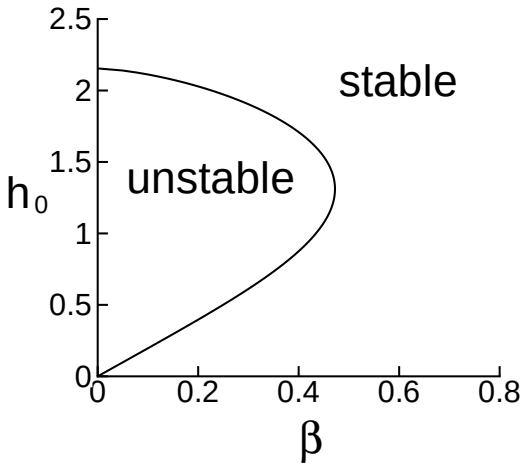

Figure 3.2 Stability diagram of flat NLC film for $\mathcal{N} = 10$.

We also carry out simulations of the PDE (3.36) showing drop evolutions with $\mathcal{N} = 10$. Numerical simulations are performed using a finite difference method, as discussed in Appendix B with precursor thickness $b = 0.01$. Figures 3.3 and 3.4 show stable spreading droplets, while Figure 3.5 shows an unstable spreading droplet.

In Figure 3.3, we see perhaps the simplest case of a stable spreading drop, with behavior similar to the Newtonian case. Also note that the drop spreads faster than its Newtonian equivalent ($\mathcal{N} = 0$), as predicted by Equation (3.35). Figure 3.4 shows another spreading drop, with the thickness high enough to be in the stable region. In this case, no instability is observed during drop spreading. In addition, there appears

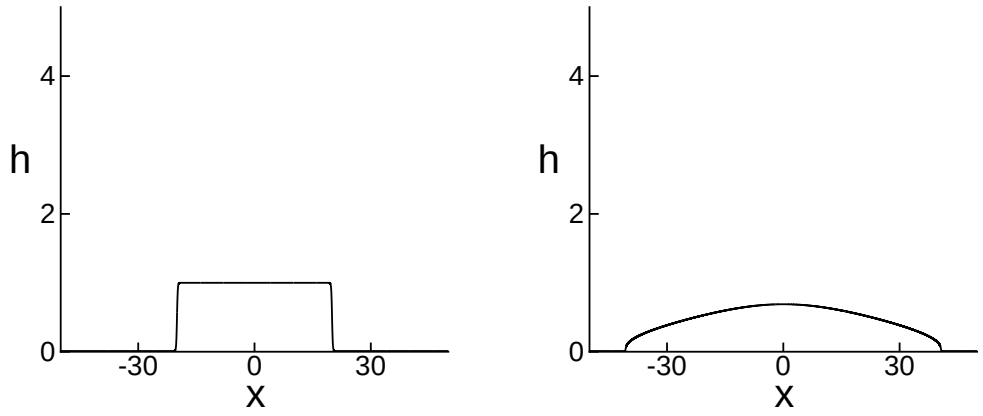

(a) $t = 0$ (b) $t = 100$

Figure 3.3 Evolution of a stably spreading NLC droplet: $\beta = 0.6$, $h_0 = 1$ and $\mathcal{N} = 10$.

to be a well-defined thickness, such that the portion of the drop below this thickness spreads, while the upper part of the drop essentially stands still.

Figure 3.5 shows the evolution when (h_0, β) fall into the unstable region. In the early stages of evolution, the initial single drop evolves into a drop with 10 humps. As the drop spreads, the humps merge, and eventually disappear.

3.3.3 Defect Modeling of Spreading 2D Droplets

As mentioned in the paper of Poulard & Cazabat [54], defects (discontinuities of the director field) appear to always accompany instabilities. But at this stage their role in the instability development is unclear: whether defects induce the instabilities, are induced by them, or some other explanation altogether, is still an open question. In this section, we extend the 2D model, Equation (3.36), to investigate the influence of defects. Our approach is to derive a 'smoothed' model of a defect in the continuum model, in which the director field varies continuously, but abruptly, in the region of the supposed defect.

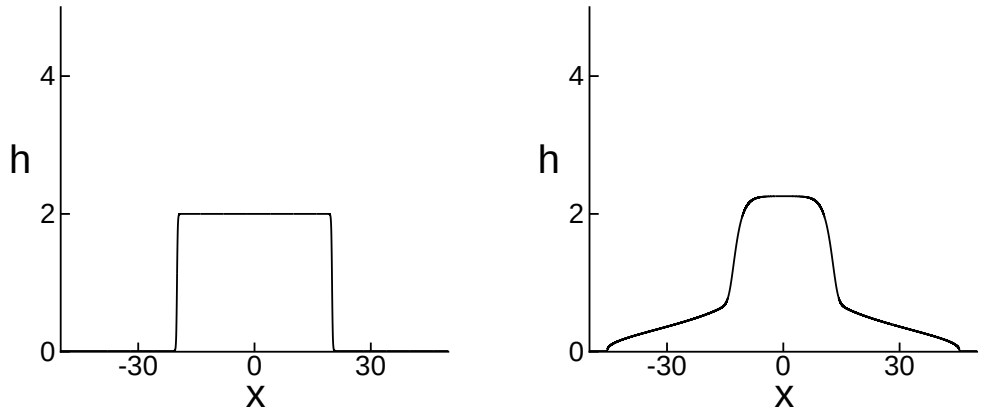

(a) $t = 0$ (b) $t = 100$

Figure 3.4 Evolution of a stably spreading NLC droplet: $\beta = 0.4$, $h_0 = 2$ and $\mathcal{N} = 10$.

We model a simple 2D defect by assuming that $\Theta = \Theta(x)$ (the difference in the preferred angle between free surface and solid substrate) has (smoothed) discontinuities at specific locations; instead of, only "pinned" defects that do not move within the layer are considered here. Figure 3.6 shows two possible defect configurations in two-dimensions: a point defect, where the director is discontinuous at a single point, and a line defect, where the discontinuity is along a line. Reverting to dimensional coordinates $(\bar{x}, \bar{z})$ momentarily it is clear that, for an idealized 2D line defect along $\bar{x} = 0$, the director angle θ is linear in $\bar{z}$ away from the actual discontinuity (the sign of the linear multiplier of $\bar{z}$ changes as we cross the discontinuity). An idealized 2D point defect at $(0, 0)$, in contrast, is described locally by $\theta \approx -\tan^{-1}(\bar{x}/\bar{z})$ (recall that θ is the angle the director makes with the vertical, and by convention is negative when $\bar{x} > 0$). At fixed distance $\bar{x} = \bar{X}$, and for $\bar{z} \ll |\bar{X}|$, this is approximated by $\theta \approx \mp\pi/2 + \bar{z}\bar{X}$. For films thinner than the defect outer core size [60], this linear approximation (where the sign of the linear multiplier again changes as the defect is crossed and $\bar{X}$ changes sign) is valid everywhere outside the core; therefore, for sufficiently thin films, 2D point and line defects are asymptotically equivalent since

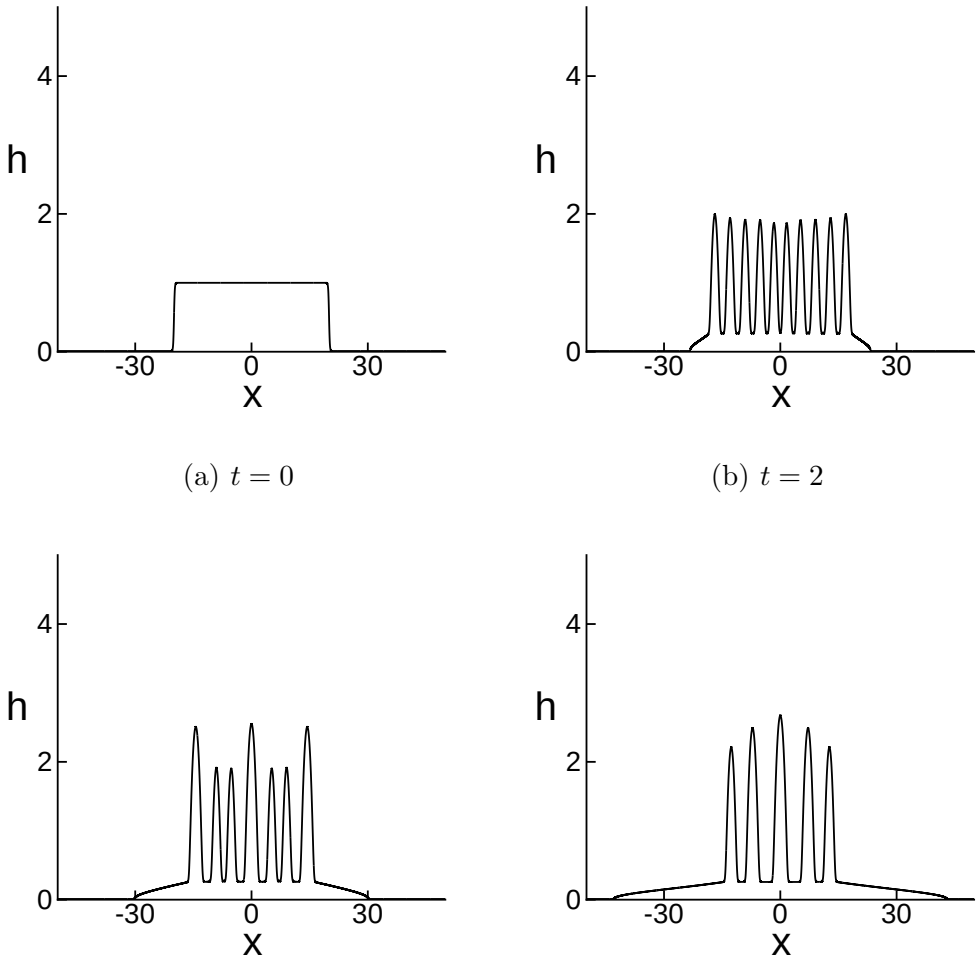

(a) $t = 0$ (b) $t = 2$

(c) $t = 20$ (d) $t = 100$

Figure 3.5 Evolution of an unstably spreading NLC droplet: $\beta = 0.2$, $h_0 = 1$ and $\mathcal{N} = 10$.

both have the same linear dependence of director angle on the vertical coordinate. In the spirit of using a 2D model to qualitatively represent 3D reality, we suggest that these idealizations can give insight into the behavior of 3D line and point defects [47].

Since defects are often associated with substrate inhomogeneities, we assume they are fixed and pre-existing. To model the change of director orientation across a defect, we assume that the difference Θ between the preferred normalized anchoring

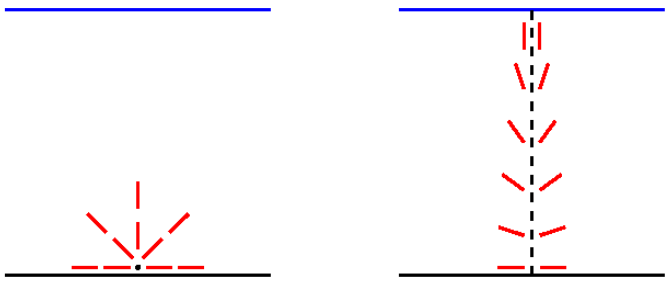

(a) Point defect, (b) line defect, in 2D drop.

Figure 3.6 Schematic of the two defect types considered. The solid (blue) top curve indicates the free surface of a droplet, the solid (black) bottom curve indicates the solid substrate, short (red) lines represent the director field orientation, and the black point-dashed line indicates the defect location.

angles at the two interfaces changes smoothly from -1 to $+1$ via the prescription

$$\Theta(x) = \tanh\left(\frac{x - x_0}{w}\right), \tag{3.40}$$

where x_0 is the position and w is the effective dimensionless width of the defect (corresponding to a dimensional defect core width wL [60]). To the left of the defect, where $x_0 - x \gg w$, the director turns through a normalized angle (-1) across the film, while to the right of the defect where $x - x_0 \gg w$ it turns through a normalized angle $(+1)$. In our simulations, we choose $w = 0.1$; the above defect formulation will be valid within the lubrication approximation provided $\delta \ll w$. Multiple defects, which are often observed, can be modeled by replacing Equation (3.40) by a superposition of hyperbolic tangents. Finally, we have the PDE governing the flow of a thin film containing a single defect fixed at $x = x_0$ as

$$\frac{\partial h}{\partial t} + \frac{\partial}{\partial x}\left[h^3(h_{xxx} - h_x) + \mathcal{N}\Theta^2\left(m^2 - \frac{5}{2}hmm'\right)h_x - \mathcal{N}\Theta\Theta_x m^2 h\right] = 0, \tag{3.41}$$

with $m(h)$ and $\Theta(x)$ given by Equations (3.20) and (3.40), respectively.

Figure 3.7 shows a stable spreading scenario ($\mathcal{N} = 10$, $\beta = 0.6$ and $h_0 = 1$). Figures 3.7(a) and (c) show the chosen initial condition (smoothed rectangle) and numerical results, respectively, at $t = 20$ with a defect at $x_0 = 3$. Consistent with LSA in Section 3.3.1, there is no free surface instability; however, in Figure 3.7(b) a small crest appears at the defect location [24]. This crest (the free surface gradient changes smoothly but abruptly; over the lengthscale $w \gg \delta$) appears to be a robust feature of our simulations with defects. Note the change in anchoring function $\Theta(x)m(h)$ across a defect.

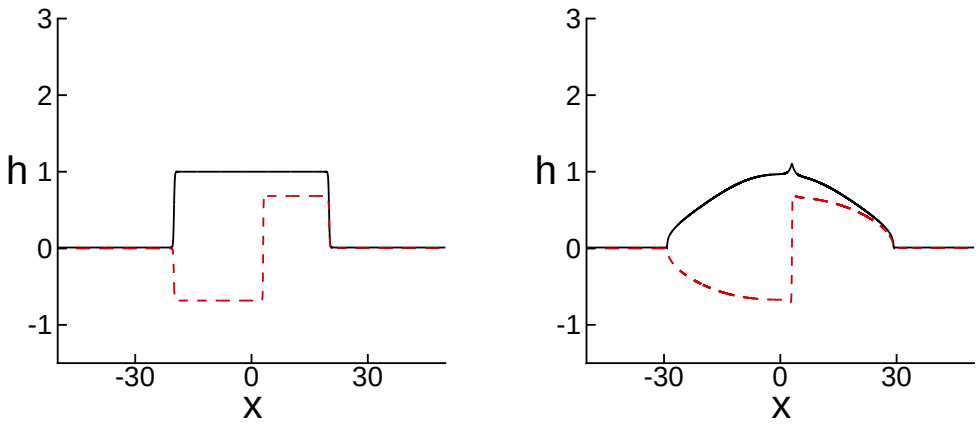

(a) $t = 0$ (b) $t = 20$

Figure 3.7 Stably spreading droplet with a defect at $x_0 = 3$: $\beta = 0.6$, $h_0 = 1$ and $\mathcal{N} = 10$, as in Figure 3.3. The solid (black) curves show the droplet profile h and the dashed (red) curves show the corresponding anchoring function $\Theta(x)m(h)$.

We have carried out other simulations with different parameter values and with different numbers of imposed defects. We have found that in all our simulations defects do not appear to alter the stability of the bulk droplet. Stability of an initially rectangular droplet containing one or more defects is still very well predicted by the linear analysis of the flat film of the same height. For a stable spreading droplet, a defect leads to a crest in the profile at large times, while for the unstable case, the defect gives rise to a pinned hump. Furthermore, in either case, defects do not

influence spreading versus nonspreading behavior. They have only a local effect; global effects, such as surface anchoring strength over the whole droplet, are more likely to affect the spreading behavior.

3.4 Influence of Prescribed Director Orientation at the Substrate

3.4.1 Uni-Directional Director Field

To analyze the influence of spatially-varying substrate anchoring $\phi(x, y)$ on droplet spreading, we firstly compare the governing equations for two different uni-directional substrate anchoring patterns. Assuming $\phi = 0$ and y-independent (the droplet spreads in the x direction and the director orientation at the substrate is parallel to the fluid flow), we have

$$h_t + \frac{5}{3}\,\partial_x \left[h^3 \left(h_{xxx} - h_x \right) + \mathcal{N} \left(m^2 - \frac{5}{2} h m m' \right) h_x \right] = 0. \tag{3.42}$$

If we assume $\phi = \pi/2$ and y-independent (the director orientation at the substrate is perpendicular to the fluid flow), the equation becomes

$$h_t + \frac{1}{3}\,\partial_x \left[h^3 \left(h_{xxx} - h_x \right) + \mathcal{N} \left(m^2 - \frac{5}{2} h m m' \right) h_x \right] = 0. \tag{3.43}$$

These two equations are identical once the time is rescaled by a constant. That is, the only influence of the substrate pattern is on the time scale. NLC flows faster if the substrate anchoring pattern is parallel to the flow direction, while it is slower otherwise.

3.4.2 Weak Surface Anchoring

To further identify the effect of the substrate anchoring pattern, $\phi(x, y)$, we assume that the surface anchoring is so weak that the director orientations are mainly determined by the boundary conditions at the substrate, $\theta = \pi/2$. We can then

set $\mathcal{N} = 0$ in our model. The resulting equation is

$$h_t + \nabla \cdot \left[h^3 \left\{ \left(I + \frac{2}{3} \begin{bmatrix} \cos 2\phi & \sin 2\phi \\ \sin 2\phi & -\cos 2\phi \end{bmatrix} \right) \cdot \nabla \right\} \left(\nabla^2 h - h \right) \right] = 0. \qquad (3.44)$$

As a first step in our investigations, we simulate a spreading droplet where the anchoring at the substrate appears as stripes. (As illustrated in Figure 3.8, $\phi = \pi/2$ for $x \in (4n-1, 4n+1)$, $n = 0, \pm 1$ and ± 2, and $\phi = 0$ otherwise.) Figure 3.8 shows the contact line evolution of such a droplet. The initial contact line position is a straight line, and the droplet spreads in the $+y$ direction. When the droplet spreads, the anchoring pattern at the substrate will influence the fluid motion. As we discussed previously, it moves faster when the fluid motion is in parallel with the anchoring pattern, and is slower when flow is perpendicular to anchoring. This is verified in Figure 3.8. The contact line moves faster at $x = 0, \pm 4$ and ± 8, where the director is aligned parallel to y. Furthermore, since the contact line moves with different speed at the substrate, it appears as sawtooth pattern in this example.

We now proceed to analyze the influence of different substrate anchoring patterns on spreading droplets. In particular, we investigate patterns that represent idealized defects. In Section 3.3.3, we have presented a simple model to consider the influence of defects at the free surface, in two space dimensions. We find that a defect does not alter the stability properties of the film. It only modifies locally the droplet profile, appearing as a crest at the free surface. Here we consider the influence of corresponding substrate anchoring patterns that may represent defects. There are four essential types of point defect [24], characterized by the winding number, m, of the accompanying director field. These four defects are $m = \pm 1$ and $m = \pm 1/2$, with anchoring patterns shown in Figure 3.9 (b) and in Figure 3.10 (a), (b) and (c).

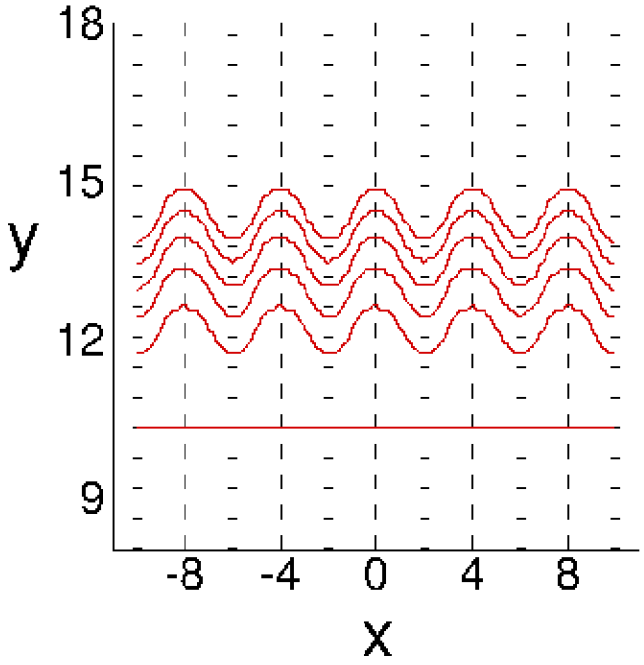

Figure 3.8 Contact line evolution of a spreading NLC front on the stripe-patterned substrate. The black dashed lines show the anchoring pattern at the substrate. The red curves show the contact line position at different times, with time interval $dt = 10$ between successive curves. The initial position of the contact line is shown as a red straight line at $y \approx 10$.

Figure 3.9 shows the evolution of a droplet on the simplest point defect, $m = 1$ radially symmetric defect. Due to the symmetry, the droplet spreads uniformly in the radial direction, and the contact line remains circular for all time.

Figure 3.10 shows the droplet evolutions for the three other different point defect patterns. Each point defect has its corresponding substrate anchoring pattern. Due to the nonuniformity of the pattern in the radial direction, the droplet spreads differently. In general, the spreading behaviors follow the substrate anchoring patterns.

3.5 Implications for the Experiment

The two trends observed by Poulard & Cazabat are that higher humidity correlates with droplet instability, as does larger droplet size. They also state (See Section IV.1

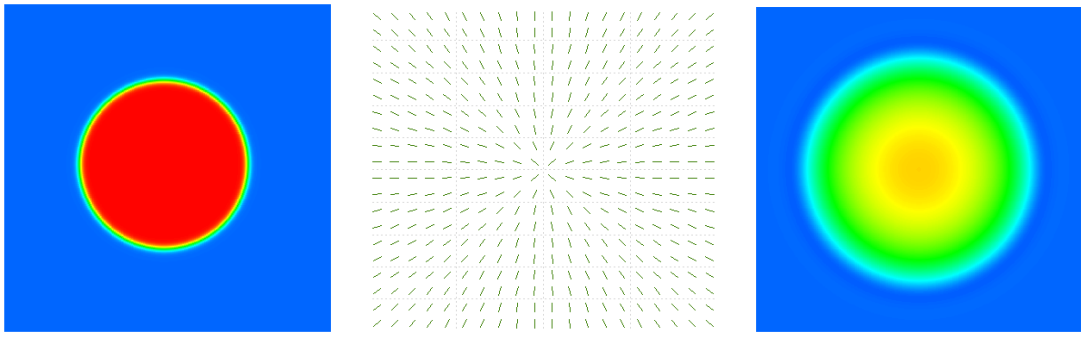

(a) ($t = 0$, contour) (b) $m = 1$ (anchoring) (c) $m = 1$ ($t = 10$, contour)

Figure 3.9 Spreading NLC droplet on radial substrate anchoring. The surface anchoring is assumed to be weak such that the flow can be described by Equation (3.44). The initial condition is shown in (a), with substrate anchoring pattern shown in (b) and the contour plot at $t = 10$ shown in (c).

in [54]) that at low RH, the drops do not spread macroscopically. These observations are only qualitative however, and likely the interplay between the individual effects of droplet size and humidity is complex. We note in addition that although humidity can affect surface tension (so that in principle the capillary number could change), we focus here on its effect on β and $\mathcal{N}$. We deal with each of these in turn.

If $\mathcal{N}$ is fixed then we hypothesize that β is a decreasing function of humidity: that is, larger values of β correspond to low humidity, and vice versa. This correlation would suggest that at low humidity anchoring is weaker (for a given droplet height h, the value of $m(h)$ decreases as β increases), and that effective anchoring strength increases with humidity. If this is so then our model supports this qualitative trend, since in general large values of β give rise numerically to stable drops, while small values of β (for droplet height h lying in the appropriate range) give rise to unstable drops. We note also that under this assumption our model leads to additional predictions, which would be interesting to test with future experiments: firstly, sufficiently large droplets (h_0 above the upper branch of the stability curve

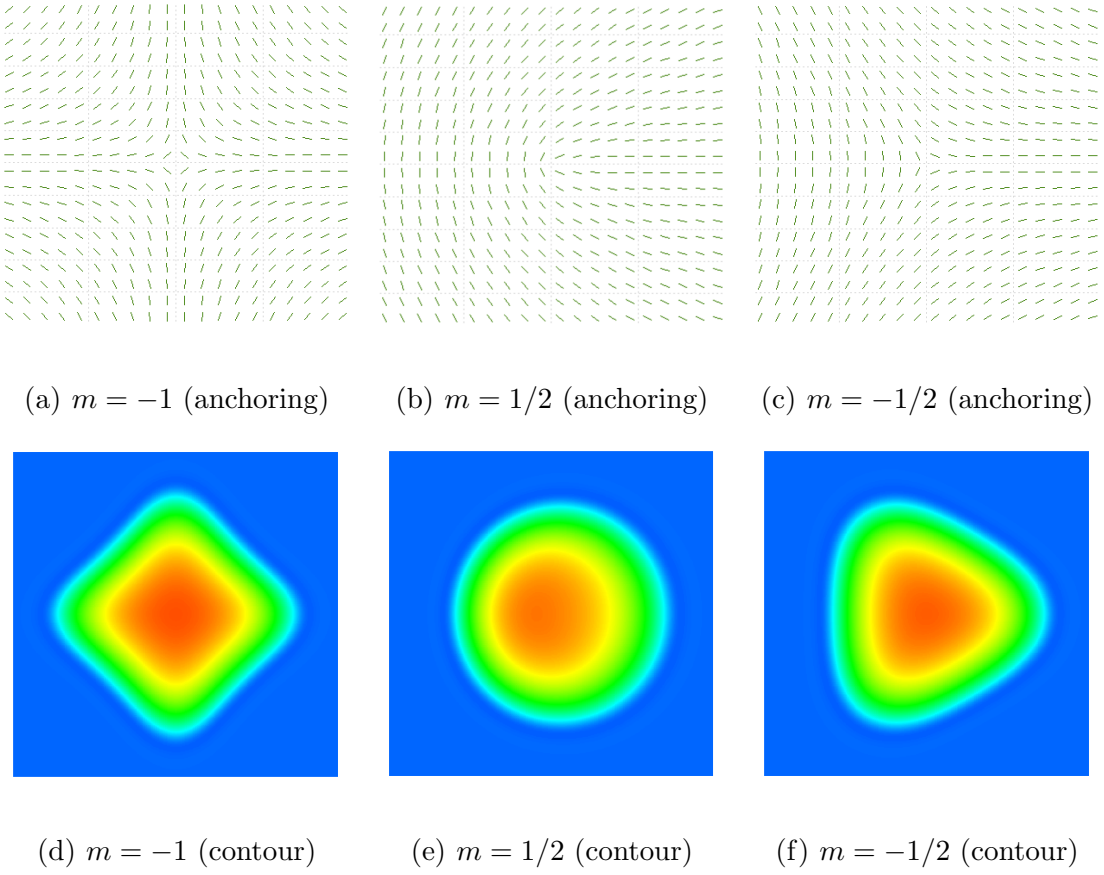

(a) $m = -1$ (anchoring) (b) $m = 1/2$ (anchoring) (c) $m = -1/2$ (anchoring)

(d) $m = -1$ (contour) (e) $m = 1/2$ (contour) (f) $m = -1/2$ (contour)

Figure 3.10 Spreading NLC droplets on different substrate anchoring patterns. The surface anchoring is assumed to be weak such that the flow can be described by Equation (3.44). Panels (a), (b) and (c) show the anchoring pattern at the substrate, while (d), (e) and (f) show the contour plot of film thickness at $t = 10$. The initial conditions are the same for all three simulations and are shown in Figure 3.9 (a).

in Figure 3.2) should again become stable; and secondly, at sufficiently low humidity (sufficiently large β) droplets of any size should be stable.

Suppose now that β is fixed, while $\mathcal{N}$ varies with humidity, via its dependence on Θ. Humidity is known to affect anchoring angles; the work [5] suggests that Θ, and hence $\mathcal{N}$, could be an increasing function of humidity. Looking at Equation (3.38), the general trend for increasing humidity is then correct, since the stability of a film goes from stable to unstable as $\mathcal{N}$ increases.

Temperature is also investigated experimentally. This quantity can, of course, influence many variables, but Poulard & Cazabat focus chiefly on its effect on the

elastic constant K, which decreases as temperature increases [2]. While the dependence on temperature is not precisely documented, the observed trend is that increasing temperature suppresses the instabilities. This general effect is captured by the model, since as K decreases, $\mathcal{N}$ decreases, and the stability of a film goes from unstable to stable. The data shown in Figure 4 of [22] show that the variation of K can be quite profound over only a few degrees Kelvin, so that the stability of a film can change appreciably as temperature is varied.

3.6 Conclusions

We have presented a new model for spreading of a thin film of nematic liquid crystal, in which the traditional anchoring boundary conditions on the director (either strong anchoring, or classical weak "Rapini-Papoular" anchoring [56], neither of which are suitable to describe a very thin spreading film) are replaced by a new condition, Equation (3.23). This new formulation preserves the property of strong anchoring when the film is thick, while allowing the director to relax to a state of uniform alignment when the film is very thin.

We have found two mechanisms leading to an unstable spreading droplet: the bending forces of the anchoring angle, θ, between the free surface and at the solid substrate leads to free surface instability, while the anchoring conditions, ϕ, at the solid substrate may guide a droplet to spread accordingly.

For the two-dimensional surface instability, simple linear stability analysis for a flat film appears to serve as a very good indicator of the behavior of more complicated spreading drops, even providing reasonable estimates of the wavelength of droplet instabilities well into the nonlinear regime. The basic mechanism driving the instability is the mismatch in anchoring angles at the rigid substrate and the

[2] Of course, quantities such as viscosity can also change dramatically with temperature; but with the Bond and capillary numbers fixed, viscosity does not enter the remaining parameters. The viscosity would, however, affect the wavenumber of any observed instability, but this effect is not studied.

drop's free surface. This mismatch means that the director has to bend across the film, and for sufficiently thin films, this requires a large energy penalty, which is destabilizing.

For three-dimensional spreading drops, we find that the speed of spreading changes dramatically at different substrate anchoring patterns. A drop spreads faster when the anchoring at the substrate is in parallel with its flow, while spreading is slower when flow is perpendicular to the substrate anchoring. For a substrate with nonuniform anchoring conditions, the contact line behaves nonuniformly, in the manner expected with the prescribed anchoring patterns.

We also examined the influence of defects on a spreading droplet. Our simple 2D model and simulations suggest that defects will not alter the stability character of the film. At the free surface, the influence of a defect is only local, including a crest. On the other hand, our 3D model, which allows us to investigate anchoring patterns at the substrate that may correspond to a defect, indicates that the contact line of a spreading droplet can behave quite differently as the substrate anchoring is varied. However, as discussed in Section 3.3.3, the size of a defect core is typically much smaller compared to a droplet. The influence of a defect with its corresponding patterns still requires further studies.

In addition, all the three-dimensional simulations we have shown were done for the case $\mathcal{N} = 0$, without including the free surface anchoring (thus, the elastic bending of the NLC across the layer is negligible). To study fully a NLC drop, it is necessary to consider the case where elasticity and "defects" acting simultaneously. This will be done in the near future.

CHAPTER 4

CONCLUDING REMARKS AND FUTURE WORK

In this Dissertation, we have studied the instabilities of Newtonian films flowing down an inverted inclined plane within a framework using the long wave (lubrication) approximation. Both completely wetting and partially wetting fluids are considered. We have found that, a contact line, modeled by the commonly used precursor film model, leads to free surface instabilities without any natural or imposed perturbation. Complex behavior, due to the coupling of the surface instabilities and the well-known transverse (fingering) instabilities, was uncovered with different families of waves evolving in the configurations characterized by different values of the governing parameter D, measuring the strength of the destabilizing component of gravity. The observed instabilities are categorized into three types and are further examined using linear stability analysis together with the absolute and convective instability analysis of a flat film. We find excellent agreement.

We have also studied the flow of a nematic liquid crystal. A mathematical model for the evolution of the surface flow of a nematic liquid crystal is derived based on the long wave approximation. The present model shows satisfactory behavior in the vicinity of the contact line. Instabilities are also studied. It is found that the mismatch of the anchoring angle, θ, at the free surface and at the substrate leads to free surface instabilities, while the anchoring condition at the solid substrate, ϕ, affects the speed of spreading.

The results and approaches presented here could serve as a basis for significant further research. As we pointed out in Section 2.4, breakup of a film plays an important role for partially wetting fluids. But we so far only considered the LSA based analysis without investigating when and how the film breaks up. Specifically,

in Figure 2.28 we have shown the stability of a film of partially wetting fluids flowing down an inclined plane under the influence of a front. There should be another curve in this figure to indicate whether or not the film will experience breakup. In addition, we have observed rich dynamics as the inclination angle α approaches 180°. How are the instability mechanisms that we have studied for completely wetting fluids modified in the case of partially wetting fluids requires further investigation.

In the direction of NLC flow, the surface anchoring energy that we used is based on the regularizing hypothesis that an NLC film approaches the isotropic state as the film height goes to zero. More experimental support as well as theoretical justification regarding the form of the surface anchoring energy are definitely needed. Besides, one should also note that the Leslie-Ericksen equations in the presented format, Equations (3.1)-(3.3), do not support mathematically a defect. Indeed, discontinuities of the director field in the vicinity of a defect break down the continuum assumption. Our approach, in this Dissertation, is to model the influence of a defect in two ways. One is to consider the influence of rapid variation of the director field across a defect. We derive a smoothed model in which the director field varies continuously, but abruptly, in the region of the supposed defect. The other approach is to consider the influence of substrate anchoring patterns surrounding a defect. Although we have found expected behavior of NLC flow under these two approaches, a rigorous theoretical justification is needed.

Further experimental verification of all studied instabilities is also needed. In spring 2011, undergraduate students at NJIT studied the NLC fluids flow down an inclined plane. They performed experiments and simulations and had found interesting results [48]. Particularly, in simulations they observed the contact line induced waves similar to what we have found in the Newtonian fluids under destabilizing forces (for example, Figure 2.5). This finding is not surprising as the films of NLC flow experience destabilizing force from the anchoring, and so the contact

line might have a chance to influence the films behind it. We believe that the new mechanism of contact line instabilities found in our work can be applied to other scenarios as well, such as under destabilizing electric fields or on a heated plate.

Finally, regarding numerical simulations, all the results we have shown are based on a method developed in Cartesian geometry. While most of the problems can be solved in such a geometry, there are some cases where the usage of polar coordinate is more appropriate. For example, one of the techniques in coating is to place a blob of liquids in the center of a spinning flat plate such that the blob will spreads outward and leave a coating that is uniform in thickness, so-called spin coating [62]. Obviously, polar coordinates are the most natural choice for such a geometry. It would be of interested to extend the ADI type of simulations that we implemented in the Cartesian case to polar geometry.

APPENDIX A

EVOLUTION OF SMALL PERTURBATIONS

Equation (2.4) is a strongly nonlinear PDE and, to our knowledge, has no analytical solutions. In this appendix, we present two analytical approaches which consider evolution of small perturbations from a base state within linear approximation. While these results are useful for the purpose of verifying numerical results, they also provide a very useful insight into formation and evolution of various instabilities discussed in this work.

A.1 Traveling Wave Solution

Setting $s = x - Ut$ in Equation (2.4), a traveling wave $H(s) = h(x,t)$ must satisfy

$$-UH + [H^3(H''' - DH' + 1)] = c. \tag{A.1}$$

Imposing the conditions $H \to 1$ as $s \to -\infty$, and $H \to b$ as $s \to \infty$, we find $U = 1+b+b^2$, $c = -b-b^2$ [8, 70]. The traveling wave speed, U, is useful for verifying whether or not the numerical result is indeed a traveling wave.

Figure A.1 shows a typical profile of the traveling wave solution for $D = -1$. A capillary ridge forms behind the fluid front, similarly as for the flow down a vertical or inclined ($D > 0$) substrate. We also find that there exists a long oscillatory region behind the capillary ridge. To analyze this 'tail', we expand Equation (A.1) around the base state, $H \equiv 1$, and consider the evolution of a small perturbation of the form $exp(qs)$, where $q = q_r + iq_i$. We find

$$-8q_r^3 + 2Dq_r + 2 - b - b^2 = 0, \tag{A.2}$$

$$q_i^2 + D = 3q_r^2. \tag{A.3}$$

Table A.1 shows the only positive root for q_r, for a set of D's. The positivity of this root signifies that the amplitude of the tail decays exponentially in the $-x$ direction, as also suggested by the insets of Figure A.1. Furthermore, as shown in Table A.1, q_r decreases for more negative D's, meaning that the tail is longer for these D's. This table also shows the imaginary part of q; we see an increase of its magnitude as D becomes more negative, suggesting shorter and shorter wavelengths in the tail. Tail behavior is very useful for computational reasons. For example,

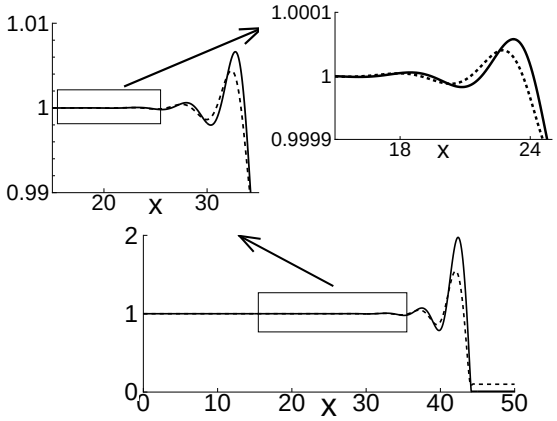

Figure A.1 Traveling wave solution of $D = -1$ case at three different scales with precursor thickness $b = 0.01$ (solid) and $b = 0.1$ (dashed). Note that the precursor thickness only changes amplitude of the traveling wave profile but not the wavelength. The arrows point to the zoomed-in regions.

to solve Equation (A.1) by a shooting method, one can evaluate suitable shooting parameters through Equations (A.2,A.3).

Figure A.1 also shows the effect of precursor thickness on traveling wave solution. It is found that while the precursor thickness changes the height of the capillary ridge, it has almost no effect on the wavelength of the tail.

A.2 Linear Stability Analysis

Another approach to analyze the stability of a flat film, is classical linear stability analysis. Assume $h = 1 + \xi$ where $\xi \ll 1$. Equation (2.4) can be simplified to the

Table A.1 Properties of the Damped Oscillatory Region Behind the Capillary Ridge

D	q_r	q_i
0	0.63	1.09
-1.0	0.50	1.32
-2.0	0.38	1.56
-3.0	0.30	1.81

leading order as

$$\xi_t + \xi_{xxxx} - D\xi_{xx} + 3\xi_x = 0. \tag{A.4}$$

By putting $\xi \sim \exp i(kx - \omega t)$, where $\omega = \omega_r + i\omega_i$, we obtain the dispersion relation

$$-i(\omega_r + i\omega_i) + k^4 + Dk^2 + 3ik = 0, \tag{A.5}$$

hence

$$\omega_r = 3k, \quad \omega_i = -(k^4 + Dk^2) = -(k^2 + D/2)^2 + D^2/4. \tag{A.6}$$

As a result, for non-negative D's, a flat film is stable under small perturbations. For negative D's, it is unstable for the perturbations characterized by sufficiently large wavelengths. The critical wave number $k_c = \sqrt{-D}$, and the perturbation with wave number $k_m = \sqrt{-D/2}$ has the largest growth rate. Besides, the speed of a linear wave is 3, and it is significantly larger than the traveling wave speed, U. As discussed in the main body of the text, this speed is very important to identify the waves induced by natural noise.

In addition, one should note that the maximum growth rate increases as inclination angle α goes from $\pi/2$ to π. Particularly, in the limiting case $\alpha \to \pi$ (hanging film), the growth rate is exactly the same as for thin film Rayleigh-Taylor

instability (e.g., [9]). Note that the scaling used in present work is not appropriate for $\alpha \to \pi$; to establish the result for this case, one should consider a different scaling, or the dimensional formulation of the problem.

A.3 Absolute and Convective Instability Analysis

For an unstable film, $D < 0$, we can perform the absolute and convective instability analysis by carrying out a change of variables

$$\eta = \sqrt{-D}\,(x - 3\,t)\,, \quad \tau = (-D)^2\,t$$

in Equation (A.4). Then we have

$$\xi_\tau + \xi_{\eta\eta\eta\eta} + \xi_{\eta\eta} = 0.$$

The front velocities (velocity of the boundary of local disturbance) are known as ± 1.62 [15]. Therefore, the front velocities of completely wetting films, Equation (A.4), are

$$\left(\frac{x}{t}\right)_{\pm} = 3 \pm 1.62\,(-D)^{3/2}. \tag{A.7}$$

APPENDIX B

NUMERICAL METHODS FOR THIN FILM EQUATION

In this appendix, we present a numerical method to solve Equation (2.3). We use finite difference method to discretize spatial variables and integrate in time implicitly. Such a procedure leads to a nonlinear system that needs to be solved in each time step. We use the Newton's method to solve such a system for two dimensional problems and use the approximate-Newton approach to solve three dimensional problems.

B.1 Solving Nonlinear Time Dependent PDE

In general, time dependent PDE can be expressed as $h_t + f(h) = 0$, where $h = h(\boldsymbol{x}, t)$ is the unknown function with time variable t, spatial variables $\boldsymbol{x}$, and f is a nonlinear discretization operator for spatial variables. From time $t^n = n\Delta t$ to t^{n+1}, where Δt is the time step, the PDE can be integrated numerically by the so-called θ method leading to a nonlinear system:

$$h^{n+1} + (1-\theta)\Delta t f^{n+1} = h^n - \theta \Delta t f^n, \tag{B.1}$$

where $f^n = f(h^n)$ and $h^n = h(\boldsymbol{x}, t^n)$. This method is known to be first order for $\theta \neq 1/2$ and is second order for $\theta = 1/2$. In this Dissertation, we use $\theta = 1/2$ for numerical simulations.

To solve the nonlinear system (B.1), we apply the Newton's method. Firstly, we linearize h^{n+1} about a guess for the solution by assuming $h^{n+1} = h^* + c$, where h^* is a guess and c is the correction. Then we express the nonlinear part using Taylor's expansion

$$f^{n+1} = f(h^* + c) \approx f(h^*) + J_f(h^*) \cdot c = f^* + J_f^* \cdot c,$$

where J_f is the Jacobian matrix for function f and $J_f^* = J_f(h^*)$. After substituting the above quantities into Equation (B.1), we obtain a linear system for the correction term, c:

$$\left(I + (1-\theta)\Delta t J_f^*\right) c = -h^* - (1-\theta)\Delta t f^* + h^n - \theta \Delta t f^n, \tag{B.2}$$

where I is the identity matrix that has the same size as the Jacobian matrix, J_f^*. The solution at $t = t^{n+1}$ is obtained by correcting the guess iteratively until the process converges, i.e., the new correction is small enough.

B.2 Spatial Discretization for Thin Film Equation

We discretize the spatial derivatives of thin film equation through finite difference method. The grid points in the computational domain, $[0, L] \times [0, M]$, is defined as

$$x_i = \left(i - \frac{1}{2}\right)\Delta x, \quad i = 1, \cdots, n_x, \quad y_j = \left(j - \frac{1}{2}\right)\Delta y, \quad j = 1, \cdots, n_y, \tag{B.3}$$

where $\Delta x = L/n_x$, $\Delta y = M/n_y$ are the step size in the x, y domain; n_x, n_y are number of grid points in the x, y domain, respectively.

The scheme presented here is 2nd order central difference scheme. In the following, the subscripts, i, j, denote that the value been taken at (x_i, y_j). The notation $h_{i+1/2,j}$ denotes an average at the point $(x_{i+1/2}, y_j)$ as

$$h_{i+1/2,j} = \frac{h_{i+1,j} + h_{i,j}}{2}.$$

Also we use the standard difference notation as

$$\begin{aligned}
\delta_x h_{i+1/2,j} &= h_{i+1,j} - h_{i,j}, \\
\delta_y h_{i,j+1/2} &= h_{i,j+1} - h_{i,j}, \\
\delta_x^3 h_{i+1/2,j} &= h_{i+2,j} - 3h_{i+1,j} + 3h_{i,j} - h_{i-1,j}, \\
\delta_y^3 h_{i,j+1/2} &= h_{i,j+2} - 3h_{i,j+1} + 3h_{i,j} - h_{i,j-1}, \\
\delta_x \delta_y^2 h_{i+1/2,j} &= h_{i+1,j+1} - 2h_{i+1,j} + h_{i+1,j-1} - h_{i,j+1} + 2h_{i,j} - h_{i,j-1}, \\
\delta_y \delta_x^2 h_{i,j+1/2} &= h_{i+1,j+1} - 2h_{i,j+1} + h_{i-1,j+1} - h_{i+1,j} + 2h_{i,j} - h_{i-1,j}.
\end{aligned}$$

The discretization of each term involving spatial derivatives is as follows: The surface tension term

$$\begin{aligned}
&\nabla \cdot [h^3 \nabla \nabla^2 h]_{i,j} = \\
&\left(h^3_{i+1/2,j} \delta_x^3 h_{i+1/2,j} - h^3_{i-1/2,j} \delta_x^3 h_{i-1/2,j} \right) / \Delta x^4 \\
&+ \left(h^3_{i+1/2,j} \delta_x \delta_y^2 h_{i+1/2,j} - h^3_{i-1/2,j} \delta_x \delta_y^2 h_{i-1/2,j} \right) / \Delta x^2 \Delta y^2 \\
&+ \left(h^3_{i,j+1/2} \delta_y \delta_x^2 h_{i,j+1/2} - h^3_{i,j-1/2} \delta_y \delta_x^2 h_{i,j-1/2} \right) / \Delta x^2 \Delta y^2 \\
&+ \left(h^3_{i,j+1/2} \delta_y^3 h_{i,j+1/2} - h^3_{i,j-1/2} \delta_y^3 h_{i,j-1/2} \right) / \Delta y^4.
\end{aligned}$$

The normal gravity term

$$\begin{aligned}
&\nabla \cdot [h^3 \nabla h]_{i,j} = \\
&\left(h^3_{i+1/2,j} \delta_x h_{i+1/2,j} - h^3_{i-1/2,j} \delta_x h_{i-1/2,j} \right) / \Delta x^2 \\
&+ \left(h^3_{i,j+1/2} (h_{i,j+1} - h_{i,j}) - h^3_{i,j-1/2} (h_{i,j} - h_{i,j-1}) \right) / \Delta y^2.
\end{aligned}$$

The tangential gravity term

$$\frac{\partial}{\partial x} \left(h^3 \right)_{i,j} = \left(h^3_{i+1/2,j} - h^3_{i-1/2,j} \right) / \Delta x.$$

B.3 Fully Implicit Algorithm

Applying algorithm Equation (B.2) to 3D thin film equation, we have [26]

$$\left(I + (1-\theta)\Delta t(J^*_{fx} + J^*_{fy} + J^*_{fm})\right) \cdot c = -h^* - (1-\theta)\Delta t f^* + h^n - \theta \Delta t f^n,$$

where J_{fx}, J_{fy} and J_{fm} are the Jacobian matrices for x, y and mixed derivative terms of function f, respectively. Equation (B.4) is a non-symmetric sparse linear system that has $n_x n_y$ unknowns. For large n_x and n_y, as it is the case for the problems discussed in the present work, solving such a system carries a significant computational cost. In general, the operation count is proportional to $O(n_x^3 n_y^3)$ or $O(n_x^2 n_y^2)$, depending on the matrix solver.

B.4 Alternating Direction Implicit (ADI) Method

To decrease the computational cost, Witelski and Bowen suggested to use the approximate-Newton approach [71]. The idea is to replace the Jacobian matrix by an approximated one

$$\left[I + (1-\theta)\Delta t \left(J^*_{fx} + J^*_{fy} + J^*_{fm}\right)\right] \sim \left[I + (1-\theta)\Delta t J^*_{fy}\right] \left[I + (1-\theta)\Delta t J^*_{fx}\right].$$

Therefore we get a new system of equations

$$\left[I + (1-\theta)\Delta t J^*_{fy}\right] \left[I + (1-\theta)\Delta t J^*_{fx}\right] \cdot c = R, \tag{B.4}$$

where $R = -h^* - (1-\theta)\Delta t f^* + h^n - \theta \Delta t f^n$ is the right hand side of Equation (B.4). One should note that as long as c decreases after each iteration and approaches 0 in some norm, we have $R = 0$, leading to Equation (B.1). That is, such an approach does not affect the stability and accuracy of the original space-time discretization.

Under the same spirit of ADI method, equation (B.4) can be easily split into two steps:

$$\begin{aligned} \left(I + (1-\theta)\Delta t J^*_{fx}\right) \cdot w &= R, \\ \left(I + (1-\theta)\Delta t J^*_{fy}\right) \cdot c &= w. \end{aligned} \tag{B.5}$$

The main advantage of such splitting is that the operations in the x and y directions are decoupled and therefore the computational cost reduced significantly. Specifically for our discretization, the Jacobian matrices in the x and y direction are penta-diagonal matrices, leading to system that can be solved in $O(n_x)$ and $O(n_y)$ arithmetic, and the overall computational cost for solving Equation (B.5) is proportional to $O(n_x n_y)$.

The approach presented here deals with a matrix that is an approximation to the original Jacobian one. Therefore we should not expect the convergent rate of the ADI method to be quadratic. However, since the approximation error is proportional to $O(\Delta t)$, for small enough time step, we expect the rate of convergence to be close to quadratic; see [71] for further discussion of this issue. Furthermore, the ratio in the operation count between fully implicit discretization and the ADI method is $O(n_x n_y)$. That is, even if we need to decrease the time step or increase the number of iterations to achieve convergence, the ADI method is still more efficient as long as the additional effort is of $o(n_x n_y)$. In our experience, under the same conditions, ADI method is significantly more efficient compared to fully implicit discretization.

BIBLIOGRAPHY

[1] D. J. Acheson. *Elementary Fluid Dynamics*. Clarendon, Oxford, 1990.

[2] S. V. Alekseenko, D. M. Markovich, and S. I. Shtork. Wave flow of rivulets on the outer surface of an inclined cylinder. *Phys. Fluids*, 8:3288, 1996.

[3] S. V. Alekseenko, V. E. Nakoryakov, and B. G. Pokusaev. Wave formation on a vertical falling liquid films. *AIChE J.*, 31:1446, 1985.

[4] S. V. Alekseenko, V. E. Nakoryakov, and B. G. Pokusaev. *Wave Flow of Liquid Films*. Begell House, New York, 1994.

[5] J. Bechhoefer, B. Jerme, and P. Pieranski. Systematic studies of the anchoring transition in nematic liquid crystals. *Phys. Rev. A*, 41:3187, 1990.

[6] M. Ben Amar and L. J. Cummings. Fingering instabilities in driven thin nematic films. *Phys. Fluids*, 13:1160, 2001.

[7] E. S. Benilov. On the stability of shallow rivulets. *J. Fluid Mech.*, 636:455, 2009.

[8] A. L. Bertozzi and M. P. Brenner. Linear stability and transient growth in driven contact lines. *Phys. Fluids*, 9:530, 1997.

[9] J. M. Burgess, A. Juel, W. D. McCormick, J. B. Swift, and H. L. Swinney. Suppression of dripping from a ceiling. *Phys. Rev. Lett.*, 86:1203, 2001.

[10] D. W. Calton, K. Seunarine, G. Bodammer, and I Underwood. Liquid crystal flow control using microfabrication techniques. *IEE Proc. Optoelectron.*, 147:163, 2000.

[11] J. Q Carou, B. R. Duffy, N. J. Mottram, and S. K. Wilson. Shear-driven and pressure-driven flow of a nematic liquid crystal in a slowly varying channel. *Phys. Fluids*, 18:027105, 2006.

[12] A. M. Cazabat, F. Heslot, S. M. Troian, and P. Carles. Fingering instability of thin spreading films driven by temperature gradients. *Natural (London)*, 346:824, 1990.

[13] S. Chandrasekhar. *Liquid Crystals*. Cambridge University Press, New York, 2nd edition, 1993.

[14] H. C. Chang. Wave evolution on a falling film. *Annu. Rev. Fluid Mech.*, 26:103, 1994.

[15] H. C. Chang and E. A. Demekhin. Stability of a solitary pulse against wave packet disturbances in an active medium. *Phys. Rev. Lett.*, 75:1747, 1995.

[16] H. C. Chang and E. A. Demekhin. *Complex Wave Dynamics on Thin Films*. Elsevier, New York, 2002.

[17] H. C. Chang, E. A. Demekhin, and D. I. Kopelevich. Nonlinear evolution of waves on a vertically falling film. *J. Fluid Mech.*, 250:433, 1993.

[18] H. C. Chang, E. A. Demekhin, and S. S. Saprikin. Noise-driven wave transitions on a vertically falling film. *J. Fluid Mech.*, 462:255, 2002.

[19] R. V. Craster and O. K. Matar. Dynamics and stability of thin liquid films. *Rev. Mod. Phys.*, 81:1131, 2009.

[20] L. J. Cummings. Evolution of a thin film of nematic liquid crystal with anisotropic surface energy. *Eur. J. Appl. Math.*, 15:651, 2004.

[21] L. J. Cummings, T.-S. Lin, and L. Kondic. Modeling and simulations of the spreading and destabilization of nematic droplets. *Phys. Fluids*, 23:043102, 2011.

[22] S. DasGupta and S. Kumar Roy. Splay and bend elastic constants and rotational viscosity coefficient in a mixture of 4-4-n-pentyl-cyanobiphenyl and 4-4-n-decyl-cyanobiphenyl. *Phys. Lett. A*, 306:235, 2003.

[23] J. R. de Bruyn. Growth of fingers at a driven three phase contact line. *Phys. Rev. A*, 46:4500, 1992.

[24] P. G. De Gennes and J. Prost. *The Physics of Liquid Crystals*. Oxford University Press, New York, 1995.

[25] J. Diez and L. Kondic. Contact line instabilities of thin liquid films. *Phys. Rev. Lett.*, 86:632, 2001.

[26] J. Diez and L. Kondic. Computing three-dimensional thin film flows including contact lines. *J. Comput. Phys.*, 183:274, 2002.

[27] J. Diez and L. Kondic. On the breakup of fluid films of finite and infinite extent. *Phys. Fluids*, 19:072107, 2007.

[28] B. R. Duffy and S. K. Wilson. A rivulet of perfectly wetting fluid with temperature-dependent viscosity draining down a uniformly heated or cooled slowly varying substrate. *Phys. Fluids*, 15:3236, 2003.

[29] D. V. Effenterre, M. P. Valignat, and D. Roux. Coupling between the nematic / isotropic transition and a thickness transition : A theoretical approach. *Europhys. Lett.*, 62:526, 2003.

[30] A. S. Fokas and D. T. Papageorgiou. Absolute and convective instability for evolution PDEs on the half-line. *Stud. Appl. Math.*, 114:95, 2005.

[31] R. Goodwin and G. M. Homsy. Viscous flow down a slope in the vicinity of a contact line. *Phys. Fluids A*, 3:515, 1991.

[32] P. Huerre and P. A. Monkewitz. Local and global instabilities in spatially developing flows. *Annu. Rev. Fluid Mech.*, 22:473, 1990.

[33] H. E. Huppert. Flow and instability of a viscous current down a slope. *Nature*, 300:427, 1982.

[34] A. Indeikina, I. Veretennikov, and H. C. Chang. Drop fall-off from pendent rivulets. *J. Fluid Mech.*, 338:173, 1997.

[35] P. L. Kapitsa and S. P. Kapitsa. Wave flow of thin fluid layers of liquid. *Zh. Eksp. Teor. Fiz.*, 19:105, 1949.

[36] S. F. Kistler and L. E. Scriven. The teapot effect: sheet-forming flows with deflection. *J. Fluid Mech.*, 263:19, 1994.

[37] L. Kondic. Instabilities in gravity driven flow of thin fluid films. *SIAM Rev.*, 45:95, 2003.

[38] L. Kondic and J. Diez. Contact line instabilities of thin film flows: constant flux configuration. *Phys. Fluids*, 22:052105, 2001.

[39] F. M. Leslie. Theory of flow phenomena in liquid crystals. *Adv. Liq. Cryst.*, 4:1, 1979.

[40] T.-S. Lin and L. Kondic. Thin films flowing down inverted substrates: Two dimensional flow. *Phys. Fluids*, 22:052105, 2010.

[41] T.-S. Lin, L. Kondic, and L. J. Cummings. Defect modeling in spreading nematic droplets. *Phys. Rev. E*, 85:012702, 2012.

[42] T.-S. Lin, L. Kondic, and A. Filippov. Thin films flowing down inverted substrates : Three-dimensional flow. *Phys. Fluids*, 24:022105, 2012.

[43] J. Liu and J. P. Gollub. Onset of spatially chaotic waves on flowing films. *Phys. Rev. Lett.*, 70:2289, 1993.

[44] J. Liu and J. P. Gollub. Solitary wave dynamics of film flows. *Phys. Fluids*, 6:1702, 1994.

[45] J. Liu, J. D. Paul, and J. P. Gollub. Measurement of the primary instabilities of film flows. *J. Fluid Mech.*, 250:69, 1993.

[46] A Mavromoustaki, O. K. Matar, and R. V. Craster. Shock-wave solutions in two-layer channel flow. I. One-dimensional flows. *Phys. Fluids*, 22:112102, 2010.

[47] R. B. Meyer. Point disclinations at a Nematic-lsotropic Liquid Interface. *Mol. Cryst. Liq. Cryst.*, 16:355, 1972.

[48] S. Naughton, N. Patel, and I. Seric. Advisors: L. Kondic, L. J. Cummings and T.-S. Lin. Instabilities of spreading liquid crystal films. *submitted to SIURO*.

[49] T. Nosoko and A. Miyara. The evolution and subsequent dynamics of waves on a vertically falling liquid film. *Phys. Fluids*, 116:1118, 2004.

[50] A. Oron, S. H. Davis, and S. G. Bankoff. Long-scale evolution of thin liquid films. *Rev. Mod. Phys.*, 69:931, 1997.

[51] A. Oron and P. Rosenau. Formation of patterns induced by thermocapillarity and gravity. *J. Phys. (France)*, 2:131, 1992.

[52] P. Palffy-Muhoray. The diverse world of liquid crystals. *Phys. Today*, 60:54, 2007.

[53] T. Podgorski, J.-M. Flesselles, and L. Limat. Corners, Cusps, and Pearls in Running Drops. *Phys. Rev. Lett.*, 87:1, 2001.

[54] C. Poulard and A. M. Cazabat. Spontaneous spreading of nematic liquid crystals. *Langmuir*, 21:6270, 2005.

[55] W. G. Pritchard. Instabilities and chaotic behavior in a free surface flow. *J. Fluid Mech.*, 165:1, 1986.

[56] A. Rapini and M. Papoular. Distorsion d'une lamelle nematique sous champ magnetique, conditions d'ancrage aux parois. *J. Phys. (Paris), Colloq.*, 30:54, 1969.

[57] P. Rosenau, A. Oron, and J. M. Hyman. Bounded and unbounded patterns of the Benney equation. *Phys. Fluids A*, 4:1102, 1992.

[58] K. J. Ruschak. Coating flow. *Annu. Rev. Fluid Mech.*, 17:65, 1999.

[59] S. Saprykin, E. A. Demekhin, and S. Kalliadasis. Two-dimensional wave dynamics in thin films. I. Stationary solitary pulses. *Phys. Fluids*, 17:117105, 2005.

[60] N. Scholpohl and T. J. Sluckin. Defect core structure in nematic liquid crystals. *Phys. Rev. Lett.*, 59:2582, 1987.

[61] L. W. Schwartz. Viscous flows down an inclined plane: Instability and finger formation. *Phys. Fluids A*, 1:443, 1989.

[62] L. W. Schwartz and R. V. Roy. Theoretical and numerical results for spin coating of viscous liquids. *Phys. Fluids*, 16:569, 2004.

[63] T. M. Segin, B. S. Tilley, and L. Kondic. On undercompressive shocks and flooding in countercurrent two-layer flows. *J. Fluid Mech.*, 532:217, 2005.

[64] V. Shikin and E. Lebedeva. Anti-gravitational instability of the neutral Helium film. *J. Low Temp. Phys.*, 119:469, 2000.

[65] N. Silvi and E. B. Dussan V. On the rewetting of an inclined solid surface by a liquid. *Phys. Fluids*, 28:5, 1985.

[66] H. A. Stone, A. D. Stroock, and A. Ajdari. Engineering flows in small devices. *Annu. Rev. Fluid Mech.*, 36:381, 2004.

[67] J. S. Sullivan, S. K. Wilson, and B. R. Duffy. A thin rivulet of perfectly wetting fluid subject to a longitudinal surface shear stress. *Q. J. Mech. Appl. Math.*, 61:25, 2008.

[68] A. J. Tanasijczuk, C. A. Perazzo, and J. Gratton. Navier Stokes solutions for steady parallel-sided pendent rivulets. *Eur. J. Mech. B/Fluids*, 29:465, 2010.

[69] Y. Y. Trifonov and O. Y. Tsvelodub. Nonlinear waves on the surface of a falling liquid film. Part 1. Waves of the first family and their stability. *J. Fluid Mech.*, 229:531, 1991.

[70] S. M. Troian, E. Herbolzheimer, S. A. Safran, and J. F. Joanny. Fingering instabilities of driven spreading films. *Europhys. Lett.*, 10:25, 1989.

[71] T. P. Witelski and M. Bowen. ADI schemes for higher-order nonlinear diffusion equations. *Appl. Numer. Math.*, 45:331, 2003.